



ICT-777137

5G-RANGE

5G-RANGE: Remote Area Access Network for the 5th Generation

Research and Innovation Action
H2020-EUB-2017 – EU-BRAZIL Joint Call

Deliverable 3.2 Physical layer of the 5G-RANGE – Part II

Due date of deliverable: 31st January 2019
Actual submission date: 20th February 2019

Start date of project: 1 November 2017
Lead contractor for this deliverable: TUD
Version 1 date: 20st February 2019
Confidentiality status: Public

Duration: 30 months

Abstract

D3.2 is a technical report describing channel coding, waveforms, corresponding inner transceiver designs and MIMO schemes for the 5G-RANGE PHY. 5G-ACRA, 5G-FlexNOW, 5G-IR2A and 5G-MIMORA are the corresponding building blocks, which are specified as part of this deliverable.

Target audience:

The primary target audience for this document is the radio access network research and development community, particularly those with an interest in mobile communication physical and MAC layers. This material can be fully understood by readers with a background in mobile wireless cellular systems, especially those familiar with 3GPP standards for 4G and 5G.

Disclaimer

This document contains material, which is the copyright of certain 5G-RANGE consortium parties and may not be reproduced or copied without permission. All 5G-RANGE consortium parties have agreed to the full publication of this document. The commercial use of any information contained in this document may require a license from the proprietor of that information.

Neither the 5G-RANGE consortium as a whole, nor a certain party of the 5G-RANGE consortium warrant that the information contained in this document is capable of use, or that use of the information is free from risk and accept no liability for loss or damage suffered by any person using this information.

This document does not represent the opinion of the European Community, and the European Community is not responsible for any use that might be made of its content.

Impressum

Full project title:	5G-RANGE: Remote Area Access Network for the 5th Generation
Document title:	D3.2 Physical layer of the 5G-RANGE – Part II
Editor:	Peter Neuhaus (TUD)
Work Package No. and Title:	WP3, Physical layer of the 5G-RANGE
Work Package leaders:	Peter Neuhaus, TUD (EU), Luciano Mendes, Inatel (BR)
Project Co-ordinators:	Marcelo Bagnulo, UC3M (EU), Priscila Solis, UnB (BR)
Technical Managers:	Yaning Zou, TUD (EU), Luciano Mendes, Inatel (BR)

This project is co-funded by the European Union through the ICT programme under H2020.

Copyright notice

© 2019 Participants in project 5G-RANGE

Executive Summary

This deliverable provides the specification of the 5G-RANGE PHY. All components are tailored to the requirements from D2.1 [1] and chosen based on performance evaluations on the 5G-RANGE channel model from D3.1 [2]. For the channel coding, a modified version of the 5G NR Polar code is chosen because of its outstanding performance in the application scenario and comparatively low implementation complexity. GFDM is chosen as waveform, because an evaluation of candidate waveforms with respect to the requirements reveals that GFDM is the candidate waveform, which fulfils all requirements and simultaneously yields the highest spectral efficiency. Furthermore, the flexibility of GFDM is also an interesting feature, since the waveform can cover OFDM and SC-FDM, which are used in LTE and 5G New Radio, as corner cases of its configuration. In addition, a novel low complexity, FFT based, implementation strategy for GFDM modems is proposed in order to facilitate affordable hardware implementations, which are essential for the economic success of the project. A major contribution of this work consists of the adaptive time-frequency resource grid, which is specifically designed for the application and can be used within TV channels in Europe and Brazil alike. Furthermore, novel GFDM channel estimation algorithms are proposed and evaluated. The Pilot- and CP-aided channel estimation algorithm can even outperform typical OFDM implementations, by utilizing information from the CP, which is usually discarded. Moreover, suitable multiple antenna signal processing schemes, which enable the utilization of diversity and multiplexing gains to enhance robustness and data rates, respectively, are specified. The application of dual polarized antennas, which allows to virtually double the number of antennas, is proposed to be used in combination with the 5G-RANGE PHY. A detailed comparison of the benefits and drawbacks of using dual-polarized antennas is provided.

List of Authors

Ahmad Nimr (TUD)

Alexandre Ferreira (INATEL)

Alexandre Matos Pessoa (UFC)

Ana-Belen Martinez (TUD)

André Lima Férrer de Almeida (UFC)

Bruno Sokal (UFC)

Carlos Filipe Moreira e Silva (UFC)

Jorge Seki (CPqD)

Juan Francisco Esteban (TID)

Juliano Ferreira (INATEL)

Luciano Mendes (INATEL)

Nathália Figueiredo (CPqD)

Peter Neuhaus (TUD)

Shahab Ehsanfar (TUD)

Wheberth Dias (INATEL)

Yaning Zou (TUD)

Table of Contents

Executive Summary	3
List of Authors	4
Table of Contents	5
List of Figures	7
Definitions and abbreviations.....	9
1 Introduction	12
1.1 Physical layer architecture.....	12
1.2 Deliverable structure	13
2 Channel coding for 5G-ACRA	14
2.1 Performance comparison	14
2.1.1 Simulation framework	14
2.1.2 Performance evaluation	16
2.2 Selection of channel coding scheme.....	18
2.3 Definition and specification of 5G-ACRA.....	18
2.3.1 Encoding and decoding	19
2.3.2 Rate matching	19
2.3.3 Channel interleaving.....	20
2.3.4 Summary	20
2.4 Discussions and future perspectives	21
3 Waveform and frame structure for 5G-FlexNOW.....	22
3.1 Waveforms	22
3.1.1 OFDM	22
3.1.2 B-OFDM	24
3.1.3 F-OFDM.....	31
3.1.4 GFDM Waveform	33
3.1.5 Waveform Comparisons.....	34
3.2 Flexible frame structure.....	42
3.2.1 Frame structure.....	42
3.2.2 Pilot signals	48
3.3 Definition and specification of 5G-FlexNOW	49
3.4 Discussions and future perspectives	50
4 Algorithms for 5G-IR2A.....	51
4.1 Synchronization.....	51
4.2 Channel estimation	52

4.2.1	Interference-free pilots insertion	52
4.2.2	Advanced Pilot- and CP-aided channel estimation for non-orthogonal waveforms	53
4.2.3	Performance evaluation	55
4.3	Definition and specification of 5G-IR2A	57
4.4	Discussions and future perspectives	57
5	MIMO techniques for 5G-MIMORA	58
5.1	Diversity schemes.....	58
5.1.1	Space-Time code performance	60
5.2	Multiplexing schemes.....	61
5.2.1	Introduction to zero-forcing and least minimum mean square error algorithms	62
5.2.2	Introduction to maximum likelihood and Sphere Decoder algorithms	63
5.2.3	Spatial Multiplexing performance	63
5.3	Impact of dual-polarized antennas on the channel capacity	65
5.3.1	Simulation Results.....	66
5.4	Definition and specification of 5G-MIMORA	70
5.5	Discussions and future perspectives	70
6	PHY and MAC interface	71
6.1	Downlink interaction	71
6.2	Uplink interaction	71
7	Conclusions	73
8	References	74

List of Figures

Figure 1: Overview on the 5G-RANGE PHY.....	12
Figure 2: Overview on FEC simulation framework architecture.	15
Figure 3: Performance comparison on AWGN channel for a block size of 1024/1056 (Polar/LDPC) on the left side and for a code rate of $R=3/4$ and different block sizes on the right side.	17
Figure 4: Performance comparison on LOS channel model for a block size of $B=1024/1056$ (Polar/LDPC) on the left side and for a code rate of $R=3/4$ and different block sizes on the right side.	17
Figure 5: Performance comparison on NLOS channel model for a block size of $B=1024/1056$ (Polar/LDPC) on the left side and for a code rate of $R=3/4$ and different block sizes on the right side.	17
Figure 6: Internal architecture of 5G-ACRA.....	18
Figure 7: Illustration of circular buffer rate matching scheme for 5G NR Polar code from [12].....	19
Figure 8: 5G-ACRA Channel interleaver based on writing the code words row wise into a triangular matrix V and reading the matrix column wise before transmission. Illustration taken from [12]......	20
Figure 9: OFDM system block diagram.....	23
Figure 10: OOB of an OFDM signal.....	24
Figure 11: B-OFDM modulation - TTI proposed structure.....	25
Figure 12: B-OFDM modulation - signal generation and mapping (time domain).....	25
Figure 13: B-OFDM modulation - signal generation and mapping (frequency domain).....	26
Figure 14: B-OFDM transmitter chain.....	26
Figure 15: Coarse synchronization algorithm.	28
Figure 16: Fine synchronization algorithm.	29
Figure 17: BLER comparison of OFDM and B-OFDM.	30
Figure 18: Throughput comparison of OFDM and B-OFDM.....	31
Figure 19: F-OFDM block diagram for the downlink.....	32
Figure 20: Power spectrum of the F-OFDM signal with two sub-bands.....	33
Figure 21: Comparison between the power spectrum of the GFDM, OFDM, B-OFDM and F-OFDM waveforms.	35
Figure 22: Comparison between the power spectrum of the GFDM, OFDM, B-OFDM and F-OFDM waveforms with windowing.	36
Figure 23: Comparison in number of CMs for conventional and FFT-based implementation.	38
Figure 24: SER performance of the waveforms under AWGN channel.	39
Figure 25: SER performance of the waveforms under 5G-RANGE LOS and NLOS channel models.	40
Figure 26: Frame structure in time domain showing the alignment of multiple numerologies.	42
Figure 27: 5G-RANGE resource grid and fragmented spectrum usage.....	44
Figure 28: Position of channel estimation reference signals on the time-frequency grid.	48

Figure 29: PSS in the time-frequency grid. The parameters needed to extract the PSS are provided by the control channel.	51
Figure 30: Example of IFPI scheme, which illustrates, why the pilots should be allocated in the middle of the subcarrier to avoid ICI from adjacent subcarriers.	53
Figure 31: Illustration of the redefinition of TN'' as a circulant matrix CN'' , which does not invalidate yN' [40].	54
Figure 32: Evaluation of IFPI channel estimation performance in terms of SER for estimated and perfect CSI over AWGN and 5G-RANGE LOS and NLOS channel models.	56
Figure 33: Evaluation of IFPI channel estimation performance over the NLOS channel model with mobility in the range [0,160] km/h. The evaluation uses the numerology ID=4 from the 5G-FlexNOW specification in Table 17.	56
Figure 34: 2x2 MIMO system.	58
Figure 35: Basic representation of STC.	59
Figure 36: STC simulation on performance gain for GFDM modulation.	61
Figure 37: Basic architecture of spatial multiplexing.	61
Figure 38: Spatial Multiplexing performance comparison for ZF, MMSE and ML algorithm and f-OFDM and GFDM modulation.	64
Figure 39: a) SISO with dual-polarized antennas. b) Channel between the vertical and horizontal polarized antennas, considered separately.	65
Figure 40: Channel throughput for a Tx power of 49 dBm, NLOS case.	67
Figure 41: Channel throughput for a Tx power of 53 dBm, NLOS case.	67
Figure 42: Channel throughput for a Tx power of 49 dBm, LOS case.	68
Figure 43: Channel throughput for a Tx power of 53 dBm, LOS case.	68
Figure 44: Channel throughput for a Tx power of 21 dBm, NLOS case.	69

Definitions and abbreviations

3GPP (3rd generation partnership project).....	14
5G-RANGE (remote area access network for 5th generation).....	12
ACRA (advanced coding for remote areas)	12
ASICs (application specific integrated circuits).....	37
AWGN (additive white Gaussian noise)	16, 54
BER (bit-error ratio)	15
BLAST (Bell-Labs layered space-time architecture)	58
BLER (block-error ratio).....	15
B-OFDM (block OFDM)	24
CFO (carrier frequency offset)	25, 51
CMs (complex multiplications).....	37
CoMP (coordinated multipoint)	24
CP (cyclic prefix)	13, 23
CS (cyclic suffix)	35
CSI (channel state information)	28, 47, 55
DCI (downlink control information)	71
DFT (discrete Fourier transform)	23, 37, 54
DMRS (demodulation reference signal).....	48
DP (dual-polarized)	66
DSP (digital signal processing)	37
EPA (extended pedestrian A)	29
EVA (extended vehicular A)	29
FAP (femtocell API)	71
FD (frequency domain)	37
FDD (frequency division duplexing)	42
FEC (forward error correction)	14
FER (frame-error ratio)	55
FFT (fast Fourier transform)	25
FlexNOW (flexible non-orthogonal waveform modulator/demodulator)	12
FPGAs (field-programmable gate arrays)	37
GFDM (generalized frequency division multiplexing)	14
gNB (next generation NodeB).....	45
IAI (inter-antenna interference).....	52
ICI (inter-carrier interference).....	24, 52
IFFT (inverse fast Fourier transform)	23, 37
IFPI (interference free pilots insertion)	15, 52
IR2A (inner receiver for remote areas applications)	13
ISI (inter-symbol interference).....	23, 24, 52, 54
LLR (log-likelihood ratio).....	15
LMMSE (linear minimum mean square error).....	55

LO (local oscillator)	51
LOS (line-of-sight)	16
MAC (medium access control)	12
MCS (modulation and coding scheme)	21, 50, 73
MF (matched filter)	34
MIB (master information block)	48
MIMO (multiple input multiple output)	12, 58
MIMORA (multiple-input multiple-output techniques for remote areas applications)	13
ML (maximum likelihood)	62
MMSE (minimum mean square error)	34, 58
MSA (min-sum-algorithm)	14
NID (NR cell identity)	52
NLOS (non-line-of-sight)	16
OOB (out-of-band)	12, 23
OSTBC (orthogonal space-time block)	65
PAPR (peak-to- average-power ratio)	53
PBCH (primary broadcast channel)	48
PDCCH (physical downlink control channel)	71
PDU (packet data unit)	71
PHY (physical layer)	12
PIC (parallel-interference-cancellation)	55
PoC (proof-of-concept)	12
PRB (physical resource block)	66
PSD (power spectral density)	53
PSS (primary synchronization signal)	48
PUCCH (physical uplink control channel)	72
QAM (quadrature amplitude modulation)	15
RB (resource block)	43
RE (resource elements)	44
SAP (service access point)	71
SCL (successive cancelation list)	14
SCS (subcarrier spacing)	42
SD (sphere decoder)	63
SDR (software defined radio)	37
SER (symbol-error ratio)	15, 55
SFO (sampling frequency offset)	51
SISO (single input single output)	15, 58
SM (spatial multiplexing)	58
SP (single-polarized)	66
SPA (sum-product-algorithm)	14
SR (sampling rate)	51
SSB (synchronization signal block)	48
SSS (secondary synchronization signal)	48

STC (space-time coding).....	58
STO (sampling time offset).....	51
TBs (transport blocks).....	71
TD (time domain).....	37
TLV (tag-length-value)	71
TR-STC (time reversal space time coding).....	58
TTI (transmission time interval).....	24
TVWS (TV white spaces)	12
UCI (uplink control information).....	72
UE (user equipment)	51
UHF (ultra high frequency).....	12
VHF (very high frequency)	12
WP (work package).....	12
ZC (Zadoff-Chu)	28
ZF (zero forcing)	15, 58

1 Introduction

The goal of the 5G-RANGE (remote area access network for 5th generation) project is to enable the 5G network to provide an economically viable solution for Internet access in remote and rural areas in Europe and Brazil, which have been unconnected or underserved so far. In order to achieve this, a long range cell network with cell radii of 50 km and beyond, utilizing TVWS (TV white spaces) in the VHF (very high frequency) and UHF (ultra high frequency) bands, which exhibit very good long range propagation characteristics, is proposed.

The main challenges on the PHY (physical layer) result from the dynamic usage of fragmented spectrum and the severe distortions resulting from the long-range channel with a high delay spread. Consequently, a flexible waveform providing high spectrum agility, low OOB (out-of-band) emissions and a high spectral efficiency, despite the high delay spread, has to be used in order to efficiently utilize TVWS. Furthermore, a robust yet affordable channel coding scheme, as well as suitable inner receiver algorithms and MIMO (multiple input multiple output) techniques, have to be applied to achieve reliable communication over the channel conditions of the targeted scenario.

This deliverable continues the work of D3.1 [2] and provides an investigation and specification of the 5G-RANGE PHY. The main goal and novelty of this work is to tailor a 5G PHY to the use cases, requirements and channel model of the application, which were obtained in [1] and [2], respectively. Furthermore, this deliverable also considers the interface to the MAC (medium access control) layer, which is developed in WP (work package) 4 and provides input to the PoC (proof-of-concept) demonstrator of WP 6. The PoC will be used to demonstrate the power of the proposed system, including the PHY. However, only a subset of the 5G-RANGE PHY will be implemented for the PoC.

1.1 Physical layer architecture

This section provides an overview on the PHY building blocks and a short introduction to each block. The connections and interactions between the blocks can be observed in Figure 1:

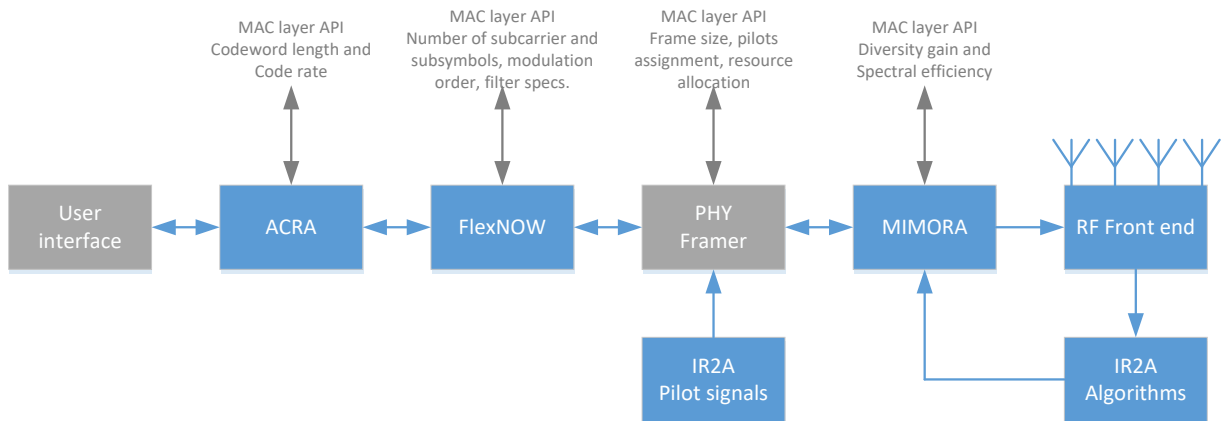


Figure 1: Overview on the 5G-RANGE PHY.

- 5G-ACRA (advanced coding for remote areas) mainly performs encoding and decoding of the payload bits using a suitable channel coding scheme. The main goal is to find a scheme which provides robustness and yet allows for a low complexity implementation. Furthermore, 5G-ACRA also performs interleaving and de-interleaving of the code words, to enhance robustness over frequency selective channels as well as rate matching and rate recovery.
- 5G-FlexNOW (flexible non-orthogonal waveform modulator/demodulator) is a flexible waveform modulator/demodulator. The main criteria on the waveform are low OOB emissions

and dynamic and non-continuous spectrum allocation capabilities. Furthermore, the frame structure should provide a high efficiency despite the need for a long CP (cyclic prefix), because of the high delay spread of the channel. In addition, the frame structure should be able to provide an adaptive time-frequency resource grid for coexistence with primary users, i.e., TV signals.

- 5G-IR2A (inner receiver for remote areas applications) contains the inner receiver algorithms for time and frequency synchronization as well as channel estimation.
- 5G-MIMORA (multiple-input multiple-output techniques for remote areas applications) performs MIMO signal processing to obtain a diversity or multiplexing gain. Especially, obtaining a diversity gain is important to enhance the systems robustness over long range channels, which is a key requirement on the PHY.

1.2 Deliverable structure

The remainder of this document is organized as follows:

- Section 2 continues the evaluation of channel coding schemes from [2] in a more practical 5G-RANGE scenario, including the 5G-RANGE channel model from [2]. Furthermore, the final specification of 5G-ACRA is provided in this section.
- Section 3 continues the evaluation of suitable waveforms for the application in 5G-FlexNOW from [2]. Waveforms candidates are compared with respect to OOB emissions and a suitable waveform is chosen also based on complexity and flexibility considerations. Furthermore, this section provides a suitable adaptive time frequency resource grid for 5G-RANGE. The detailed specifications of 5G-FlexNOW conclude this section.
- Section 4 introduces synchronization and channel estimation algorithms for the application in 5G-IR2A. Two advanced GFDM channel estimation procedures are introduced and their performance is evaluated on the 5G-RANGE channel model. The section is closed by the specifications of 5G-IR2A.
- Section 5 introduces MIMO signal processing schemes for 5G-MIMORA. The section introduces and compares diversity and multiplexing schemes, which are suitable for the application in 5G-MIMORA. Furthermore, the option of using dual-polarized antennas for 5G-RANGE is explored, which allows to virtually double the effective number of antennas. The specifications of 5G-MIMORA conclude this section.
- Section 6, provides an overview on the MAC-PHY interface.
- Finally, section 7 summarizes the contributions and conclusions of this deliverable.

2 Channel coding for 5G-ACRA

This section continues the evaluation of FEC (forward error correction) schemes for the application in 5G-ACRA from Section 4 of [2]. The goal is to find a FEC scheme that provides robustness despite the severe distortions caused by the long-range channel (cf. Section 2 in [2]) and yet comes with moderate decoding complexity to enable the economic success of the project. In D3.1 three possible FEC schemes are introduced, namely Turbo, Polar and LDPC codes. By comparing their respective performance on an AWGN channel it is shown that Turbo codes cannot compete with the other two schemes and, hence, they are not further investigated for the application in 5G-ACRA. Moreover, the investigation shows that the 5G NR Polar code outperforms the investigated 5G NR LDPC code for small code block sizes B , a result which was also obtained in the performance evaluation within 3GPP (3rd generation partnership project) [3]. The overall performance of both schemes is found to be similar in D3.1.

In the remainder of this section the performance comparison of Polar and LDPC codes is firstly continued in a more realistic setting, which includes the channel model developed in [2] and the waveform chosen for 5G-FlexNOW in 3.1. Secondly, based on the results of the performance comparison, a FEC scheme for the application in 5G-ACRA is chosen. Then, the complete channel coding block 5G-ACRA is specified and finally a discussion of the results concludes this section.

2.1 Performance comparison

This section provides a performance comparison of the 5G NR Polar and the 5G NR LDPC code using simulations in a more realistic setting as compared to D3.1. The goal is to compare the performance in a practical application setting and using nearly the full transceiver chain including practical channel estimation, demodulation and channel coding algorithms. This is the main difference to the performance evaluation in the previous deliverable D3.1, where the goal was to determine the fundamental performance limits of the different channel coding schemes.

2.1.1 Simulation framework

A simulation framework written in *MATLAB* provides the performance comparison. Large parts of this simulator are available under an open-source license: To simulate the 5G NR Polar code an open-source implementation¹ by the University of Southampton (UK) is utilized. This implementation is compliant to the 3GPP specifications in [4]. Furthermore, it includes an implementation of the SCL (successive cancellation list) decoding algorithm from [5] with the option to use a *min-sum* approximation. For the simulation of the 5G NR LDPC code, a new library has been implemented within the project. The library is also publicly available on *GitHub*². Since the last deliverable, this implementation has been extended to support more code rates and block sizes and the decoder has been extended by a MSA (min-sum-algorithm) implementation in addition to the existing SPA (sum-product-algorithm), both of which are implemented according to [6]. Also, for the proposed channel model and GFDM (generalized frequency division multiplexing) modulation³, libraries were developed and extended within the work of WP 3.

¹ Available: <https://github.com/robmaunder/polar-3gpp-matlab>

² Available: <https://github.com/vodafone-chair/5g-nr-ldpc>

³ Available: <https://github.com/vodafone-chair/gfdm-lib-matlab>

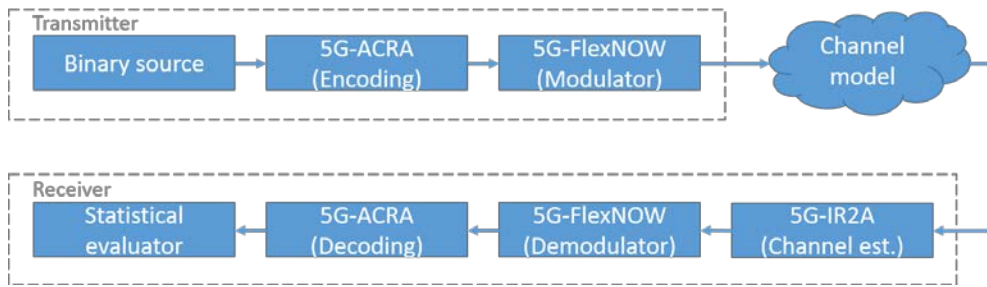


Figure 2: Overview on FEC simulation framework architecture.

Figure 2 provides an overview on the simulation framework. The first block is a random binary source to generate data bits. The second block is 5G-ACRA, which performs FEC encoding and interleaving of the code words. The goal of this section is to evaluate the performance of 5G-ACRA. The last block at the transmitter is 5G-FlexNow, which performs mapping to 64 QAM (quadrature amplitude modulation) symbols and consecutive GFDM modulation. An overview on the GFDM parameters is provided in Table 1. After passing the channel model, which is implemented according to the specification in [2], 5G-IR2A performs channel estimation at the receiver. For this purpose, 5G-IR2A implements GFDM channel estimation using the IFPI (interference free pilots insertion) scheme, which is introduced in Section 4.2.1. Afterwards, 5G-FlexNOW performs ZF (zero-forcing) GFDM demodulation using the estimated channel impulse response. Then, bit-wise LLR (log-likelihood ratio) values are obtained using an optimized soft information de-mapper, which limits the maximum LLR range to avoid numerical instabilities in the decoders⁴. After de-interleaving, 5G-ACRA performs 5G NR Polar or 5G NR LDPC decoding, respectively. Both decoders are configured to use the *Min-Sum approximation* in all evaluations presented in this deliverable in order to obtain practical⁵ performance comparisons. The last block performs statistical performance evaluation in terms of the following metrics:

- QAM SER (symbol-error ratio), which can be used to evaluate the performance of channel estimation and to determine how severe the received signal is distorted by the channel.
- BLER (block-error ratio), which is the ratio of erroneous to total number of code word blocks. This metric yields the main performance comparison, because it is the most important metric with respect to the overall system performance.
- BER (bit-error ratio), which can also be used to evaluate the performance of the FEC schemes.

Note that the simulations in this section consider only SISO (single input single output) systems, hence 5G-MIMORA is not part of the simulation framework.

⁴ Evaluations within the project have shown that this can significantly enhance the performance of the FEC schemes and, hence, this is an improvement as compared to [2].

⁵ In practical hardware implementations, the SPA algorithm is nearly always relaxed to the MSA algorithm, which does not involve the non-linear hyperbolic tangent function (cf. e.g. [5]).

Table 1: GFDM modulation settings used in the simulation framework. The simulated GFDM numerology corresponds to numerology ID=0 in Table 17, which is introduced in Section 3.3.

Parameter	Value
GFDM subcarriers	16384
GFDM subsymbols	4
Bandwidth	30.72 MHz
CP duration	141.7 μ s
CS duration	25 μ s
Window duration	16.67 μ s
Pilot spacing (time/freq.)	4/2

2.1.2 Performance evaluation

This section provides a performance evaluation of the considered 5G NR Polar and 5G NR LDPC code using the simulation framework and settings, which are introduced in the previous section. Firstly, the performance is evaluated in terms of BLER on an idealistic AWGN (additive white Gaussian noise) channel. The BLER is plotted versus the average energy per QAM symbol to noise power spectral density ratio, which is denoted as E_S/N_0 . Results are shown in Figure 3 (left-hand side). It can be observed that the Polar code outperforms the LDPC code for nearly all code rates at the considered block sizes of $B = 1024/1056$ for the Polar and LDPC code, respectively. A comparison for a fixed code rate of $R = 3/4$ and a varying code block sizes is also provided in Figure 3 (right-hand side). Remarkably, it can be observed that the Polar code outperforms the LDPC code for all block sizes. This is a novel result as compared to the previous evaluations in [2]. The difference between the evaluations previous and the here provided results is that the new evaluation considers channel estimation errors, an optimized LLR de-mapper ensuring numerical stability and most importantly makes use of the Min-Sum approximation in the decoders. The results show that under these practical conditions, the Polar code outperforms the LDPC code on an AWGN channel.

To obtain more practical performance evaluations and to ensure a robust operation of the 5G-RANGE system over long distances (as required by Req-F.m.8 [1]) the performance is further evaluated using the general LOS (line-of-sight) and NLOS (non-line-of-sight) channel models, developed in [2].

A performance comparison for different code rates on the LOS channel model is depicted in Figure 4 (left-hand side). It can be observed that the LOS channel is more distorting and requires a higher transmit power to achieve a similar BLER as compared to the AWGN channel. Moreover, the Polar code outperforms the LDPC code for all considered code rates and a block size of $B = 1024/1056$. Figure 4 (right-hand side) provides a performance comparison for different code block sizes B . Surprisingly, the gain of using a larger block size is marginal. E.g. switching from $B = 1024$ to $B = 4096$ yields hardly any gain. The performance increase is close to linear for a wide range of E_S/N_0 . This indicates that the channel is diversity limited. Therefore, using diversity schemes, as introduced in Section 5.1, could significantly increase the performance.

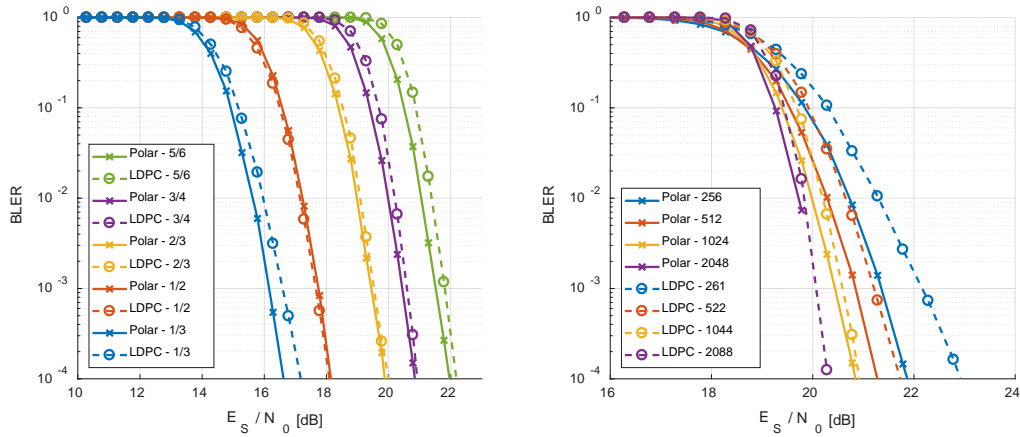


Figure 3: Performance comparison on AWGN channel for a block size of 1024/1056 (Polar/LDPC) on the left side and for a code rate of $R=3/4$ and different block sizes on the right side.

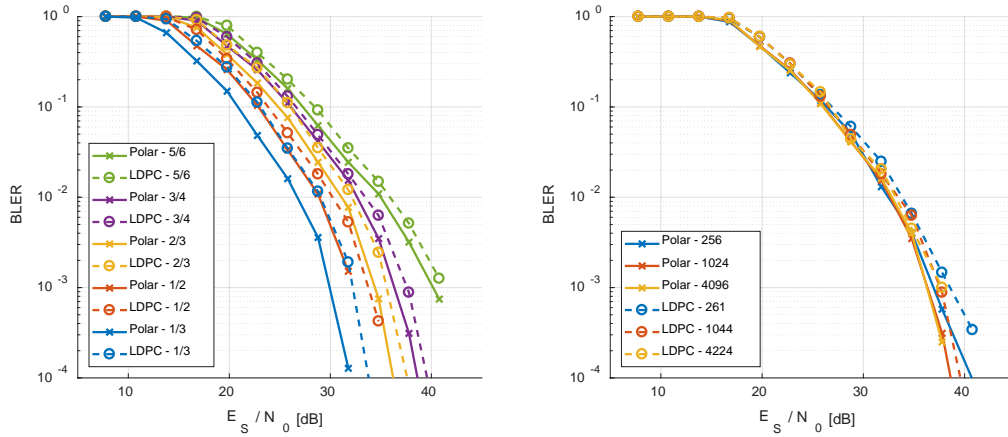


Figure 4: Performance comparison on LOS channel model for a block size of $B=1024/1056$ (Polar/LDPC) on the left side and for a code rate of $R=3/4$ and different block sizes on the right side.

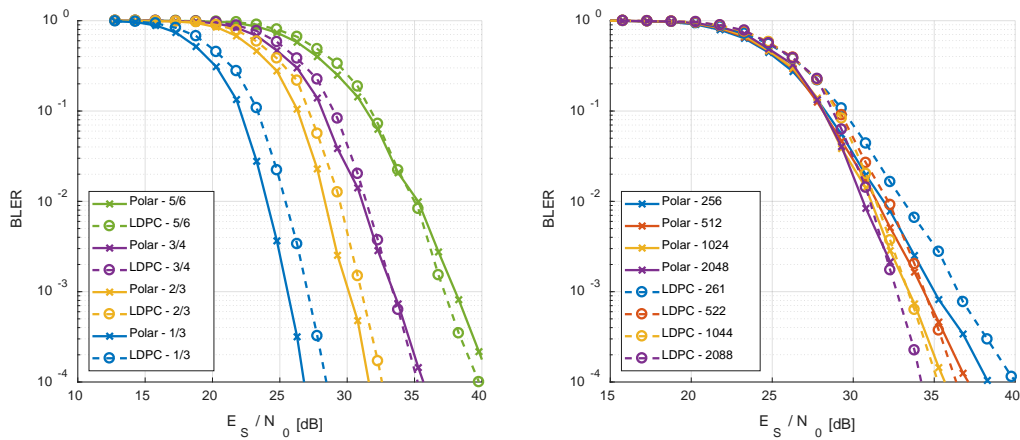


Figure 5: Performance comparison on NLOS channel model for a block size of $B=1024/1056$ (Polar/LDPC) on the left side and for a code rate of $R=3/4$ and different block sizes on the right side.

The performance over the NLOS channel model is depicted in Figure 5 for different code rates (left-hand side) and different block sizes (right-hand side), respectively. The evaluation shows that the Polar code outperforms the LDPC code for lower code rates, whereas for a code rate of $R = 5/6$ the LDPC code outperforms the Polar code at high E_S/N_0 . Comparing the block size, it can be observed that the Polar code outperforms the LDPC code for small block sizes, whereas the performance of both schemes converges for longer block sizes.

2.2 Selection of channel coding scheme

The performance evaluation in Section 2.1.2 in a typical 5G-RANGE scenario with practical receiver algorithms leads to the following observations:

1. 5G NR Polar code slightly outperforms 5G NR LDPC code under many conditions in the meaningful operating regime;
2. 5G NR Polar code outperforms 5G NR LDPC code significantly for block sizes below $B = 1024/1056$, whereas the performance converges for larger block sizes;
3. In none of the investigated cases is the 5G NR Polar code significantly outperformed by the 5G NR LDPC code.

Based on the observations above, it can be expected that the 5G NR Polar code yields a better performance and a higher robustness for the application in the 5G-RANGE PHY. In addition, the evaluation reveals that the application of two channel coding schemes does not seem to be justified, because the performance difference is never significant (cf. to observation 3). Therefore, our approach to specify a single channel coding scheme in order to reduce implementation complexity, as opposed to 5G NR, which implements two channel coding schemes, is justified (cf. [2]).

The choice of FEC scheme for 5G-ACRA should also consider the implementation complexity, because the system cost is of great importance for the success of the technology and could affect the economic feasibility of the system. A comparison in terms of complexity between the 5G NR Polar and 5G NR LDPC code is already provided in Section 4 of [2], where the complexity of the Polar code is found to be acceptable. For small block sizes, the complexity of the Polar code can even be considered low. As a result, the application of the 5G NR Polar code is also feasible with respect to the implementation complexity. Furthermore, the performance investigation reveals another possibility to further reduce the complexity: since the Polar code outperforms the LDPC code for smaller block sizes (cf. observation 3 from above), the chosen block size could be reduced as compared to the necessary block size for the LDPC code, which in turn reduces the implementation complexity. Because of the findings above, the 5G NR Polar code is chosen as single FEC scheme for the application in 5G-ACRA.

2.3 Definition and specification of 5G-ACRA

This section specifies the operation of 5G-ACRA. Figure 6 provides an overview on the internal architecture of 5G-ACRA.

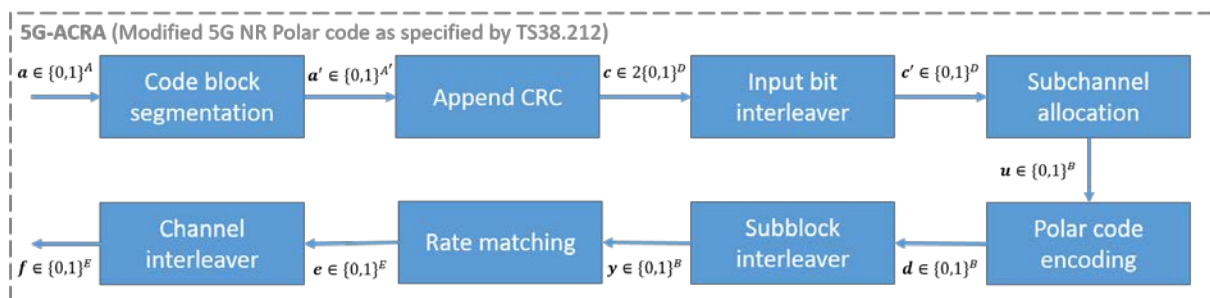


Figure 6: Internal architecture of 5G-ACRA.

2.3.1 Encoding and decoding

Our proposal for the Polar code encoding is based on Arikan's initial proposal in [7] with an encoding complexity of $O(B \cdot \log_2 B)$. The underlying operation, the so-called channel polarization operation has already been introduced in Section 4.3 of D3.1 [2]. The implementation of this scheme is straightforward and the complexity is already very competitive. A more advanced systematic encoding scheme can be found in [8]. The authors introduce a low-complexity, highly parallel and flexible encoding algorithm and prove its correctness. Furthermore, they introduce and evaluate the performance of software and real-time hardware implementations with very low complexity, which can achieve throughputs of 10 Gbps and 29 Gbps, respectively.

For Polar code decoding, we propose to use the implementation from [5], which provides a widely adopted SCL decoder architecture for CRC-aided Polar codes. By restricting the list size L to powers of two, the decoder can utilize efficient radix-2L sorters, which enables hardware efficient implementations. Nevertheless, since list decoders are somewhat serial decoders, it is very challenging to parallelize their implementations. Therefore, iterative decoder, e.g. based on belief propagation could be a good choice for future decoding algorithms [9]. Promising approaches include [10], which provides a belief propagation list decoder with the best performance so far reported and exhibits a highly parallel architecture, which is advantageous for implementation.

2.3.2 Rate matching

Rate matching is defined as the process of selecting the actual transmission bits after channel coding, such that they match exactly the assigned physical transmission resources. The inverse process at the receiver is known as *rate recovery*. Rate matching in 5G-ACRA is based on the 5G NR Polar code rate matching scheme, which utilizes a circular buffer, as specified in [11]. Figure 7 provides an overview on the rate matching scheme. The input to the rate matching unit is denoted as \mathbf{y} and describes a binary vector of length D . This vector is written into a circular buffer of similar length. The rate matching procedure reads out certain parts of the buffer for transmission. It can be summarized as follows [12]:

- *Puncturing*: Only the last part of the code word is transmitted. The code word is punctured by the first $U = B - E$ bits. Applied for $E \leq B$ and $R \leq 7/16$.
- *Shortening*: Only the first part of the code word is transmitted. The code word is shortened by the last $U = B - E$ bits. Applied for $E \leq B$ and $R > 7/16$.
- *Repetition*: Repetition of the first $U = E - B$ bits. Applied for $E > B$.

The performance of the 5G NR rate matching scheme can be slightly enhanced by tweaking some parameters of the algorithm as e.g. shown in [13].

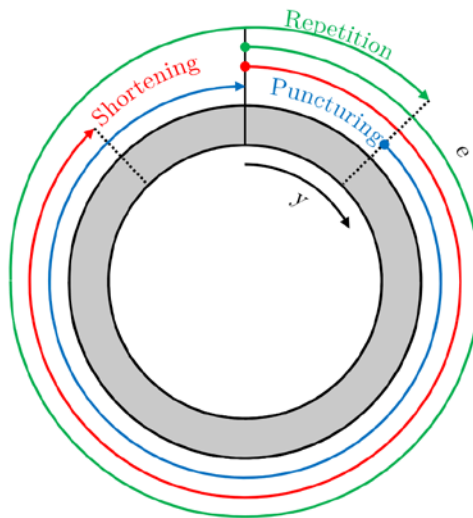


Figure 7: Illustration of circular buffer rate matching scheme for 5G NR Polar code from [12].

2.3.3 Channel interleaving

Channel interleaving for 5G-ACRA is based on [11]. The goal is to improve the robustness of the channel coding scheme, especially for higher order modulations, where many consecutive bits are mapped to a single constellation symbol, by a randomized shuffling of the code word bits. Therefore, a triangular block interleaver is utilized. The interleaver is defined by a square upper triangular matrix \mathbf{V} of size $T \times T$, where T is defined as the smallest integer, such that it holds $T(T + 1)/2 \geq E$. The corresponding value of T can be obtained numerically as

$$T = \left\lceil \frac{\sqrt{8E + 1} - 1}{2} \right\rceil \quad (1)$$

Now the interleaver writes the code word after rate matching \mathbf{e} , row wise into \mathbf{V} . The remaining part at the bottom (marked grey in Figure 8) is filled with *NULL* values. Then, the interleaved code word \mathbf{f} is obtained by reading \mathbf{V} column wise, where the *NULL* value entries are skipped [12].

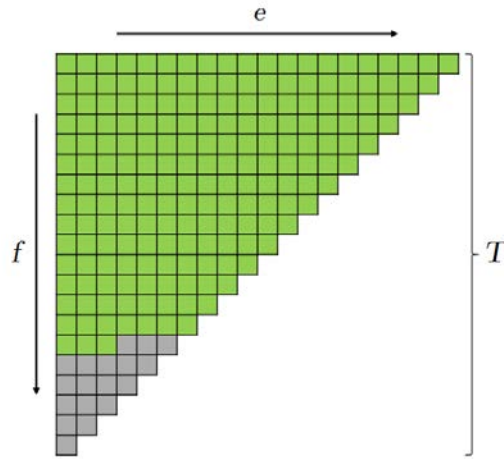


Figure 8: 5G-ACRA Channel interleaver based on writing the code words row wise into a triangular matrix \mathbf{V} and reading the matrix column wise before transmission. Illustration taken from [12].

2.3.4 Summary

In this section, we provided the specification of 5G-ACRA. The specifications are mainly based on the 5G NR Polar code, which is applied only on the control channel in 5G NR. For code block segmentation, CRC appending and input bit interleaving we utilize the specifications of 3GPP for 5G NR. For encoding, the algorithm proposed by Arikan is utilized, which allows efficient Polar encoding for code power of two block sizes B . For decoding, we utilize the SCL decoder from [5], which utilizes efficient radix-2L sorting, hence, restricts the list size to powers of two. Rate matching utilizes writing and reading into a circular buffer and channel interleaving adopts the scheme from 5G NR, which writes row wise in an upper triangular matrix and reads the data out column wise. Both schemes allow for an efficient hardware implementation. The detailed specifications are summarized in Table 2.

Table 2: Specification of 5G-ACRA.

5G-ACRA	
Fixed parameter	Description
FEC Scheme	5G NR CRC-aided Polar code according to [11]
Encoder	Arikan Systematic Encoder [7] (optional: Systematic low-complexity encoder [8])
Decoder	SCL decoder from [5]
Rate matching	Circular buffer-based rate matching according to [11] (optional: Enhanced by proposal from [13])
Interleaver	Upper triangular matrix-based channel interleaver according to [11], [12]
Variable parameter	Description
Block size B	Length of the code words, which are the output of 5G-ACRA encoding. Valid range is $B \in \{256, 512, 1024, 2048, 4096, 8192\}$.
Code rate $R=D/B$	Ratio of number of information bits D to total number of bits per block B . Valid range is $R \in \{\frac{1}{3}, \frac{1}{2}, \frac{2}{3}, \frac{3}{4}, \frac{5}{6}\}$.
List size L	SCL decoder list size to trade-off performance and complexity. Valid range is $L \in 2^n, n \in \{0, 1, \dots, 5\}$ with default value $L_0 = 2^3 = 8$.

2.4 Discussions and future perspectives

In this section, we provided the specification of 5G-ACRA as well as a performance evaluation. Despite the fact that we utilize only a single FEC scheme for the control and transport channel, we have shown that we can obtain a robust (cf. Section 2.1.2) yet low complexity transceiver. Polar codes seem to be a perfect choice for this task, both in terms of performance and complexity. With the proposed design of 5G-ACRA we can address all requirements for the application scenarios and use cases in terms of robustness and complexity/cost.

After the full definition of 5G-ACRA from an implementation point of view, an open task remains to define the MCS (modulation and coding scheme) table in collaboration with WP 4. This task is foreseen to be part of Task 6.1 *Software-based system integration* of WP 6.

3 Waveform and frame structure for 5G-FlexNOW

The requirements on the waveform for 5G-FlexNOW are quite different to the requirements of 5G NR. D2.1 identifies many mandatory functional requirements on the waveform, which have to be considered in the definition of 5G-FlexNOW [1]. In the following we provide a short summary of the main requirements on the waveform and frame structure:

- Waveform
 - Dynamic and non-continuous spectrum allocation (Req-F.m.5, Req-F.m.6)
 - Robust against severe multipath and high Doppler shift (Req-F.m.8)
 - High spectrum efficiency and expected QoS (Req-F.m.11)
 - Run-time configurable waveform (Req-F.m.13)
 - Robust waveform with low OOB without relying on RF filters (Req-F.m.14)
- Frame structure
 - Handle random multiple access and channel delay profile over large cells (Req-F.m.10)
 - Adaptive time-frequency resource grid (Req-F.m.13)

The remainder of this section is organized as follows: Section 3.1 compares different waveforms and chooses the most suitable waveform for the application in 5G-FlexNOW according to the requirements listed above. Then Section 3.2 introduces a suitable frame structure. Finally, this section is concluded by the specification of 5G-FlexNOW.

3.1 Waveforms

A brief introduction on the OFDM, B-OFDM, F-OFDM and GFDM waveforms is present in the previous deliverable D3.1 [2]. This section provides a more detailed comparison, before comparing their performance and selecting a suitable waveform.

3.1.1 OFDM

The OFDM waveform is an interesting solution for applications where the communications channel exhibits multiple paths. Considering the computational resources available today, the low complexity of OFDM made it a solution widely adopted in many standards and for many different scenarios. Besides, the subcarriers orthogonality eliminates the intercell and inter-user interference once the frequency and time synchronization is achieved. The equalization in the frequency domain and its simple integration with diversity and multiplexing MIMO techniques (simple due to the orthogonality) are other advantages of OFDM. This section provides an introduction to signal generation and reception techniques for OFDM as well as a discussion of pros and cons.

3.1.1.1 Operational principles of OFDM

In the general multicarrier transmission principle, the transmitted data are distributed between K subcarriers and each one transmits R_s/K symbols per second, where the symbol rate is denoted as R_s . All subcarriers are orthogonal in the frequency domain, hence

$$\sum_{n=0}^K \exp\left(j2\pi \frac{a}{K} n\right) \exp\left(j2\pi \frac{b}{K} n\right) = 0 \quad \text{for} \quad a, b \in \mathbb{N}, a \neq b, a < K, b < K, \quad (2)$$

where n represents the time samples. The truncation of the subcarriers in k samples can be seen as the use of a transmission filter $g_{TX}[n]$ with impulse response given by

$$g_{TX}[n] = u[n] - u[n - K], \quad (3)$$

where $u[n]$ is the discrete unit step function. Hence, OFDM symbols are orthogonal, i.e., non-overlapping, in the time domain. Figure 9 shows the block diagram of an OFDM system.

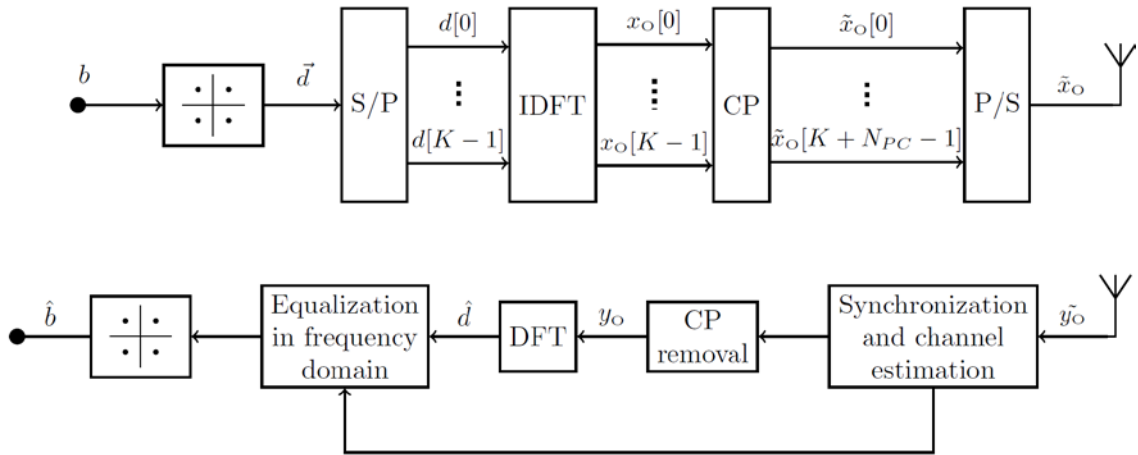


Figure 9: OFDM system block diagram.

The information bits b are mapped in symbols according to the used constellation and are organized in a vector of data $\vec{d} = [d_0, d_1, \dots, d_{K-1}]$. Each symbol from this vector modulates a single subcarrier. The combination of all the subcarriers results in the OFDM signal, defined as

$$x_o[n] = \sum_{k=0}^{K-1} d[k] \exp\left(j2\pi \frac{k}{K} n\right) \quad \text{for} \quad 0 \leq n \leq K-1. \quad (4)$$

Equation (4) can be interpreted as an IFFT (inverse fast Fourier transform) of \vec{d} , except for the absence of a normalization factor $\frac{1}{N}$. This is the key for low complexity implementations of OFDM, utilizing the fast number of efficient IFFT implementations. This operations can also be represented in the matrix form, resulting in

$$x_o = F_K^H \vec{d}, \quad (5)$$

where F_K is the DFT (discrete Fourier transform) matrix of dimension K .

A guard interval, composed of the CP (cyclic prefix) is inserted between the OFDM symbols. This CP allows to interpret the linear convolution of the transmit signal with the channel impulse response as a circular convolution. This allows to eliminate the ISI (inter-symbol interference) and makes low complexity frequency domain equalization feasible. In this case, the length of the CP must be

$$N_{CP} \geq N_{CH} - 1 \quad (6)$$

where N_{CH} is the channel impulse response length.

After the signal passes through the channel, where it suffers the effects of fading and AWGN, a process to reverse the modulation is applied to the signal at the reception chain. After the frequency and time synchronization and the removal of the CP, the received samples are processed by the DFT (discrete Fourier transform). The signal is equalized in the frequency domain, and the received bits are obtained after detection.

3.1.1.2 Analysis of Out-Of-Band emission

The OFDM waveform, despite its advantages in terms of orthogonality and low complexity, presents limitations to attempt the new demands of 5G. The high OOB (out-of-band) emissions is a limiting factor which makes it difficult to use in some applications for 5G. For example, the need for the usage of RF filters to suppress the high level of OOB emissions makes it difficult to be used in cognitive radio applications, which require low OOB emissions for coexistence with primary users. In scenarios of high data rate, the flexibility to aggregate and liberate bandwidth according to the quality of service of users is fundamental. Besides that, the use of pico and femtocells implies a high density of frequency reuse.

The high OOB results in a high level of interference that must be controlled by CoMP (coordinated multipoint) algorithms. Figure 10 shows the OOB emission of the OFDM signal with 64 subcarriers.

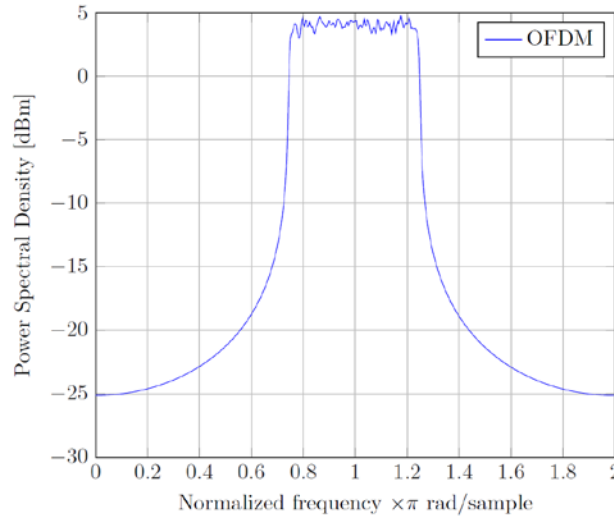


Figure 10: OOB of an OFDM signal.

3.1.2 B-OFDM

Latency reduction in mobile wireless communications requires the symbol duration reduction for OFDM signals, but the minimum CP length is limited by the maximum channel delay spread. As found out in [2], the 5G-RANGE multipath channels have a long delay spread, hence require a long CP. For this reason, we propose to use a B-OFDM (block OFDM) TTI (transmission time interval), which achieves a significant CP overhead reduction, by keeping only the CP corresponding to the first symbol and removing the remaining ones on the same TTI [14]. With this simple change, the system improves both the latency and the spectral efficiency of the system. Figure 11 shows the frame structure of the standard OFDM and the B-OFDM proposal. Note that the proposed version of B-OFDM in this section is a modified version as compared to the version, presented in [2], because the CP is taken from the first symbol and not from the end of the whole block. The implications of this are discussed in this section.

With this modification, the efficiency of both systems can be compared to quantify this improvement:

- OFDM efficiency is: $\eta_{OFDM} = N_{OFDM} / (N_{CP} + N_{OFDM})$
- B-OFDM efficiency is: $\eta_{BOFDM} = N_{sym} \cdot N_{OFDM} / (N_{CP} + N_{sym} \cdot N_{OFDM})$,

where N_{sym} is the number of OFDM symbols in a TTI, N_{cp} is the length of the CP and N_{OFDM} is the OFDM symbol length. A similar efficiency can be achieved by GFDM.

Using LTE standard values for these variables, it is possible to calculate overhead improvement for the proposed TTI structure. These values are: $N_{sym}=14$, $N_{cp}=160$ and $N_{OFDM} = 2048$ for 20 MHz bandwidth configuration. The overhead efficiency for standard OFDM would be $\eta_{OFDM} = 92.75\%$ as compared to the overhead efficiency for the proposed B-OFDM TTI structure, which would be $\eta_{BOFDM} = 99.45\%$. This shows the significant efficiency improvement of B-OFDM.

The absence of the CP in any symbols creates problems in multipath conditions. The main problems are ICI (inter-carrier interference) and ISI (inter-symbol interference). However, it is possible to cancel this effect with some signal processing, as described in the next subsections.

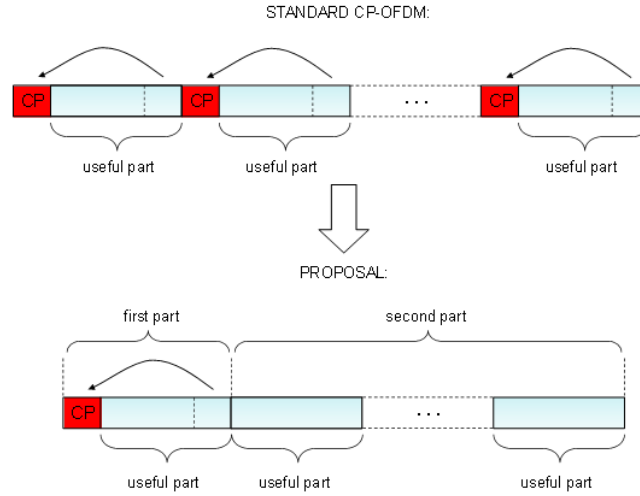


Figure 11: B-OFDM modulation - TTI proposed structure.

The fundamental difference between the proposed TTI structure and a single, longer OFDM symbol used in the B-OFDM proposal from [2] is the CFO (carrier frequency offset) compensation capability. The old proposal B-OFDM has reduced CFO correction properties due to the longer symbol length (only one FFT (fast Fourier transform) with $N_{\text{sym}} \cdot N_{\text{OFDM}}$ before the equalizer). With the proposed new structure, these capabilities remain the same as in standard OFDM, because it is determined by the FFT size over the first symbol, which is identical in both cases.

In order to fulfil Req-F.m.14, low OOB emissions from the waveform are required. At this point, the proposed structure has the same spectrum properties as standard OFDM, which introduces high interferences in adjacent channel. Therefore, in order to fulfil Req-F.m.14 it is necessary to apply additional filtering and windowing techniques.

3.1.2.1 Signal generation and mapping

The mapping of complex symbols to time-frequency resources for this new proposal varies with respect to the OFDM standard. The first OFDM symbol undergoes the same mapping process, the rest of the symbols belonging to the TTI are grouped in a single extended OFDM symbol containing the concatenated subcarriers of the original remaining OFDM symbols and the corresponding length in the time domain. Therefore, the length of the TTI is not modified, except for the deleted CPs. This is illustrated in Figure 12.

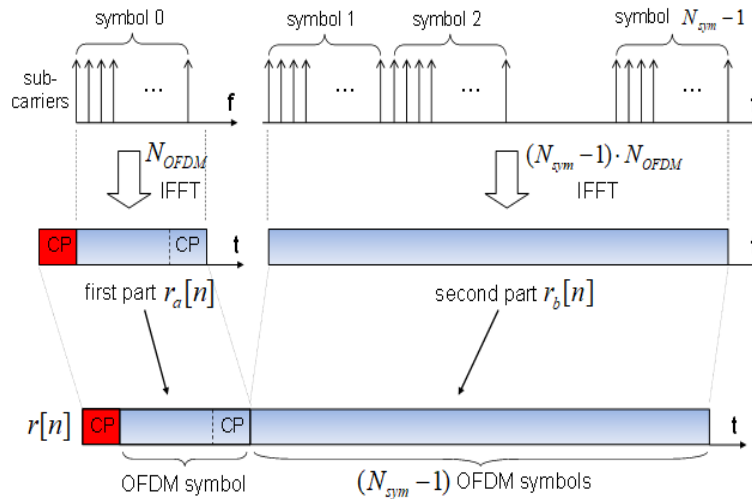


Figure 12: B-OFDM modulation - signal generation and mapping (time domain).

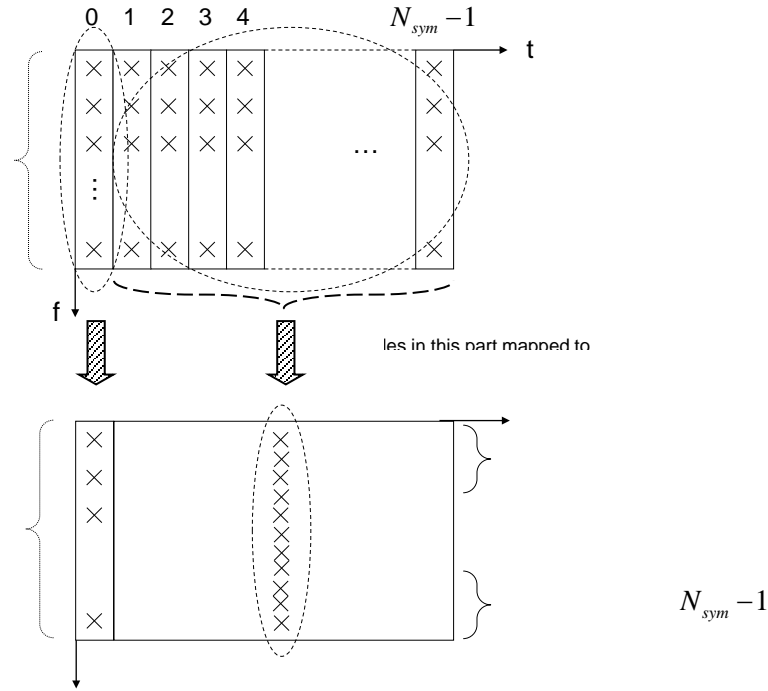


Figure 13: B-OFDM modulation - signal generation and mapping (frequency domain).

The presence of a higher number of subcarriers in the second part of the TTI results in lower frequency diversity because the subcarriers separation is lower. This can impact the performance of the FEC. To compensate this effect, it is necessary to introduce an additional interleaver after FEC encoding to improve frequency diversity upon reception. The final transmitter chain of this proposed TTI is depicted in Figure 14.

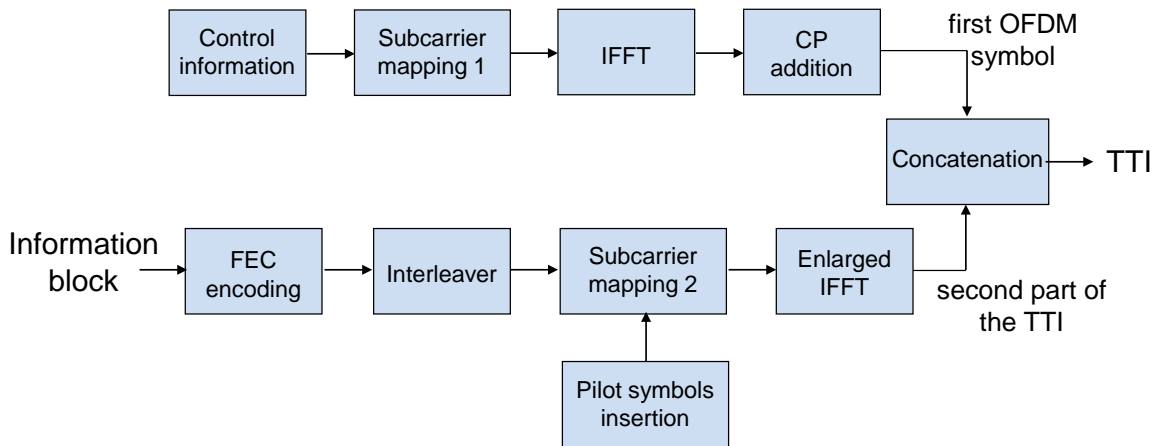


Figure 14: B-OFDM transmitter chain.

3.1.2.2 Equalization and data recovery

One critical issue in OFDM is how to deal efficiently with ISI and ICI as a result from multipath radio channel conditions. The traditional approach of OFDM is to mitigate these problems with the use of the CP at the beginning of each symbol. Due to the absence of CP in any symbol of the second part of the TTI, is necessary to implement an algorithm to mitigate ISI and ICI effect in this part of the TTI.

What follows is a detailed theoretical explanation about the signal processing necessary to equalize the received signal in order to obtain data correctly. For the proper data recovery, this equalization has to be done after the synchronization algorithm is finished.

The algorithm is based on the following steps:

- In first place, it is estimate the channel frequency response $H[f]$ using standard OFDM detection techniques with the first part of the TTI structure $r_a^{TTI}[n]$ as it was defined in the Figure 15. With this information the receiver is capable to obtain the time-domain channel impulse response $h[n] = IFFT\{H[f]\}$, obtaining the most representative multipath components of the channel.

$$h[n] = \sum_{j=0}^{N_{taps}-1} a_j \delta[n - \tau_j] \quad (7)$$

N_{taps} is the number of most significant delayed signals received, a_j is the complex amplitude of the j -th tap and τ_j is its delay associated for each tap.

- Using this channel estimation the first OFDM symbol can be reconstructed through proper equalization and demodulation, this reconstructed symbol is $s_a^{TTI}[n]$.
- To remove the ISI effect from the first part of the TTI towards the second part of the TTI, ISI effect is calculated with the following expression:

$$ISI = \sum_{j=0}^{N_{taps}-1} a_j \tilde{s}_a^{TTI}[n - \tau_j + N_{OFDM}] \quad 0 \leq n \leq \tau_{\max} \quad (8)$$

Being τ_{\max} the maximum value of the cannel delays and $\tilde{s}_a^{TTI}[n]$ is equal to $s_a^{TTI}[n]$ (First OFDM equalised symbol) for $0 \leq n < N_{OFDM}$ and zero outside. The ISI component from the first symbol OFDM can be subtracted to obtain the second part of the TTI without ISI issue ideally:

$$r_{b,ISI}^{TTI}[n] \equiv r_b^{TTI}[n] - ISI \quad (9)$$

- Besides the ISI cancelation is also necessary to restore the cyclicity of the signal to cancel the inter-carrier interferences. The cyclicity of the signal is lost due to the spread delayed signals. These delayed signals does not appear as a cyclic shifts because of the absence of the CP. The samples that are lost to the right of the TTI will be reintroduced to the left as in a circular shift register. The samples that is necessary to be reconstructed are unknown, but it can be obtained from the ISI effect towards the first OFDM symbol of the next TTI:

$$ISI^{TTI+1}[n] = r_a^{TTI+1}[n] - \sum_{j=0}^{N'_{taps}-1} a'_j \tilde{s}_a^{TTI+1}[N_{OFDM} - N_{CP} + n - \tau'_j] \quad (10)$$

Where the variables N'_{taps} , a'_j and τ'_j are the corresponding to the channel estimation of the first OFDM symbol of the next TTI. $ISI^{TTI+1}[n]$ is the ISI effect from the $r_b^{TTI}[n]$ signal towards the next TTI.

- Whit this approach is possible to obtain the data from second part of the TTI, without ISI and ICI issues:

$$r_{b,ISI,ICI}^{TTI}[n] = r_{b,ISI}^{TTI}[n] + r_a^{TTI+1}[n] - ISI^{TTI+1}[n] \quad (11)$$

It should be notice that is supposed for this algorithm that the channel frequency response estimation remains valid during the whole second part of the TTI.

3.1.2.3 Time synchronization issues

The main problem that we have to solve with this TTI structure is the synchronization. Due to the elimination of the last $(N_{\text{sym}} - 1)$ CPs, the cyclicity of the CP is lost at the second part of the TTI. Therefore, perfect synchronization is required in order to receive the data correctly for the second part of the TTI. Two stages of synchronization are carried out to ensure that this perfect synchronization is feasible in multipath conditions:

- Coarse synchronization:

At this first stage of the synchronization, we studied the correlation properties between the CP and the end of the first OFDM symbol.

To improve correlation properties, two ZC (Zadoff-Chu) sequences has been used as pilot data. One sequence is used by the fine algorithm (ZC 2) and the other is employed by the coarse algorithm (ZC 1). The second one is placed at the end of the first OFDM symbol and is replicated to the CP.

To detect the beginning of the sequence, a signal with the length of the CP is correlated with the N_{OFDM} samples that follow. This process is done by moving the windowed signal one by one sample until is reached the correlation peak. This peak indicates the start of the TTI. Figure 15 illustrates the procedure.

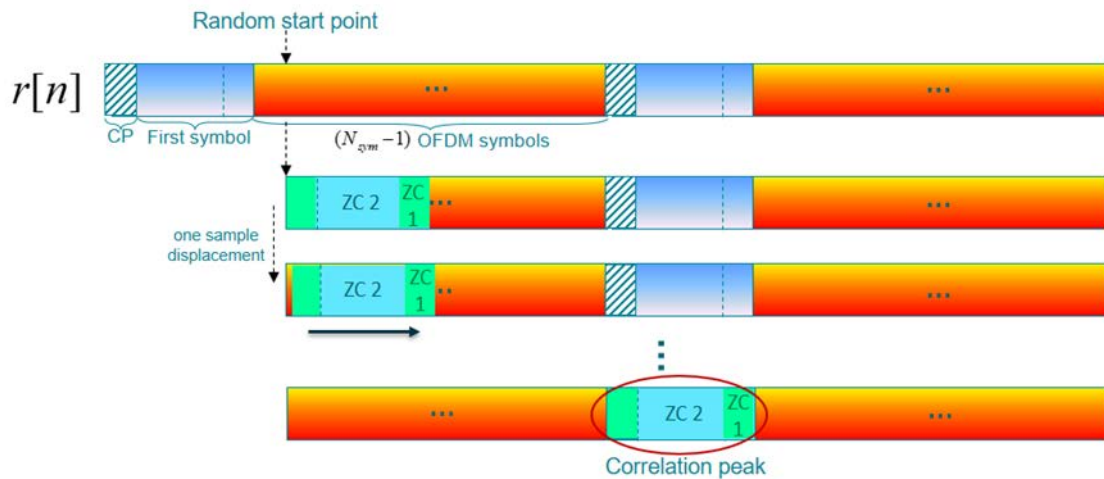


Figure 15: Coarse synchronization algorithm.

The number of iterations that must be performed to guarantee that at least once the correct point of the TTI is processed is $(N_{\text{sym}}N_{\text{OFDM}} + N_{\text{CP}})$.

However, the problem is that in multipath conditions this is not very accurate due to the delayed signals, so there might be sampling error around the correct point. Therefore, fine synchronization is the made with the value returned by the coarse synchronization.

- Fine synchronization:

When the algorithm has an estimation of the start point of the TTI by the coarse synchronization, the fine synchronization starts. For this process, the second sequence of ZC is used. At this stage, the signal is equalized to eliminate the effect of the channel. To do this equalization, an ideal CSI (channel state information) knowledge at the receiver has been assumed. Correlation is computed again, using the second ZC sequence. When the correlation peak is found, the exact point at which

the packet begins can be obtained. In this case, after performing equalization, the starting point is obtained with greater accuracy. Figure 16 illustrates the fine synchronization algorithm.

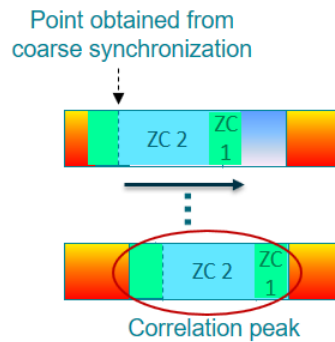


Figure 16: Fine synchronization algorithm.

To find the beginning the beginning of the frame taking into account the margin error of the coarse algorithm, a correlation is made starting at point obtained by the coarse synchronization minus $N_{CP}/2$, comparing our signal with the ZC 2 known by the receiver. This comparison is done N_{CP} iterations and then the perfect synchronization point is obtained when the correlation is maximum.

Simulations were performed to obtain the limits of SNR in which this algorithm is capable to synchronize correctly. Two different propagation models have been used: EPA (extended pedestrian A) and EVA (extended vehicular A) which has different delay profiles. The coarse algorithm is done during 500 TTIs to obtain the most repeated value, which is used by the fine algorithm, which works during 31 TTIs. To yield the correct synchronization this fine synchronization algorithm has to obtain the correct value in more than 50% of the iterations (16 iterations at least). Table 3 shows the SNR limits for an acceptable performance of the proposed TTI structure.

Table 3: Synchronization results for B-OFDM modulation

SNR (dB)	Percentage of success [%]. EPA channel	Percentage of success (%). EVA channel
-10	25.54	10.26
-8	24.36	34.62
-6	98.72	100
-4	98.73	100
-2	98.74	100
0	100	100
2	100	100
4	100	100
6	100	100

3.1.2.4 OFDM throughput comparison

Simulations with different conditions were performed in order to compare the system performance assuming conventional OFDM TTI and the proposed TTI structure. The simulations conditions are depicted in Table 5.

Table 4: Simulation setup for OFDM, B-OFDM throughput comparison.

Parameter	Setting
Carrier frequency	2.6 GHz
System bandwidth	20 MHz
User bandwidth	100 RBs
Modulation and Coding Scheme Index	MCS 0, 5, 10, 15, 20, 25, 28
Cyclic prefix length (samples)	160 (1 st symbol) + 144 (subsequent ones) for LTE; 160 + 0 for the modified scheme
Channel type	ITU EPA channel model, 3 km/h with no shadow fading
Channel estimation	Ideal
MIMO configuration	1x1
Receiver scheme	Maximum Likelihood
No. erroneous blocks	400
Reconstruction of PDCCH	Hard decisions over the received constellation symbols
No. iterations of the turbo decoder	8
HARQ	Not implemented
Interleaver	Rectangular matrix with 12 columns and $\lceil (\text{no. PDSCH bits})/12 \rceil$ rows

Using this simulation conditions, BLER and throughput comparisons have been obtained, which are shown in Figure 17 and Figure 18, respectively. The legend refers with “no CP” to the B-OFDM waveform and by “CP” as the standard OFDM structure.

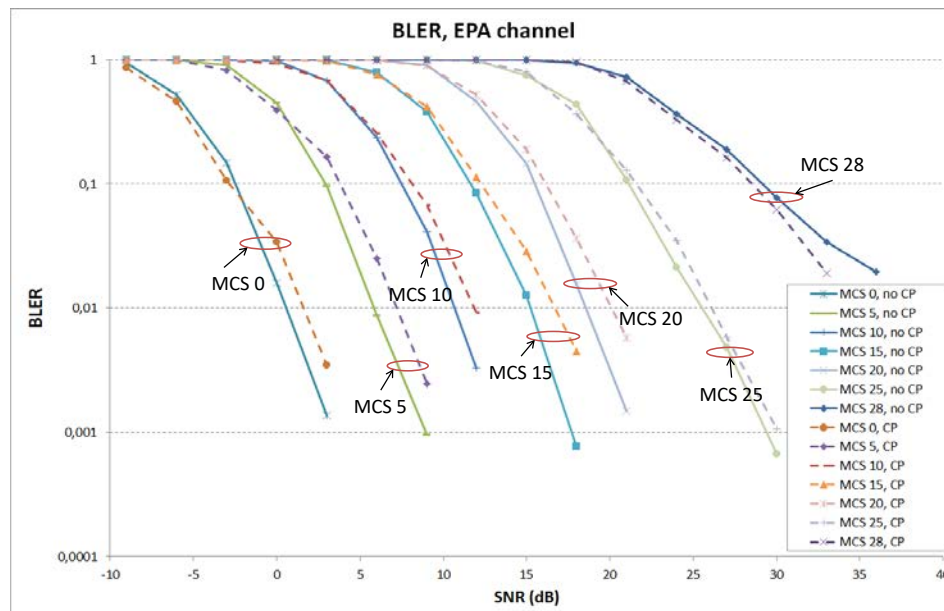


Figure 17: BLER comparison of OFDM and B-OFDM.

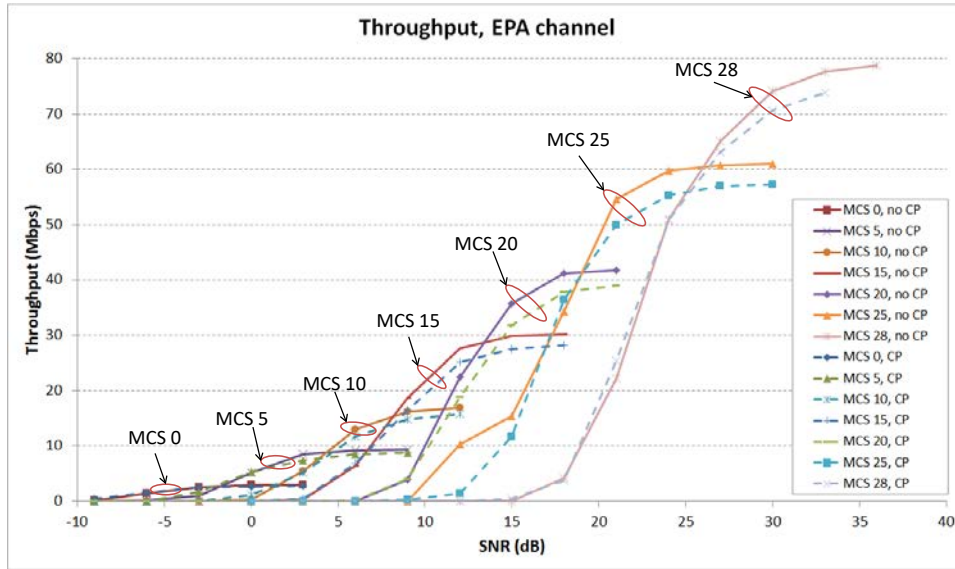


Figure 18: Throughput comparison of OFDM and B-OFDM.

The simulation shows that the proposed TTI structure has an improvement in both of throughput and BLER results due to the higher CP overhead efficiency. BLER has an improvement around 1 dB for a fixed BLER value. Throughput has a higher improvement for the highest MCS values and it is more evident at high SNR, where up to 7% of throughput improvement can be observed.

In conclusion, the reduction of the CP overhead creates an improvement of the systems in terms of throughput and BLER, in exchange for an additional processing at the receiver side, both in the equalization and in the synchronization. The functional requirements defined at the beginning of this section can be accomplished due to the similarity with the standard OFDM structure (Req-F.m.5, Req-F.m.6, Req-F.m.8, Req-F.m.10, Req-F.m.13). For these requirements, the system shall have similar properties as standard OFDM.

3.1.3 F-OFDM

The F-OFDM waveform was briefly presented in D3.1 [2]. This waveform was introduced in [15] as a well frequency localized waveform, derived from OFDM but able to address some of its drawbacks namely: strict requirement on synchronization between UE's, OOB emissions and hence spectral efficiency.

On the downlink of the F-OFDM signal, the band is divided into L sub-bands. The data for each user is processed independently and correspond to the signal to be transmitted in the l -th sub-band. The bits are mapped in a QAM constellation and transmitted in blocks of K_l symbols, with K_l being the number of subcarriers in the l -th sub-band. One IFFT of K_l points is processed for each sub-band. A cyclic prefix of length $N_{CP,l}$ is added. The signal is then filtered linearly convolving the signal the prototype impulse response $g_l[n]$. The signal is then translated to the l -th sub-band and combined to the signals of the other sub-bands for transmission. Figure 19 illustrates the F-OFDM transmitter and receiver chains as a block diagram.

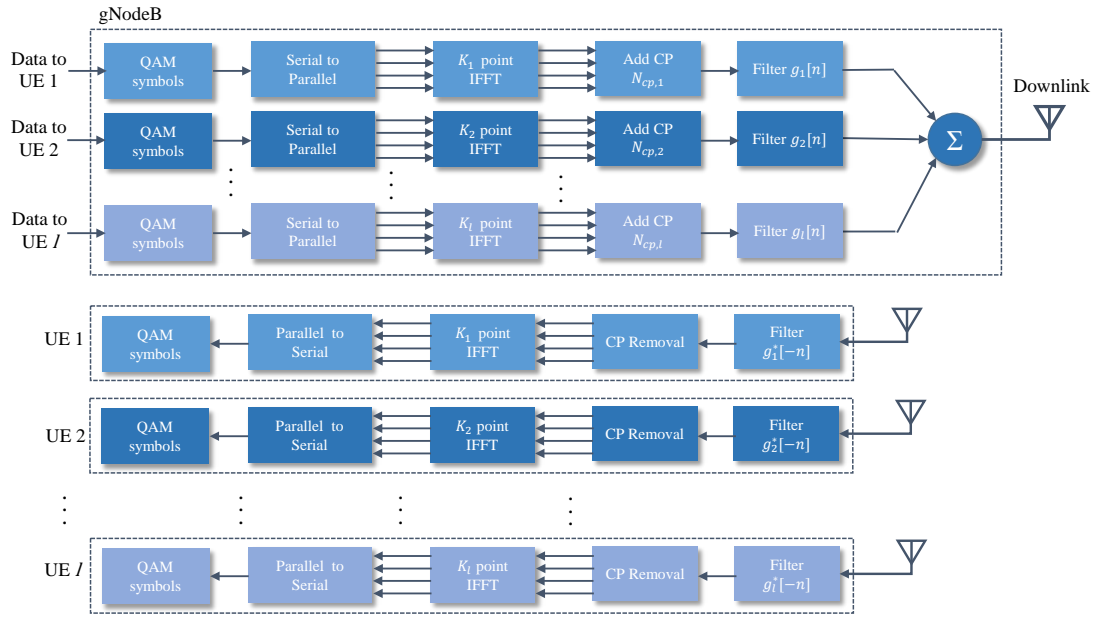


Figure 19: F-OFDM block diagram for the downlink.

The F-OFDM signal for each user is given by

$$\tilde{x}_l[n] = x_l[n] * g_l[n] \quad (7)$$

where $x_l[n]$, is the OFDM signal for the l -th sub-band with $N_{cp,l}$ samples given by

$$x_l[n] = \sum_{k=k'}^{k'+K_l-1} d_{k,l} \cdot e^{(j2\pi \frac{k}{N}n)}, (-N_{cp,l} \leq n < N) \quad (8)$$

where N is the total number of subcarriers in the system and $\{k', k' + 1, \dots, k' + N - 1\}$ are the index of the subcarriers assigned to the l -th sub-band. $d_{k,l}$ is the QAM symbol transmitted at the k -th subcarrier in the l -th sub-band.

At the receiver the signal is filtered by $g_l^*[-n]$, which is the matched version of the transmission filter. This operation rejects emissions from other UE's and maximizes the SNR for the receiver for the UE at the l -th sub-band.

The overall system frequency response at the receiver is $g_l[n] * h[n] * g_l^*[-n]$, is then compensated by the frequency-domain single-tap equalizer as in the OFDM waveform. $h[n]$ is the channel frequency response.

One important aspect of the F-OFDM signal is the design of the $g_l[n]$ filter. This is designed in such way that it is flat inside the l -th sub-band and have a high rejection a few subcarriers away. Such selective filter requires a long impulse response, usually much longer than the CP. The use of a sinc function truncated by a hamming window provides good time localization and, despite its length, most of the energy is contained within the CP and this reducing the inter-symbol interference caused by the linear convolution with the filter [15]. Figure 20 shows the spectrum of the F-OFDM signal with two sub-bands.

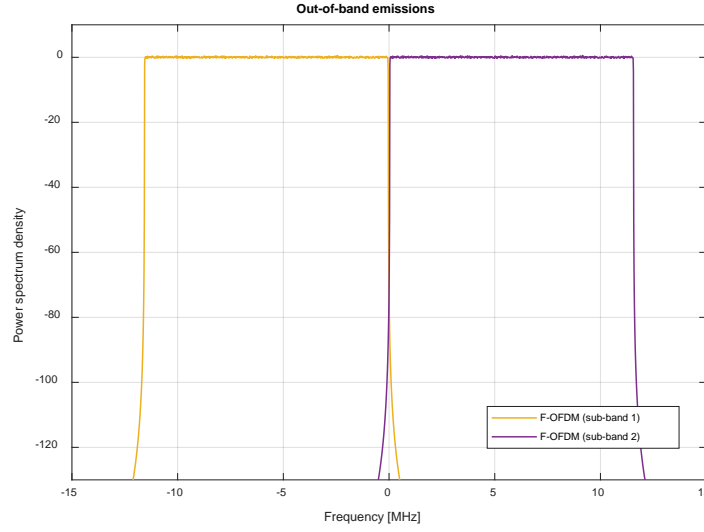


Figure 20: Power spectrum of the F-OFDM signal with two sub-bands.

3.1.4 GFDM Waveform

As introduced in D3.1 [2], GFDM is a non-orthogonal multicarrier waveform where, as opposed to OFDM, every individual subcarrier is pulse-shaped to reduce OOB emissions [16]. In addition to that, the GFDM symbol is composed by M subsymbols that are cyclically time-shifted versions of the pulse shaping filter kernel $g[n]$, weighted by the information data to be carried. Each one of the K subcarriers is a cyclically frequency-shifted version of the transmission pulse.

The GFDM waveform is described in the discrete time by

$$x[n] = \sum_{k=0}^K \sum_{m=0}^M d_{k,m} \cdot g[\langle n - mK \rangle_N] \cdot e^{j2\pi \frac{k}{K}n}, \quad (9)$$

where $x[n]$, is the modulated signal, $g[n]$ is the prototype pulse, $N = MK$, is the total number of samples of the GFDM symbol and $\langle \cdot \rangle_N$ denotes modulo N operation.

The GFDM signal can be viewed as a framework allowing the description and implementation of many recent waveforms, which makes GFDM a suitable technique for the 5G-FlexNOW implementation. Eq. (9) can be described as matrix operations. In this case, the modulated signal vector is given by

$$\mathbf{x} = \mathbf{A}\mathbf{d}, \quad (10)$$

where \mathbf{d} is the $MK \times 1$ data vector and \mathbf{A} is the $N \times N$ transmit matrix composed by the N possible combinations of the K frequency-shifted and the M time-shifted versions of transmitter pulse. The GFDM signal is transmitted through the channel, modeled by a discrete impulse response $h[n]$. The received signal vector is given by

$$\mathbf{y} = \mathbf{H}\mathbf{A}\mathbf{d} + \mathbf{w}, \quad (11)$$

in which \mathbf{H} is the $N \times N$ circulant channel matrix built from the impulse response $h[n]$. It is assumed that $x[n]$ is protected by a CP longer than the channel delay profile. \mathbf{w} is the Additive White Gaussian Noise (AWGN) vector with zero mean and variance σ_w^2 . At the receiver side, the transmitted data is estimated by

$$\hat{\mathbf{d}} = \mathbf{B}\mathbf{y}, \quad (12)$$

where \mathbf{B} is the $N \times N$ receiver matrix. There are three standard linear receiver matrices, namely ZF, MF (matched filter), and MMSE (minimum mean square error). The MF reception matrix is the conjugate transpose of the transmit matrix, leading to

$$\mathbf{B}_{\text{MF}} = \mathbf{A}^H \mathbf{H}^{-1}, \quad (13)$$

where $(\cdot)^H$ denotes the Hermitian operator. The MF receiver results in maximum rejection of AWGN per subcarrier. However, it is not able to remove self-interference when non-orthogonal prototype pulses are employed on the transmitter side. Notice that channel equalization is performed by the term \mathbf{H}^{-1} . The ZF receiver matrix is given by

$$\mathbf{B}_{\text{ZF}} = (\mathbf{H}\mathbf{A})^{-1}, \quad (14)$$

The ZF receiver is able to cancel the self-interference in the case of non-orthogonal pulses, but at the cost of noise enhancement.

In ZF and MF receivers, the effect of the selective channel can be treated before the GFDM detection, i.e., frequency-domain equalization can be used before demodulation instead of inverting the channel matrix. In contrast, the MMSE receiver jointly performs channel equalization and GFDM decoding, minimizing the mean square error between the transmitted and the estimated data symbols. The receiver matrix for this case is given by

$$\mathbf{B}_{\text{MMSE}} = [(\mathbf{H}\mathbf{A})^H(\mathbf{H}\mathbf{A}) + \sigma_w^2 \mathbf{I}]^{-1}(\mathbf{H}\mathbf{A})^H. \quad (125)$$

3.1.5 Waveform Comparisons

This section provides a comparison of all previously introduced candidate waveforms with respect to OOB emissions, CP-overhead efficiency, implementation complexity and SER performance, before choosing the most promising candidate for the application in the 5G-RANGE PHY.

3.1.5.1 Out-of-band emissions

The 5G-RANGE PHY must allow dynamic spectrum (Req-F.m.5) usage in the TVWS spectrum. The non-continuous spectrum allocation (Req-F.m.6) on unlicensed spectrum demands a robust waveform, able to meet the requirement out-of-band emission limits (Req-Q.m.11) without the use of RF filters (Req-F.m.14) [1].

In order to cope with these requirements, the waveform for the 5G-RANGE PHY must exhibit low OOB emissions. A numerical simulation was performed to compare the waveforms. Table 5 shows the parameters used for each waveform in the simulations. The resulting power spectrum is depicted in Figure 21.

Table 5: Parameters used in the simulation of the waveforms for power spectrum comparison.

	OFDM	B-OFDM	F-OFDM	GFDM
Subcarriers (K)	16384	16384	16384	16384
subsymbols (M)	1	4	1	4
Prototype pulse	Sinc	Sinc	Sinc	Raised Cosine
Roll-off factor (α)	NA	NA	NA	0
Filter Length (L)	NA	NA	8193	65536
Filter Type	NA	NA	Windowed-sinc	NA

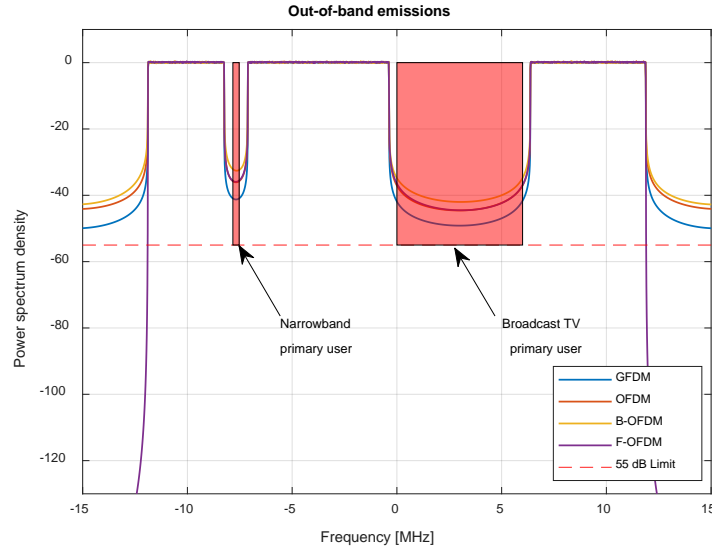


Figure 21: Comparison between the power spectrum of the GFDM, OFDM, B-OFDM and F-OFDM waveforms.

Figure 21 simulates the spectrum occupied by the waveforms when part of the bandwidth is reserved to a narrowband and a wideband primary user, denoted by the red parts in the figure. It is possible to verify that F-OFDM has the lower OOB emission, but its performance in terms of in-band emission is not the same. In the reserved bands of the spectrum, F-OFDM performs close to OFDM. The OFDM and B-OFDM performance is poor due to the abrupt transitions between symbols. GFDM has a slightly better performance when compared with OFDM, but it still does not match the OOB emissions requirement. In fact, with the assumed configuration, none of the waveforms is able to meet the OOB emissions requirement of -55 dBc ACLR. (Req.-Q.m.11).

To overcome this, a windowing operation is applied to the waveforms, creating a smooth transition between the symbols. The window operation consists on multiplying the waveform samples by a window. A raised cosine window is used. This window is given by

$$w_N[n] = \begin{cases} 0.5 \cdot \left[1 + \cos\left(\pi + \frac{n\pi}{N_w}\right) \right], & (n < N_w) \\ 1, & (N_w \leq n < N - N_w) \\ 0.5 \cdot \left[1 + \cos\left(\frac{(n - N - N_w)\pi}{N_w}\right) \right], & (n \geq N - N_w), \end{cases} \quad (16)$$

where N is the symbol length in samples and N_w is the number of samples in the transition region. The spectrum of the waveforms with windowing is depicted in Figure 18. Is important to notice that the $2N_w$ samples affected by the windowing operation must belong to the symbol's cyclic extensions, and not to the symbol itself. Hence, it is necessary to add a CS (cyclic suffix) to the symbol.

In Figure 22 is possible to notice that OFDM, GFDM and F-OFDM waveforms were able to fulfil the OOB emission requirement. Despite the windowing operation, B-OFDM still exhibits poor OOB emissions. This is due to the fact that the symbol of this waveform is composed by several OFDM subsymbols and the transition between all of them generates OOB emissions, while the window can be applied only at the beginning and end of the entire symbol. Because B-OFDM does not fulfil Req.-Q.m.11, it is discarded as a possible candidate waveform.

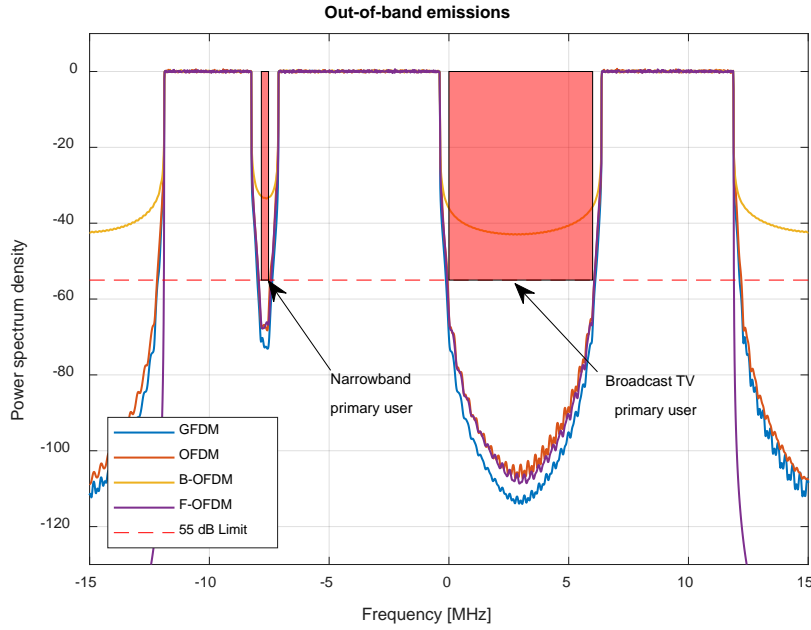


Figure 22: Comparison between the power spectrum of the GFD, OFDM, B-OFDM and F-OFDM waveforms with windowing.

3.1.5.2 Overhead Efficiency

Despite useful in many aspects, the cyclic extensions, namely CP and CS, added to the waveform symbols adds overhead to the data transmission and reduces the useful data rate achievable with those waveforms. The requirement for robustness against severe multi-path propagation environment and high spectral efficiency are contradictory, in the sense that a long CP is required to achieve the first, but at the same time it reduces the spectral efficiency.

The efficiency of the waveforms regarding the cyclic extensions can be calculated by

$$\eta = \frac{N}{N + N_{CP} + N_{CS}}, \quad (17)$$

where, N_{CP} , N_{CP} and N_{CP} are the number of samples in the symbol, number of samples in the CP and in the CS, respectively. The efficiency of the waveforms regarding the cyclic extensions is presented in Table 6. This comparison considers the same level of protection against multi-path propagation for all waveforms, hence, the same number of subcarriers and CP duration. The duration of the symbol for B-OFDM and GFD waveforms is $N = MK$, where K and M are the numbers of subcarriers and subsymbols, respectively.

Table 6: Cyclic extension efficiency of the waveforms OFDM, B-OFDM, F-OFDM and GFD.

Waveform	K	M	N	N_{CP}	N_{CS}	η
OFDM	16384	1	16384	4352	768	76,19%
B-OFDM	16384	4	65536	4352	768	92.75%
F-OFDM	16384	1	16384	4352	768	76,19%
GFD	16384	4	65536	4352	768	92.75%

The GFDM and B-OFDM can offer a better efficiency due to the fact that the cyclic extensions are applied to multiple subsymbols resulting in less overhead.

3.1.5.3 Implementation Complexity

Modern wireless communication devices use DSP (digital signal processing) to perform the operations related to the transmission and reception of the radio signals. These procedures can be performed by application-specific hardware, as is the case for ASICs (application specific integrated circuits), generic hardware like FPGAs (field-programmable gate arrays) or by software in SDR (software defined radio) architectures. In any of the previous cases, the number of mathematical operations required to transmit or receive signals has a direct impact on cost, silicon area, and energy consumption of the wireless devices.

Two metrics are usually considered when assessing complexity of signal processing algorithms, the number of CMs (complex multiplications), and the big-O complexity, which describes how the number of complex operations scales as the input parameters grow asymptotically.

The implementation of the OFDM waveform is accomplished efficiently by the use of the FFT (fast Fourier transform). Assuming the Cooley-Tukey [17] algorithm, the OFDM modulation and demodulation processes can be computed using one IFFT (inverse fast Fourier transform) at the transmitter and one FFT at the receiver, resulting in $K \log_2 K$ CMs. The single tap equalization process in the OFDM waveforms adds $2K$ multiplications, which results in an overall complexity of $K(\log_2 K + 2)$. The big-O complexity for the OFDM modulation and demodulation processes is then $\mathcal{O}(K \cdot \log_2 K)$.

As the B-OFDM signal is formed by M OFDM subsymbols, the B-OFDM symbol can be formed repeating the OFDM M times, leading to the total of $MK \cdot \log_2 K$ CMs, including the demodulator processing. The equalization of the B-OFDM waveform is processed for the entire block of MK samples the signal needs to be transformed to the frequency domain with equalized and transformed back to time domain for the demodulation process. The equalization process adds $MK(\log_2(MK) + 2)$ CMs resulting in an overall complexity of $MK(\log_2 K + \log_2(MK) + 2)$. Note that if $M \rightarrow 1$, the big-O complexity of B-OFDM also approaches $\mathcal{O}(K \cdot \log_2 K)$.

The F-OFDM signal is obtained by filtering the signal after the IFFT modulation process. At the receiver the signal is matched filtered and then demodulated using a FFT. The filtering operation is a linear convolution and considering the length of the filter impulse response $K/2$ [15], its complexity is of the order of $(K/2)^2$. The filtering operation can also be implemented with FFT using the overlap-and-save method which reduces the complexity of each filtering operation to $K(\log_2 K + 1)$. The equalization process also adds $2K$ CMs and the overall complexity for the F-OFDM modulator and demodulator process is then $K(3\log_2 K + 4)$ CMs. The big-O complexity for F-OFDM is also $\mathcal{O}(K \cdot \log_2 K)$.

Until now, the implementation of a GFDM modem was considered to be very complex, because either the number of subcarriers K or the number of subsymbols M has to be odd⁶ [18]. As a result, the DFT (discrete Fourier transform) in at least one of the parameters K/M cannot be implemented efficiently as a FFT. However, recent advances in filter design have shown how to overcome the constraint and allow for even parameters [19]. Following this principle, a TD (time domain) real-time implementation with an even number of subcarriers is presented in [20], and a FD (frequency domain) implementation with an even number of subsymbols is shown in [21]. However, recent advances in filter design have shown how to overcome this constraint and allow for even parameters [19]. Besides, the flexibility of this new architecture allows for an implementation of different well-known waveforms, without being restricted to GFDM. As a result, a more efficient and flexible implementation using a GFDM modem is now possible.

⁶ Otherwise, the modulation matrix \mathbf{A} becomes singular.

The radix-2-based modem for time and frequency domain GFDM described in [22] will be used as a reference. This modem replaces the conventional core from previous designs with an FFT block, enabling radix-2 processing. With the proposed architecture, modulator as well as demodulator can be configured independently to work either in time domain or in frequency domain. Therefore, the final configuration of the modem can be chosen from one of the four different available combinations, namely TD-TD, TD-FD, FD-TD and FD-FD, making it possible to address different needs. Table 7 contains the number of CMs needed for different modem configurations. At the receiver, usually a FD channel equalizer is preferred, because of available low-complexity implementations. This evaluation considers the three possible implementations (TD-TD, TD-FD and FD-FD), distinguishing between the conventional and the FFT-based design. For simplicity, only TD-FD is included, an FD-TD implementation would result in a similar complexity. To illustrate the performance improvement, Figure 23 compares the number of CMs, which account for the highest computational complexity of the two most common implementation schemes, namely FFT-based TD-FD and conventional TD-FD. It can be observed that the new design beats the conventional by more than two orders of magnitude for large systems. A thorough description of the complexity in terms of number of CMs, and a hardware analysis considering flexibility, resource consumption and latency can be found in [22]. Nevertheless, it is important to notice that the GFDM modulation and demodulation processes can also be implemented with big-O complexity of $\mathcal{O}(MK \cdot \log_2 MK)$.

Table 7: Number of CMs of the modem

Implementation	Number of CMs
FFT-based, TD-FD	$2N \log_2(N) + 2N$
FFT-based, TD-TD	$2N \log_2(N) + N \log_2(M) + 2N$
FFT-based, FD-FD	$2N \log_2(N) + N \log_2(K) + 2N$
conventional, TD-FD	$N \log_2(N) + (K + M)N$
conventional, TD-TD	$N \log_2(N) + N \log_2(K) + 2MN$
conventional, FD-FD	$N \log_2(N) + N \log_2(M) + 2KN$

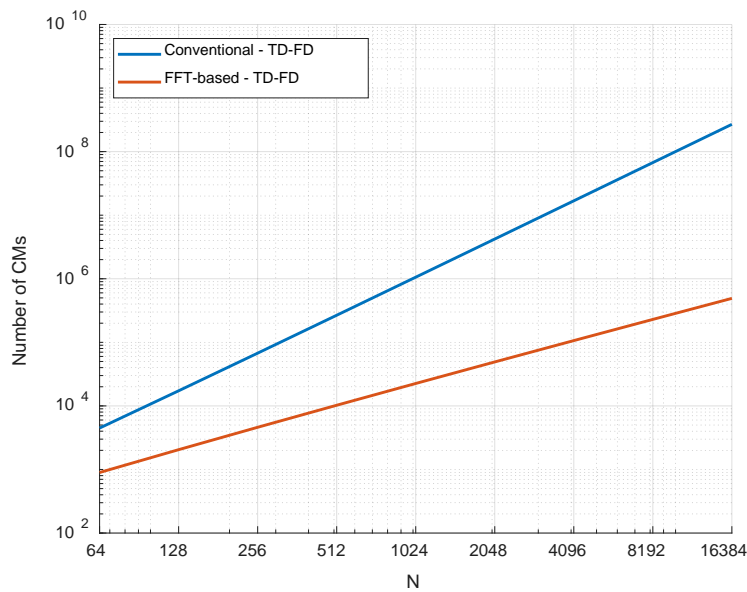


Figure 23: Comparison in number of CMs for conventional and FFT-based implementation.

Table 8 summarizes the implementation complexity for each waveform. For this comparison, the computational effort to transmit and receive the same amount of data in each waveform is assumed. Hence, for OFDM and F-OFDM the complexity in CMs is calculated for M symbols in order to achieve a fair comparison.

Table 8: Comparison of the complexity of the waveforms for $K=16384$ and $M=4$.

Waveform	Number of CMs	CMs ($K=16384$, $M=4$)
OFDM	$MK(\log_2 K + 2)$	1.05×10^6
B-OFDM	$MK(\log_2 K + \log_2(MK) + 2)$	2.10×10^6
F-OFDM	$MK(3\log_2 K + 4)$	3.01×10^6
GFDM	$2MK(\log_2(MK) + 2)$	2.36×10^6

From Table 8, it can be noticed that, as expected, OFDM have the less complex implementation, followed by the B-OFDM and GFDM waveforms. The F-OFDM waveform is the most complex implementation due to the need of the long filters at transmitter and receiver sides, even when considering fast convolution algorithms based on FFT. However, the implementation complexity of any waveform is affordable for current signal processing processors and FPGAs.

3.1.5.4 SER Performance

This section provides a numerical SER performance comparison of the different waveform over the 5G-RANGE channel model, in order to evaluate the suitability of the different waveforms for the application in 5G-FlexNOW. The SER performance has direct impact on the BLER performance and hence on the total system performance. Even small differences in SER can lead to significantly different BLER performance. Figure 24 presents the waveforms SER performance over AWGN channel, while Figure 25 shows the SER performance over 5G-RANGE channel models, assuming LOS and NLOS. Furthermore, Table 9 presents the parameters used during for the SER simulations for the waveforms.

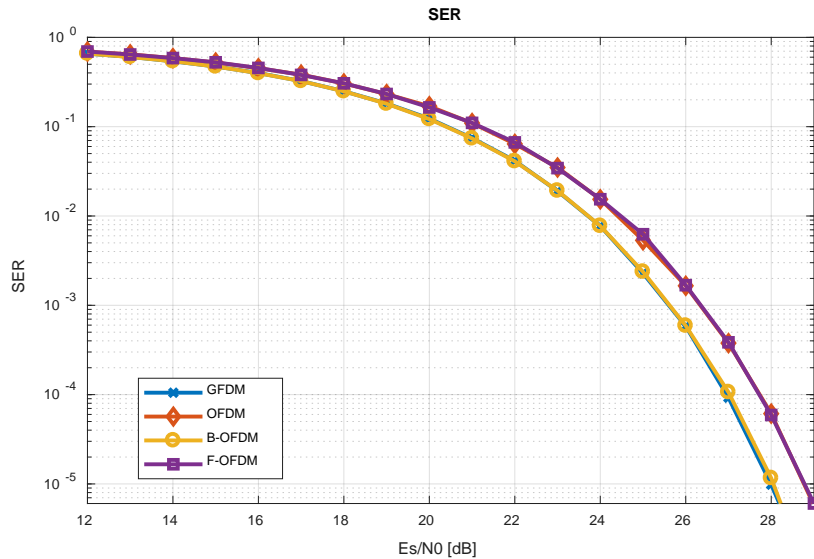


Figure 24: SER performance of the waveforms under AWGN channel.

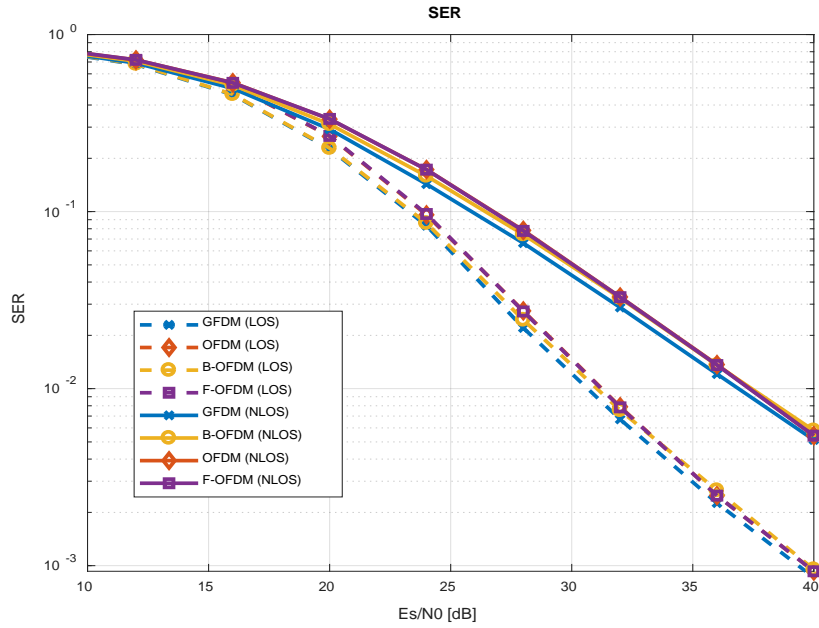


Figure 25: SER performance of the waveforms under 5G-RANGE LOS and NLOS channel models.

Table 9: Parameters of the waveforms for the SER comparison.

	OFDM	B-OFDM	F-OFDM	GFDM
Subcarriers (K)	16384	16384	16384	16384
Subsymbols (M)	1	4	1	4
Cyclic-prefix (CP)	4352	4352	4352	4352
Cyclic-suffix (CS)	768	768	768	768
Modulation order	64-QAM	64-QAM	64-QAM	64-QAM
Prototype pulse	sinc	sinc	sinc	raised cosine
Roll-off factor (α)	NA	NA	NA	0
Demodulator type	ZF	ZF	ZF	ZF

From the AWGN and LOS/NLOS simulation results, it is possible to notice that the SER performance of the GFDM and B-OFDM waveforms is practically the same. The OFDM and F-OFDM waveforms have worse performance due to the lower CP/CS efficiency. In order to compare the waveforms with the same spectral efficiency, the CP/CS efficiency must be compensated using

$$C = 10 \cdot \log_{10}(\eta).$$

The GFDM presents a slight performance gain over 5G-RANGE NLOS channel when compared with the other waveforms. This performance gain can be explained by the higher diversity gathered by GFDM.

3.1.5.5 Waveform selection

The GFDM, OFDM and F-OFDM waveforms are able to fulfil the 5G-RANGE specification, regarding OOB emissions. The B-OFDM cannot meet the -55 dB ACPR specification and cannot be further considered for the 5G-RANGE PHY.

On the simulated conditions, GFDM, OFDM and F-OFDM waveforms offer the same level of OOB emissions, with GFDM presenting a slightly better SER performance when compared with the other two candidates. Considering the 5G-RANGE application scenario, F-OFDM does not add any benefit over OFDM, which has smaller implementation complexity. Therefore, two waveforms will be considered as part of the 5G-RANGE PHY: i) GFDM, because of its low OOB emissions, high spectrum efficiency and flexibility and; ii) OFDM because of its low complexity and possible compatibility with other 5G scenarios. It is important to notice that this definition doesn't mean that two sets of modulator/demodulators need to be implemented, since GFDM covers OFDM as corner case.

3.2 Flexible frame structure

The 5G-RANGE frame structure proposal aims to address the various propagation channels imposed by the remote area applications and, therefore, fulfil the use-case and requirements for long range and TVWS operation. Some of the requirements implies conflicting PHY parameters, requiring a flexible frame structure where different numerologies can be employed.

The 5G-RANGE frame adopts the same principle of scalable numerology present in 5G NR, where SCS (subcarrier spacing) in every sub-frame, to attend specific users and use cases.

Another important function of the frame structure is to define the position for specific signals, such as, reference signals used for synchronization and channel estimation required for the correct operation of the PHY. This section will describe the main aspects of the frame structure and it will also present the definitions made, up to this point in the project, regarding the frame structure for the 5G-RANGE PHY for FDD (frequency division duplexing) operation in TVWS spectrum.

3.2.1 Frame structure

The 5G-RANGE transmissions are organized in periods so called radio frames. After the transmission of one radio frame the organization of the data transmitted over the air repeats on the next frame and so on. An integer number of sub-frames with the same duration composes the radio frame. The number of symbols in the sub-frame is dependent on the numerology.

3.2.1.1 Time domain structure and flexibility

Due to conflicting requirements, such as mobility and resilience to severe multipath, a single numerology cannot offer an efficient compromise solution. The 5G-RANGE frame must, therefore, support multiple numerologies coexisting in the air interface to serve different users and use-cases. The same approach used in 5G NR is adopted, where the frame supports a scalable numerology. In this case, the symbol and CP duration are scaled inversely to the SCS, in such way that an integer number of symbols, for any numerology, align at the sub-frame duration boundaries. Figure 26, depicts the frame structure in time domain highlighting this alignment.

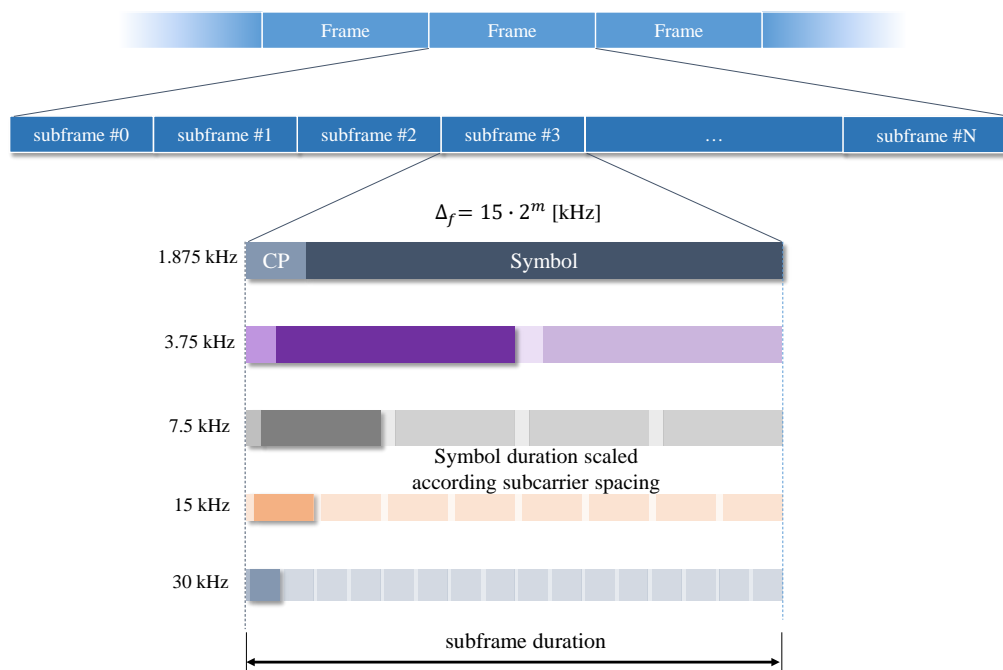


Figure 26: Frame structure in time domain showing the alignment of multiple numerologies.

Table 10 shows the frame and sub-frame duration for the different numerologies supported in 5G-RANGE. The rationale for the choice of those numbers is presented in Section 3.2.1.3.

Table 10: 5G-RANGE symbol duration in different numerologies for GFDM waveforms.

Numerology ID	SCS [kHz]	CP [μs]	CS [μs]	Symbol [μs]	Subframe [μs]	Symbols per subframe
0	1.875	141.7	25	2133.33	4600	2
1	3.75	70.8	12.5	1066.67	4600	4
2	7.5	35.4	6.25	533.33	4600	8
3	15	17.7	3.13	266.67	4600	16
4	30	8.9	1.57	133.33	4600	32
5	30	4.4	0.78	66.67	4600	64

The 5G-RANGE sub-frame duration depends on the selected waveform. Using the OFDM waveform, where each symbol is protected by one CP or using the GFDM waveform, where many symbols or sub-symbols are protected by a single CP, leads to different sub-frame durations.

3.2.1.2 Resource grid and fragmented spectrum usage

The 5G-RANGE PHY uses multicarrier waveforms with transmissions arranged in symbols, in time domain, and carried by subcarriers, in frequency domain. This structure forms a time-frequency grid where the information is organized and transmitted in a similar manner than in 5G NR.

The fragmented spectrum usage, required for TVWS operation (Req-F.m.6), is achieved by selecting the groups of subcarriers to transmit, avoiding the positions on the spectrum where the primary users are located. This approach allows fine granularity in spectrum usage and allows for avoiding narrowband incumbents in efficient manner. Figure 27 depicts the frequency-time resource grid.

The 5G-RANGE PHY allows allocation with the granularity of one RB (resource block), which is composed by a fixed bandwidth of 180 kHz in frequency domain. This RB is equivalent to 12 subcarriers with 15 kHz SCS, therefore, the same as LTE or the 5G NR. However, as opposed to 5G NR, RBs are not scaled with the SCS and hence, remain constant for any numerology. In the time domain, the 5G-RANGE RBs have a duration of one sub-frame.

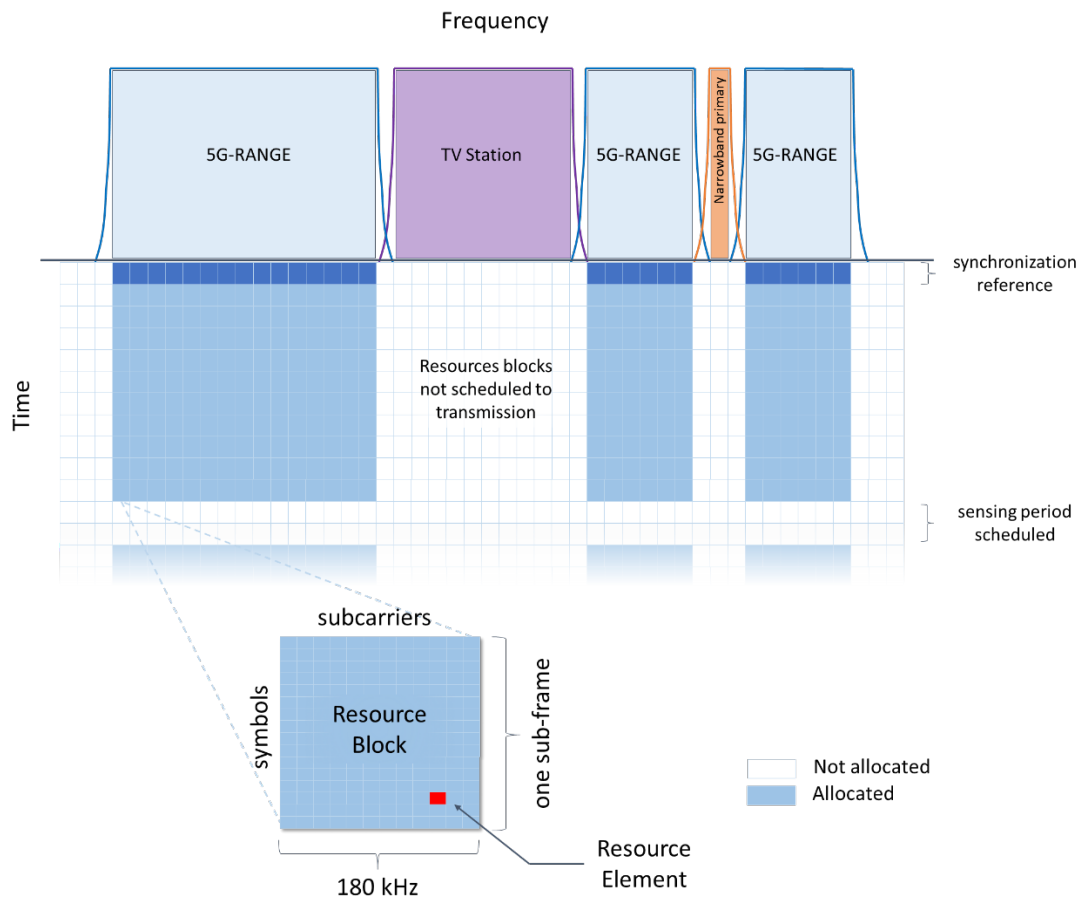


Figure 27: 5G-RANGE resource grid and fragmented spectrum usage.

The amount of RE (resource elements) carried in a RB for the various waveforms are shown in Table 11. In this table, it is also possible to verify the gross bit rate for one RB, assuming mapping ranging from QPSK up to 256QAM.

Table 11: Gross bitrate per RB for GFDM waveform.

ID	SCS [kHz]	Number of subcarriers	Number of subsymbols	RE's	Bitrate per RB (kbps)			
					QPSK	16 QAM	64 QAM	256 QAM
0	1.875	96	16	672	292.17	584.35	876.52	1314.78
1	3.75	48	16	720	313.04	626.09	939.13	1408.70
2	7.5	24	32	720	313.04	626.09	939.13	1408.70
3	15	12	64	720	313.04	626.09	939.13	1408.70
4	30	6	128	720	313.04	626.09	939.13	1408.70
5	30	6	256	736	320.00	640.0	960.00	1440.00

Table 12 shows the gross bit rate at the PHY layer considering 24MHz downlink bandwidth of TVWS spectrum, which is equivalent to 132 RB's.

Table 12: Gross PHY bitrate for 24MHz of TVWS spectrum.

Numerology ID	Gross bitrate for 24 MHz [Mbps]			
	QPSK	16 QAM	64 QAM	256 QAM
0	38.57	77.13	115.70	154.27
1	41.32	82.64	123.97	165.29
2	41.32	82.64	123.97	165.29
3	41.32	82.64	123.97	165.29
4	41.32	82.64	123.97	165.29
5	42.24	84.48	126.72	168.96

We propose one slice of time in the radio frame dedicated for in-band spectrum sensing. During this period no transmission are allowed from the gNB (next generation NodeB) or from the UE. Therefore it is possible for the receivers to sense the spectrum within the bandwidth of its RF front-end. In the downlink direction, the UE senses its receiving spectrum, while in the uplink the gNB performs the sensing.

The samples collected during the sensing period will be processed by to decide by the occupation or vacancy of the spectrum and this decision is provided to the cognitive MAC, allowing not only the detection of primary users, but also the presence of unauthorized transmissions, avoiding interference. The duration and periodicity of this procedure will be defined in WP 4. Once done, the frame structure will be adjusted accordingly.

3.2.1.3 Use cases and numerology

5G Range PHY must be robust against severe multipath environments and high Doppler shift (Req-F.m.8) [1]. On multi-carrier waveforms, four parameters of the PHY design are crucial for achieving this goal:

- Multicarrier modulations using frequency-domain single tap equalizer assumes that every subcarrier has a flat frequency response. For this assumption be true, the subcarrier bandwidth must be narrower than the channel coherence bandwidth [23].
- To avoid ISI, the cyclic prefix duration must be longer than the maximum channel impulse response duration [24].
- In the case of frequency-domain channel estimation, the pilot carrier spacing should be smaller than the channel coherence bandwidth [24].
- In the case of preamble channel estimation, the preamble should be longer than the channel impulse response [25].
- The channel is assumed to be constant during the symbol duration, therefore, the symbol time must be shorter than the channel coherence time [23].

The channel model is then used to specify the required parameters for the PHY. The 90% coherence bandwidth is given by [26]

$$B_c = \frac{1}{50\sigma_\tau}, \quad (18)$$

where σ_τ is the channel RMS delay spread. Applying (18) to the 5G-RANGE channel models [27] we obtain the 90% coherence bandwidth and it is presented in Table 13. From the table it is possible to see that the subcarrier bandwidth on the long-range channel must be smaller than 40 kHz.

Table 13: 5G RANGE channel model parameters.

Channel Model	Delay spread RMS (σ_τ)	Impulse response duration (τ_m)	Coherence Bandwidth (B_c)
General (CDL-A)	100 ns	966 ns	200 kHz
General (CDL-D)	100 ns	1253 ns	200 kHz
D2D (CDL-A)	500 ns	4893 ns	40 kHz
D2D (CDL-D)	500 ns	6263 ns	40 kHz

Furthermore, to avoid inter-symbol interference, the CP must be longer than the impulse response duration of the channel. In [28], the authors suggest that CP length must be 18% of the electromagnetic wave propagation time from the BS to the edge of the cell, leading to

$$T_{CP} \geq 0.18 \cdot R/c, \quad (19)$$

where, R is the cell radius and c is the speed of light. The 5G-RANGE specific requirements for “Agribusiness and smart farming”, “Connectivity” and “Remote Health Care” use cases require coverage of up to 100 km, leading to a cyclic prefix duration longer than 60 μ s.

It is reasonable to use this long symbol duration when mobility requirements are relaxed, as it is the case for “Wireless Backhaul connectivity” or “Remote Health care (Multimedia)”. For use cases requiring higher mobility, the long symbol can degrade the performance when the symbol duration is comparable to the channel coherence time. Considering the time-variant channel with Jake’s spectrum, the 50% channel coherence time, $T_{C(50)}$, is given by [29]

$$T_{C(50)} = \frac{9}{16\pi \cdot f_D}, \quad (20)$$

where, f_D , is the maximum Doppler frequency shift, given by

$$f_D = \frac{v}{c} \cdot f_0, \quad (21)$$

in which f_0 and v are the carrier frequency and mobile speed, respectively. Table 14 shows the mobile speed and the coherence time for the use cases defined for 5G-RANGE [1].

The correlation of the channel impulse response taken between two arbitrary time intervals distant in time by Δ_t [30] can be evaluated by

$$R(\Delta_t) = J_0\left(2\pi \frac{f_D}{\lambda} \Delta_t\right), \quad (22)$$

where $J_0(\cdot)$ is the zero order Bessel function of the first kind, and λ is the wavelength of the carrier frequency.

Table 14: Doppler shift and coherence time for the 5G-RANGE use cases.

Use Case	Specific requirement on mobility [km/h]	Maximum Doppler at 800 MHz [Hz]	Coherence Time (50%) [ms]	Coherence Time (99%) [μs]
Agribusiness and smart farming	60	44.5	4	268
Connectivity	60	44.5	4	268
Wireless backhaul (Backhaul)	static	0	-	-
Wireless backhaul (Small Cell)	30	22.2	8	537
Remote Health Care (Monitoring)	120	88.9	2	134
Remote Health Care (Multimedia)	static	0	-	-

From Table 14, is possible to verify that using a long symbol, which is desired from a bandwidth efficiency perspective, cannot meet the mobility required for all use cases. Hence, it is interesting to allow different numerologies to coexist within the frame, each one supporting different users, as proposed in this section.

Using the scalable numerology approach, it is possible to trade between multipath robustness and Doppler resilience by choosing the most appropriate numerology for a given situation or user. This process will be executed dynamically, in parallel with the link adaptation, by the Cognitive MAC. Table 15 shows the numerology proposed for the 5G RANGE PHY. This table also shows the maximum theoretical range and accepted UE speeds associated with the possible numerologies.

Table 15: 5G-RANGE PHY numerologies and associated supported cell range and maximum mobile speed.

Numerology ID	SCS [kHz]	CP [μs]	Symbol [μs]	Number of subsymbols	Number of subcarriers	Target Range [km]	Target Speed [km/h]
0	1.875	141.7	2133.3	4	16384	236,11	7
1	3.75	70.8	1066.7	4	8192	118,06	15
2	7.5	35.4	533.3	4	4096	59,03	30
3	15	17.7	266.7	4	2048	29,51	60
4	30	8.9	133.7	4	1024	14,76	120
5	30	4.4	66.7	2	1024	7,38	240

3.2.2 Pilot signals

The frame structure is also responsible for defining the position for reference signals needed for synchronization and evaluation of the CSI (channel state information). This section describes the 5G-RANGE control signaling in details.

3.2.2.1 Synchronization signals

As specified before, the reference signals in 5G-RANGE will follow largely the specifications defined for 5G NR. However, the main challenge in 5G-RANGE regarding synchronization compared to 5G NR is that, for the initial synchronization, it has to consider that only specific areas of the spectrum (or more specifically of the frame structure, cf. to Section 3.2.1) will be available for the extraction of the required information for synchronization. Therefore, a dedicated channel located in the licensed band will serve for initial access, providing essential information such as the carrier frequency and the frequency band available in the TVWS spectrum, information about the position of the reference signals and system parameters. Once the UE has obtained this initial information, the specific synchronization procedure can be adopted from 5G-NR, based on the detection of the SSB (synchronization signal block).

Each SSB consists of one-symbol PSS (primary synchronization signal), one-symbol SSS (secondary synchronization signal) and a PBCH (primary broadcast channel). The PBCH is divided into a DMRS (demodulation reference signal) and data known as MIB (master information block).

A detailed description about the reference synchronization signals PSS and SSS, as well as the PBCH DMRS in 5G-NR, their generation and mapping in the SSB can be found in [31]. The PSS is located at the beginning of every 5G-RANGE frame and it is the reference for acquiring symbol timing and carrier frequency synchronization.

3.2.2.2 Channel estimation signals

The reference signal used to obtain channel state information are defined on the frame structure. On every subframe, pilot subcarriers are inserted and its specific location depends on the numerology in use. The time and frequency spacing between pilots must respect the 2D sampling theorem and depends on the channel statistics.

Figure 28, shows the position of the reference signals for the 5G-RANGE system with one, two and four transmitting antennas. In detail, the spacing between the reference signals in the resource grid for each numerology is provided in Table 16.

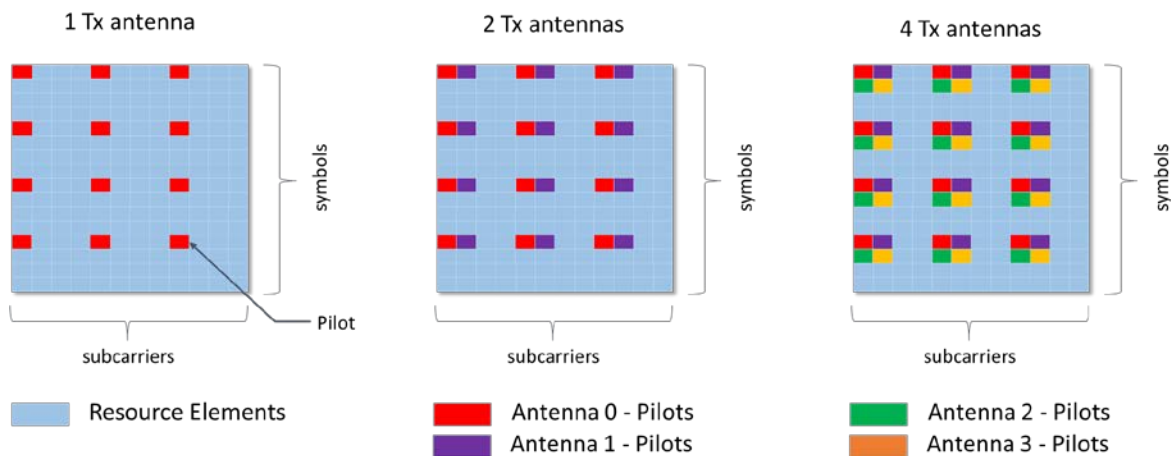


Figure 28: Position of channel estimation reference signals on the time-frequency grid.

Table 16: Spacing between channel estimation pilots for 5G-RANGE numerologies.

Numerology ID	Spacing in frequency (subcarriers)	Spacing in frequency (kHz)	Spacing in time (symbols)	Spacing in time (μs)
0	4	7.5	2	4600,0
1	4	15.0	4	4600,0
2	4	30.0	4	2300,0
3	4	60.0	4	1150,0
4	4	120.0	4	575,0
5	6	180.0	4	287,5

3.3 Definition and specification of 5G-FlexNOW

The specification of 5G-FlexNOW is provided in Table 17.

Table 17: 5G-FlexNOW specification for the 5G-RANGE PHY.

5G-FlexNOW						
	Waveform numerology					
ID	0	1	2	3	4	5
Sample rate (MHz)	30.72					
Waveform	GFDM (OFDM as special configuration)					
Prototype pulse	Raised cosine					
Roll-off factor	0					
Window type	Raised cosine					
Subcarrier Spacing (kHz)	1.875	3.75	7.5	15	30	30
Number of subcarriers	16384	8192	4096	2048	1024	1024
Number of active subcarriers (23.76 MHz bandwidth)	12672	6336	3168	1584	792	792
Number of subsymbols	4	4	4	4	4	2
CP Duration (us)	141.7	70.8	35.4	17.7	8.9	4.4
CS duration (us)	25	12.5	6.25	3.13	1.56	0.78
Symbol duration (us)	2133.3	1066.7	533.3	266.7	133.7	66.7
Extended Symbol (us)	2300	1150	575	287	147.75	71.9
Cyclic extension efficiency	92.75%	92.75%	92.75%	92.75%	92.75%	92.75%
Modulation	QPSK to	QPSK to	QPSK to	QPSK to	QPSK to	QPSK to

	256 QAM	256 QAM	256 QAM	256 QAM	256 QAM	256 QAM
CP Protection Range (km)	230	120	60	30	14	7
Target mobile speed (km/h)	7	15	30	60	120	240
Pilot spacing (subcarriers)	4	4	4	4	4	8
Pilot spacing (symbols)	2	4	4	4	4	4
Uncoded gross bit rate (excluding pilots) 23.76 MHz (132RB)						
QPSK	38.57	41.32	41.32	41.32	41.32	42.24
16-QAM	77.13	82.64	82.64	82.64	82.64	84.48
64-QAM	115.70	123.97	123.97	123.97	123.97	126.72
256-QAM	154.27	165.29	165.29	165.29	165.29	168.96

3.4 Discussions and future perspectives

In this section, we compared the waveforms performance considering the 5G-RANGE channel model and selected GFDM as the waveform for the 5G-FlexNOW block. The selection of this waveform fulfills the OOB emissions requirement (Req-F.m.14) allowing the 5G-RANGE to make use of non-continuous portions of the spectrum as required (Req-F.m.5, Req-F.m.6). This waveform also offers better spectral efficiency than traditional OFDM and, using modulations up to 256-QAM, the 5G-FlexNOW block can offer a high spectral efficiency (Req-F.m.11).

Also, this section proposed the numerology for the 5G-RANGE, including the rationale for the selected parameters. By adopting the same scalable numerology approach used in 5G-NR, it is possible to address the conflicting requirements with different numerologies. By changing the numerology dynamically (Req-F.m.13), according to the actual channels state and mobility, 5G-RANGE PHY is able to be robust against severe multipath channel and also support high Doppler shift (Req-F.m.8). The proposed numerology can deal with very long multipath channel response, up to 140 μ s and with mobile speed up to 240 km/h.

The scalable numerology approach aims to address all use cases described in [1], although there is no one to one relationship between the use cases and the numerologies. The best waveform numerology for every user connected to 5G-RANGE gNB will be selected according to the actual channel state. Nevertheless, the numerology was specified to cover or surpass the use case requirements.

The grouping of the radio resource in blocks in time-frequency grid allows for scheduling transmissions from any users located in the cell (Req-F.m.10). The proposed resource grid allows the coexistence of the multiple numerology in a frame and also allows the numerology to be adapted dynamically, according to the uses needs, in a subframe basis (Req-F.m.13).

This section also shown that recent advances in GFDM waveform with an even number of subcarriers and subsymbols [19] leads to a more efficient implementation using the novel structure proposed in [22], reducing the implementation complexity gap between OFDM and GFDM waveforms.

As with the 5G-ACRA, after the definition of the 5G-FlexNOW, an open task remains to define the MCS (modulation and coding scheme) table in collaboration with WP 4. This task is foreseen to be part of Task 6.1 *Software-based system integration* of WP 6.

4 Algorithms for 5G-IR2A

This section describes the algorithms used on the receiver side to recover the transmitted data both in uplink and downlink.

4.1 Synchronization

The PHY layer of the 5G-RANGE operates using synchronous transmissions. It requires all UE (user equipment) associated to the gNB to acquire synchronization in order to receive or transmit data. The UE must be able to identify the boundaries of a frame, sub-frame, and symbols on the downlink signal, to collect information from the frame structure. The UE must also be able to transmit data in the uplink with a known time relationship to the downlink transmissions. By doing so, the uplink transmissions are synchronous to the downlink.

The error between the instant the UE considers the start of a symbol, in respect to the actual start is the so-called STO (sampling time offset) measured in samples. The UE's are equipped with its own time references, which in turn, are used to create the local SR (sampling rate) and LO (local oscillator). Another important requirement for synchronization is that the LO frequency error in respect to the carrier frequency, and the UE SR to the gNB SR, to be negligible. The LO frequency error and the SR frequency error are known as CFO (carrier frequency offset) and SFO (sampling frequency offset) respectively, both measured in Hz.

The UE estimates its CFO, STO, and SFO from the downlink signal, using the reference signals located in specific positions in the time-frequency grid. The first step in the synchronization process is to obtain the necessary initial information through a licensed control channel (specified by functional requirement Req-F.m.3 in [1]), which is especially dedicated for this purpose. As mentioned before (see Section 3.2.2.1), one of the main problems 5G-RANGE has to cope with is the usage of fragmented spectrum. This characteristic prevents 5G-RANGE from applying a conventional initial synchronization procedure as defined in 5G NR. Only after having obtained information about important configuration parameters, such as the operating carrier frequency or the location of the reference signals, the UE can continue with the estimation of the synchronization parameters, adopting the algorithms suitable for 5G NR. Figure 29 shows the PSS in the time-frequency grid. The PSS signal is transmitted on the first symbol at the beginning of every radio frame and is transmitted surrounded by a guard band to allow for its separation through a filtering process.

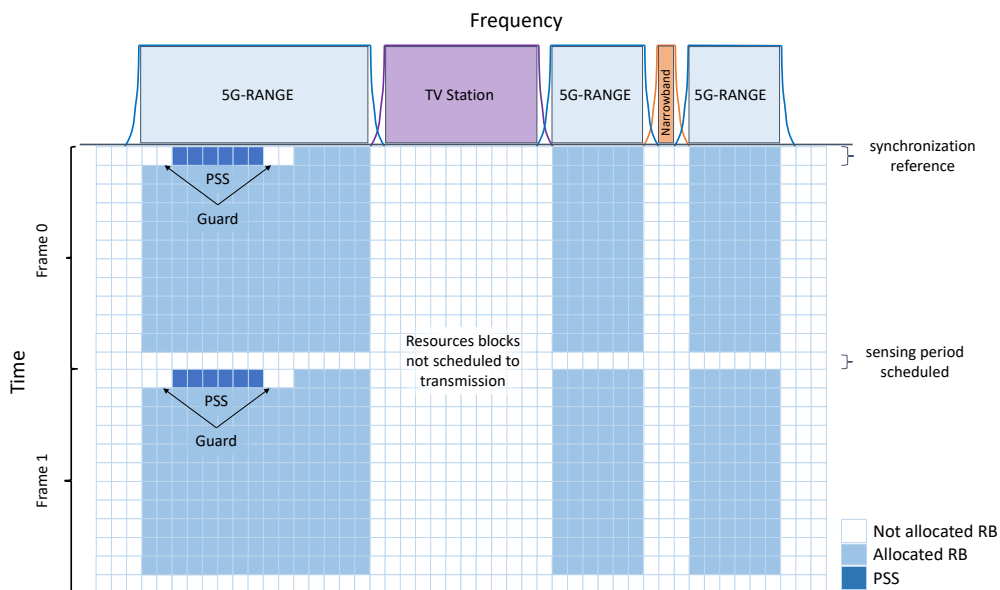


Figure 29: PSS in the time-frequency grid. The parameters needed to extract the PSS are provided by the control channel.

The next step in the synchronization procedure is to obtain the PSS through filtering of the received signal in the corresponding frequency band, defined by the control channel. The periodicity of this signal can be exploited to perform an algorithm based on the autocorrelation, with double sliding window, as presented in [32]. The maximum of this metric provides a coarse estimation of the frame arrival. To refine this timing estimation, the received signal is correlated with the PSS available at the receiver [33]. The estimated frame arrival is defined by the maximum of the output of the cross-correlation, which should be a peak exceeding a certain threshold. However, due to the periodicity of the PSS, the output of this metric will exhibit not only one peak, but also secondary peaks, which can be reduced in a further step through the multiplication of the previously calculated autocorrelation with the cross-correlation [33]. The fine timing estimation obtained with this modified timing metric is used as a reference to calculate the frequency offset, obtained through the phase of the initially calculated autocorrelation at the point indicated by the timing estimation.

The mentioned approach should be able to estimate the maximum CFO which can appear in the system. Considering a carrier frequency of 800 MHz and oscillators with 1ppm accuracy. The CFO due to the inaccuracies of the oscillators is 1600 Hz. Besides, the Doppler effects due to the UE mobility should be considered. For a maximum mobile speed of 240 km/h and the mentioned carrier frequency, this frequency offset is 177.78 Hz. The theoretical maximum CFO considering both effects would be 1.78 kHz, which is lower than the SCS of the first numerology. Therefore, only fractional CFO is expected in this system, justifying the use of the proposed approach for this purpose. In addition, the specifications for the accuracy of the oscillators defined in [34] are more restricted than the 1 ppm considered here. Hence, the design would not necessarily require the use of oscillators with the accuracy required by the standard, which would relax the costs of the system.

The received signal, after compensation of the estimated frequency offset and subsequent removal of CP, can be sent to the next block for further processing. Furthermore, the PSS and SSS contained in an SSB are used to extract the radio frame and sub-frame boundaries, as well as the NID (NR cell identity). With this information, the UE can use the PBCH DMRS to decode the information contained in the data field of the PBCH or MIB. In [35] and [36], the authors present an overview on the synchronization procedures for 5G NR.

4.2 Channel estimation

The channel estimation performance is crucial for the overall system performance, since it limits the performance of all subsequent stages. Furthermore, channel estimation for non-orthogonal waveforms is much more challenging than channel estimation in orthogonal systems like the widely used OFDM. The reason for this is that channel estimation is usually based on the observation of known pilots. However, in non-orthogonal waveforms, the pilot observations will, in general, be distorted by ISI (inter-symbol interference), ICI (inter-carrier interference) and, in MIMO systems, IAI (inter-antenna interference). These interferences are generally caused by unknown data bits and cannot be easily canceled out.

Early works on GFDM channel estimation investigate the performance loss due to the unknown interference [37], [38]. An error floor or a non-negligible performance gap is shown for conventional channel estimation approaches. Therefore, the remainder of this section introduces two advanced channel estimation schemes for GFDM, which are applied in 5G-RANGE to ensure robust communication over the challenging channel model (cf. [2]).

4.2.1 Interference-free pilots insertion

This section describes an IFPI (interference free pilots insertion) approach for GFDM, which was first introduced in [39]. The idea is to insert the pilots into the signal such that they are orthogonal to the data symbols in the frequency domain. Consequently, frequency domain channel estimation algorithms developed for OFDM can be applied.

A GFDM modulated transmit signal \mathbf{x} can be written in linear form as

$$\mathbf{x} = \mathbf{A}\mathbf{d} = \mathbf{A}(\tilde{\mathbf{d}} + \check{\mathbf{d}}), \quad (23)$$

where \mathbf{A} denotes the modulation matrix and $\tilde{\mathbf{d}}$ and $\check{\mathbf{d}}$ only contain pilot and data symbols, respectively. This means that $\tilde{\mathbf{d}}$ contains zeros at all pilot positions and vice versa. We assume a GFDM configuration with K subcarriers and M subsymbols, such that the total number of samples is $N = KM$. The transmit signal can be written in a slightly more restricted form as

$$\check{\mathbf{x}} = \mathbf{F}_N^H \sum_{k=0}^{K-1} \mathbf{P}^{(k)} \mathbf{G}^{(\delta)} \mathbf{R}^{(\delta)} (\Gamma \tilde{\mathbf{d}}_k + \mathbf{F}_M \check{\mathbf{d}}_k), \quad (24)$$

where \mathbf{F}_N denotes a DFT matrix of size N , $\mathbf{R}^{(\delta)} = [\mathbf{I}_M, \mathbf{I}_M, \dots, \mathbf{I}_M]^T$ performs δ -fold repetition and $\Gamma = \mathbf{P}' \text{blkdiag}(\lambda \mathbf{I}_{n_T}, \mathbf{F}_{M-n_T})$, where $\mathbf{P}^{(k)}$ and \mathbf{P}' denote permutation matrices [21], [39]. The $\text{blkdiag}(\cdot)$ operator creates a block diagonal matrix from the argument, a detailed definition is provided in [39]. The value of δ depends on the number of non-zero pulse shaping filter coefficients in the frequency domain. Using the above definition ensures that there is no interference between data and pilots. However, the frequency bins for pilots have to be chosen in the middle of the subcarrier, such that there is no ICI from adjacent subcarriers. Also, the scheme allows to allocate one or multiple pilots per antenna and to NULL the chosen pilots for the other antennas, such that channel estimation per transmit antenna can be performed in a MIMO setting. Figure 30 provides an example on the IFPI scheme for two antennas. It also illustrates why the pilots should be allocated in the middle of the subcarrier. The scheme just ensures no interference within the subcarrier. Still, there could be interference from subcarriers 1 or 3, if the pilots are allocated too far to the left or right.

The effect of pilot insertion on the GFDM PAPR (peak-to-average-power ratio) and on the PSD (power spectral density) were investigated in [39]. It was found that both are only slightly degraded. Furthermore, the scheme also exhibits a very low implementation complexity, since simple frequency domain channel estimation algorithms for orthogonal multicarrier systems like OFDM can be applied. As a result, we propose the IFPI channel estimation method as the main channel estimation algorithm for 5G-IR2A.

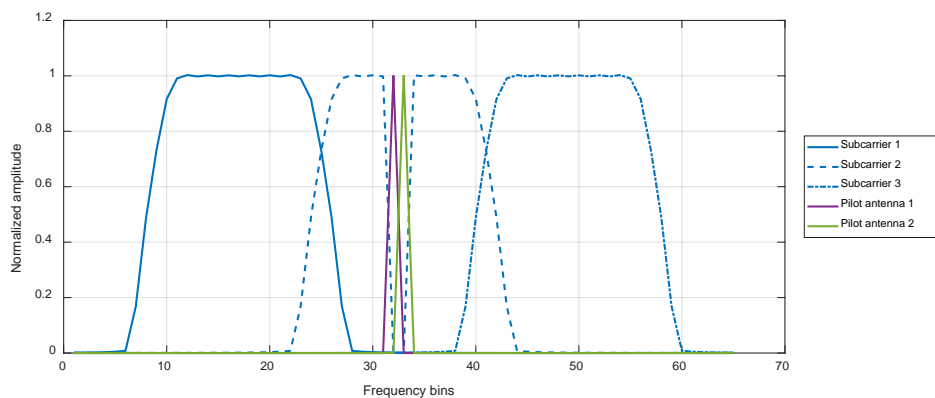


Figure 30: Example of IFPI scheme, which illustrates, why the pilots should be allocated in the middle of the subcarrier to avoid ICI from adjacent subcarriers.

4.2.2 Advanced Pilot- and CP-aided channel estimation for non-orthogonal waveforms

This section introduces a new advanced Pilot- and CP-aided channel estimation strategy for non-orthogonal waveforms, which was first published in [40]. In most practical receivers, CP is discarded. In contrast, we propose to use the information from the CP at the receiver to enhance the channel estimation performance of non-orthogonal waveforms.

In the remainder of this section, the channel is assumed to be a Rayleigh block fading channel with impulse response $\mathbf{h} \in \mathbb{C}^L$. Firstly, the N dimensional transmit signal is defined as

$$\mathbf{x}_N = \mathbf{A}\mathbf{d}, \quad (25)$$

where $\mathbf{d} \in \mathbb{C}^N$ and $\mathbf{A} \in \mathbb{C}^{N \times N}$ denote a vector of transmit symbols, e.g. obtained by mapping bits to a QAM constellation set, and the linear GFDM modulation matrix. Adding a CP of length N_{CP} can be described as

$$\mathbf{x}_{N'} = \begin{bmatrix} \mathbf{A}_{\text{CP}} \\ \mathbf{A} \end{bmatrix} \mathbf{d}, \quad (26)$$

where $\mathbf{A}_{\text{CP}} \in \mathbb{C}^{N_{\text{CP}} \times N}$ contains the last N_{CP} rows of \mathbf{A} and $N' = N + N_{\text{CP}}$. Assuming block fading over two consecutive transmit signals $\mathbf{x}_{a,N'}$ and $\mathbf{x}_{b,N'}$ of length N' yields the following linear system model

$$\mathbf{y}_{2N'} = \mathbf{T}_{2N'} \mathbf{x}_{2N'} + \mathbf{w}_{2N'} \quad (27)$$

with $\mathbf{x}_{2N'} = [\mathbf{x}_{a,N'}^T \mathbf{x}_{b,N'}^T]^T$, a Toeplitz channel matrix $\mathbf{T}_{2N'} \in \mathbb{C}^{2N' \times 2N'}$, where the beginning of the first column is given by \mathbf{h} , and AWGN (additive white Gaussian noise) $\mathbf{w}_{2N'} \sim \mathcal{CN}(\mathbf{0}, \sigma_w^2 \mathbf{I}_{2N'})$. It is assumed that only the second transmit signal $\mathbf{x}_{b,N'}$ contains pilots for channel estimation. The first transmission signal $\mathbf{x}_{a,N'}$ is only considered, because it leads to ISI (inter-symbol interference) in the CP of $\mathbf{x}_{b,N'}$. Therefore, for channel estimation, only the last $N'' = N + 2N_{\text{CP}}$ samples of $\mathbf{y}_{2N'}$ have to be considered and are hence denoted as

$$\mathbf{y}_{N''} = \mathbf{T}_{N''} \mathbf{x}_{N''} + \mathbf{w}_{N''}. \quad (28)$$

In order to obtain the parts of $\mathbf{y}_{N''}$ which contain pilots, the following windowing matrix is defined

$$\mathbf{J} = \begin{bmatrix} \mathbf{0}_{N' \times N_{\text{CP}}} & \mathbf{I}_{N'} \end{bmatrix}. \quad (29)$$

Unfortunately, $\mathbf{T}_{N''}$ cannot be diagonalized, because it is a Toeplitz matrix. In order to overcome this issue, we redefine (29) above with a circulant version of $\mathbf{T}_{N''}$, denoted as $\mathbf{C}_{N''}$

$$\mathbf{y}_{N'} \triangleq \mathbf{J}(\mathbf{C}_{N''} \mathbf{x}_{N''} + \mathbf{w}_{N''}). \quad (30)$$

Note that this does not invalidate equation (30), because the windowing matrix \mathbf{J} only cuts out the valid part of the equation. A graphical illustration is given in Figure 31.

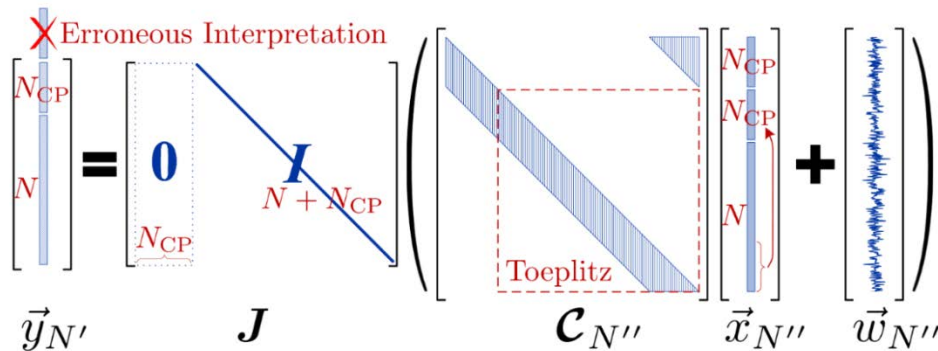


Figure 31: Illustration of the redefinition of $\mathbf{T}_{N''}$ as a circulant matrix $\mathbf{C}_{N''}$, which does not invalidate $\mathbf{y}_{N'}$ [40].

Now diagonalizing the circulant channel matrix with the DFT (discrete Fourier transform) and manipulating the expressions yields

$$\mathbf{y}_{N'} = \mathbf{J}(\sqrt{N''} \mathbf{F}_{N''}^H \mathbf{X}_{N''} \mathbf{F}_{N'',L} \mathbf{h} + \mathbf{w}_{N''}), \quad (31)$$

which is a standard Gaussian model and, hence, the LMMSE (linear minimum mean square error) estimate $\hat{\mathbf{h}}$ of \mathbf{h} can be obtained by the Bayesian Gauss-Markov theorem [41]. The LMMSE estimate and the estimation error covariance are given by [40]

$$\hat{\mathbf{h}} = \mathbf{\Sigma}_{hh} \mathbf{Q}_p^H (\mathbf{Q}_p \mathbf{\Sigma}_{hh} \mathbf{Q}_p^H + \mathbf{\Sigma}_{\psi\psi}^I)^{-1} \mathbf{y}_{N'} \quad (32)$$

$$\hat{\mathbf{\Sigma}}_{hh} = \mathbf{\Sigma}_{hh} - \mathbf{\Sigma}_{hh} \mathbf{Q}_p^H (\mathbf{Q}_p \mathbf{\Sigma}_{hh} \mathbf{Q}_p^H + \mathbf{\Sigma}_{\psi\psi}^I)^{-1} \mathbf{Q}_p \mathbf{\Sigma}_{hh}, \quad (33)$$

where $\mathbf{Q}_p^H = \sqrt{N''} \mathbf{J}_{N''}^H \mathbf{X}_{N'',L} \mathbf{F}_{N'',L}$ is the observation matrix and $\mathbf{\Sigma}_{\psi\psi}^I \in \mathbb{C}^{N' \times N'}$ is the covariance matrix of the noise plus interference terms given in [40]. This reference also provides an extension to MIMO and a LMMSE PIC (parallel-interference-cancellation) extension of the algorithm. Furthermore, numerical evaluations show that the proposed channel estimation technique achieves an up to 2.4 dB lower FER (frame-error ratio) using CP information of pilots for GFDM as compared to OFDM. Note that this approach can also be applied for other non-orthogonal waveforms by changing the modulation matrix \mathbf{A} accordingly.

4.2.3 Performance evaluation

In this section, the performance of the proposed IFPI scheme is investigated in a practical setting including the 5G-RANGE channel models, which are described in [2]. The performance is investigated in terms of SER (symbol-error ratio) after ZF GFDM demodulation using hard de-mapping of 64-QAM constellation symbols. We compare the performance with estimated channel to the performance of demodulation with perfect CSI (channel state information), which yields an upper bound on the system performance. Numerical results were obtained using the simulation framework described in Section 2.1.1. The results are depicted in Figure 32 as the average SER over 10^4 random channel realizations. The channel estimation loss at a practical operating point $\text{SER} = 10^{-2}$ for the NLOS and LOS channel model are ~ 0.8 dB and ~ 1 dB, respectively. Figure 33 evaluates the channel estimation performance of the IFPI scheme for 5G-FlexNOW numerology 4, which is designed for mobile speeds up to 120 km/h, in a setting with QPSK. From the evaluation, it can be seen that the performance degrades only slightly with increasing mobile speed. From evaluations in [2], it can be concluded that the system performance after channel coding is usually close to optimal for SER below 10^{-2} . Therefore, the system is expected to be robust against high Doppler shifts and mobile speeds (even beyond 120 km/h) under the investigated conditions for $\frac{E_S}{N_0} \geq 20$ dB. As a result, it can be concluded that (Req-F.m.8) is fulfilled by the system.

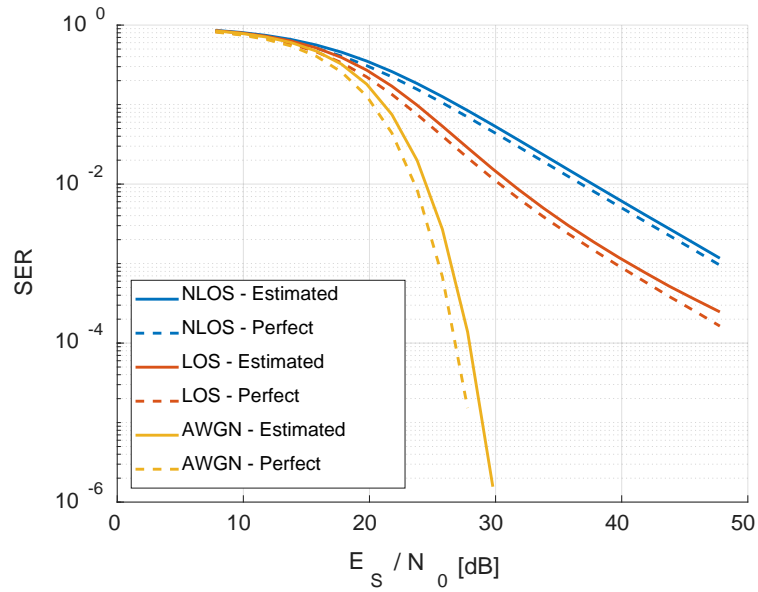


Figure 32: Evaluation of IFPI channel estimation performance in terms of SER for estimated and perfect CSI over AWGN and 5G-RANGE LOS and NLOS channel models.

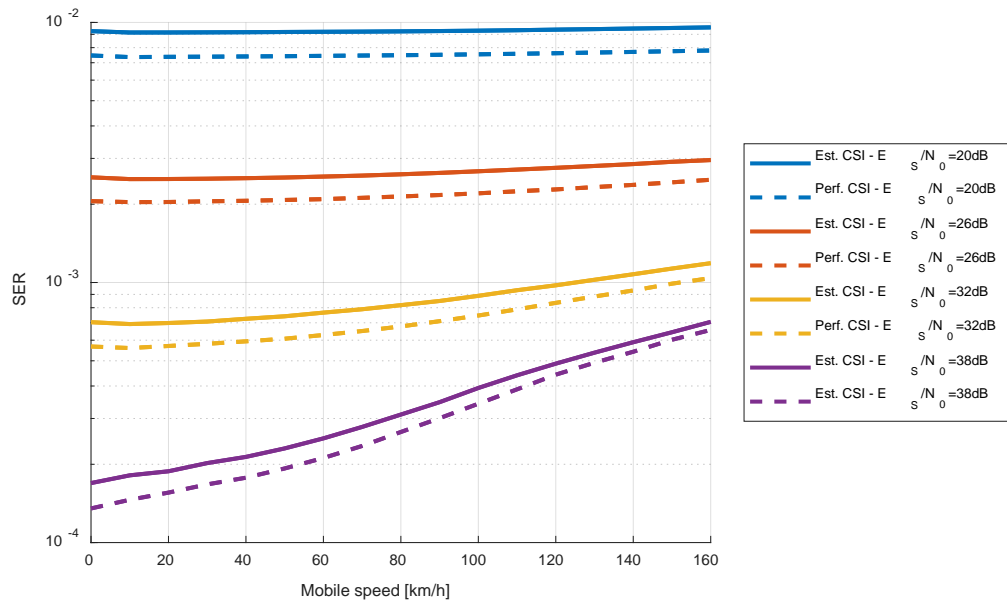


Figure 33: Evaluation of IFPI channel estimation performance over the NLOS channel model with mobility in the range $[0,160]$ km/h. The evaluation uses the numerology ID=4 from the 5G-FlexNOW specification in Table 17.

4.3 Definition and specification of 5G-IR2A

The specification of 5G-IR2A is provided in Table 18.

Table 18: Specification of 5G-IR2A.

5G-IR2A	
Synchronization	
Signals	SSB, PSS, SSS as defined in section 3.2.2.1
Algorithm	Extraction of PSS, Autocorrelation, Cross-correlation as defined in section 4.1
Channel estimation	
Signals	DM-RS, CSI-RS, SRS inserted into the transmission using IFPI technique as defined in 3.2.2.2.
Algorithm	IFPI scheme as described in 4.2.1, followed by frequency domain channel estimation with FFT based interpolation (optional: Advanced CP-aided channel estimation as described in section 4.2.2).

4.4 Discussions and future perspectives

In this section, we discussed synchronization for 5G-RANGE which is mainly based on the 5G NR synchronization scheme. For channel estimation, two schemes, namely interference free pilots insertion and CP-aided channel estimation were introduced. Both channel estimation schemes are shown (in the references for CP-aided channel estimation) to be extremely powerful and yet exhibit a low complexity. Employing these schemes, it has been shown in 4.2.3 that the performance of the channel estimation is already close to optimal. Furthermore, the performance evaluation shows that the system is very robust against distortions introduced by the communication channel, which leads to the conclusion, that Req-F.m.8 is fulfilled. Consequently, 5G-IR2A provides robust yet low complexity synchronization and channel estimation to enable an affordable radio access network for the application in the 5G-RANGE use cases in remote and rural areas.

5 MIMO techniques for 5G-MIMORA

Among the requirements on the 5G-RANGE PHY, the ones related with robustness (Req-F.m.8) and data rate (Req-Q.m.6) stand out as most challenging. In general, MIMO (multiple input multiple output) techniques describe the utilization of multiple transmit and receive antennas to enhance the system performance. These MIMO techniques are essential to meet the mentioned requirements [42] [43]. The benefits of MIMO techniques are achieved exploiting the spatial domain in addition to the time and frequency domains already used by single antenna or SISO (single input single output) systems.

MIMO techniques with spatial diversity allow for improving the BER performance for a given SNR value, because redundant information is transmitted on different antennas using space-time coding [43]. Hence, diversity schemes are essential to fulfill Req-F.m.8. To process the received signal with spatial diversity techniques, special signal processing algorithms for combining the redundant signals and to retrieve the original data stream are applied. Optionally, multiple receive antennas can be employed to improve the system's performance by harvesting diversity gain at the receiver. Some example of spatial diversity techniques are the so-called Alamouti scheme [44] and trellis space-time-codes [45].

SM (spatial multiplexing) techniques, on the other hand, employ multiple antennas to transmit different data streams, or layers, simultaneously. A system that uses J transmit antennas and J receive antennas can increase the data rate up to J times when compared to the same system with single antenna [42]. Therefore, spatial multiplexing is beneficial to increase the overall throughput of the system. This improvement is obtained without requiring extra transmission bandwidth. The gain obtained on the data rate is called multiplexing gain [43]. IAI is solved at the receiver by interference cancellation algorithms, which are employed in association with multiple reception antennas techniques. Some example of interference cancellation algorithms commonly used in spatial multiplexing are ZF (zero forcing), MMSE (minimum mean square error), sphere decoding and BLAST (Bell-Labs layered space-time architecture) and its derivations. The following subsections present more details about the specific application of the spatial diversity and spatial multiplexing in 5G-MIMORA.

5.1 Diversity schemes

The STC (space-time coding) proposed by Alamouti [44] explores the diversity of the channel in space and time domains in order to achieve a diversity gain proportional to the product of the number of transmit antennas by the number of receive antennas. A basic overview on a MIMO system with 2 transmit and 2 receive antennas is illustrated in Figure 34.

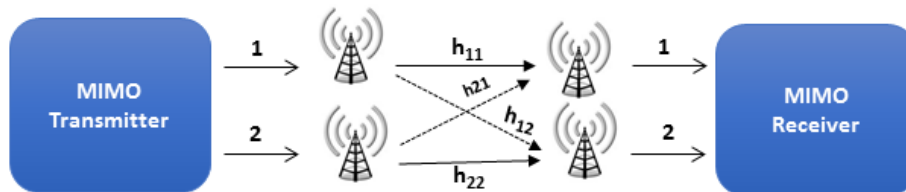


Figure 34: 2x2 MIMO system.

Using space-time coding techniques on fading channels allows to achieve diversity gains without decreasing the data rate [46]. The STC technique was combined with GFDM modulation in [47]. This work analyzes the coding efficiency and robustness in severe fading environments. It has been proven that these two techniques can be easily integrated to achieve the maximum gain of diversity with low implementation complexity. Depending on the prototype filter, the GFDM modulation becomes non-orthogonal. That is, the transmitted signals have ISI and ICI. When the pairs of modulation symbols used in the STC belong to the same GFDM symbol, there is a loss of performance in gaining diversity because the GFDM symbol must be equalized before the STC decoding process. As a solution to this problem, the TR-STC (time reversal space time coding) technique can be used with the GFDM

modulation [48]. Space-time codes can be applied to modulating symbols, such as QAM symbols, or blocks of modulating symbols, such as OFDM or GFDM symbols. The TR-STC technique, for example, is applied to GFDM Symbols.

The basic representation of TR-STC system is illustrated in Figure 35, where $(.)^H$, \mathbf{F}_N and \mathbf{X}_i correspond to transposing and conjugating operation, the N dimensional discrete Fourier transform matrix and the i -th OFDM or GFDM block in the frequency domain, respectively.

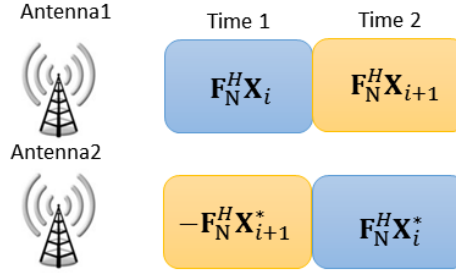


Figure 35: Basic representation of STC.

The space-time coding operates on two sets of OFDM or GFDM blocks, \mathbf{x}_i and \mathbf{x}_{i+1} . Two transmitting antennas transmit the data separately on two consecutive periods of time. During the transmission of block i , antenna 1 transmits the signal $\mathbf{F}_N^H \mathbf{X}_i$, and antenna 2 transmits $-\mathbf{F}_N^H \mathbf{X}_{i+1}^*$. At the subsequent instant of time, antenna 1 transmits $\mathbf{F}_N^H \mathbf{X}_{i+1}$ and antenna 2 transmits $\mathbf{F}_N^H \mathbf{X}_i^*$. This distinction of transmitting symbols, both in space (by two antennas) and in time (two subsequent time slots), represents the time-space coding.

The received symbols can be described in the frequency domain as:

$$\begin{aligned} \mathbf{Y}_{i,l} &= \hat{\mathbf{H}}_{1,l} \mathbf{X}_i - \hat{\mathbf{H}}_{2,l} \mathbf{X}_{i+1}^* + \mathbf{W}_{1,l} \\ \mathbf{Y}_{i+1,l} &= \hat{\mathbf{H}}_{1,l} \mathbf{X}_{i+1} + \hat{\mathbf{H}}_{2,l} \mathbf{X}_i^* + \mathbf{W}_{2,l}, \end{aligned} \quad (34)$$

where l and i represents the receiver antenna and data block indexes, respectively. The matrix $\hat{\mathbf{H}}_{j,l}$ represents the estimated channel, where j is the transmit antenna index, \mathbf{W} represents the AWGN noise in the frequency domain. These signals can be combined in order to achieve the maximum gain of diversity, leading to

$$\begin{aligned} \hat{\mathbf{X}}_i &= \mathbf{H}_{eq}^{-1} \sum_{l=1}^L (\hat{\mathbf{H}}_{1,l}^* \mathbf{Y}_{i,l} + \hat{\mathbf{H}}_{2,l} \mathbf{Y}_{i+1,l}^*) \\ \hat{\mathbf{X}}_{i+1} &= \mathbf{H}_{eq}^{-1} \sum_{l=1}^L (\hat{\mathbf{H}}_{1,l} \mathbf{Y}_{i+1,l} - \hat{\mathbf{H}}_{2,l} \mathbf{Y}_{i,l}^*) \end{aligned} \quad (35)$$

where

$$\mathbf{H}_{eq} = \sum_{l=1}^L \sum_{j=1}^2 \hat{\mathbf{H}}_{j,l} \odot \hat{\mathbf{H}}_{j,l}^* \quad (36)$$

and \odot represents the Hadamart product. After combining the signals, the estimated symbols can be obtained by

$$\hat{\mathbf{d}}_i = \mathbf{B} \mathbf{F}_N^H \hat{\mathbf{X}}_i \quad (37)$$

where \mathbf{B} is the demodulation matrix, e.g. $\mathbf{B} = \mathbf{A}^{-1}$.

5.1.1 Space-Time code performance

In frequency selective channels, the SER performance of STC-GFDM varies according to the number of transmitting antennas J and the number of receive antennas L , and can be estimated by [16]

$$p_e \approx 4\tau \sum_{i=0}^{JL-1} \left(\frac{JL-1+i}{i} \right) \left(\frac{1+\eta}{2} \right)^i, \quad (38)$$

where

$$\tau = \left(\frac{k-1}{k} \right) \left(\frac{1-\eta}{2} \right)^{JL} \quad (39)$$

and $k = \sqrt{2^u}$, with u being the the number of bits per data symbol and

$$\eta = \frac{\sqrt{\left(\left(\frac{3h_e^2}{2^u-1} \right) \left(\frac{E_s}{\varepsilon_0 N_0} \right) \right)}}{\sqrt{2 + \frac{3h_e^2}{2^u-1} - \frac{E_s}{\varepsilon_0 N_0}}}, \quad (40)$$

where E_s is the symbol mean energy, N_0 is the AWGN power spectral density and ε_0 is noise enhancement factor. Given that

$$h_e^2 = \sum_n E[|h_n|^2], \quad (41)$$

where h_n represents the channel impulse response, and considering K subcarriers, M subsymbols, N_{CP} samples of cyclic prefix and N_{CS} samples for cyclic suffix, the noise enhancement factor can be stated as

$$\varepsilon_{0,\text{GFDM}} = \varepsilon \left(\frac{KM+N_{cp}+N_{cs}}{KM} \right). \quad (42)$$

The performance of the STC technique applied to GFDM was analyzed through a simulation whose parameters considered are presented in Table 19.

Table 19: STC simulation parameters.

Parameter	Value
Waveform	GFDM
Mapping	16-QAM
GFDM shaping filter	Raised Cosine
Pulse shaping filter roll-off	0,25
Number of subcarriers (K)	512
Number of subsymbols (M)	3
Samples of Cyclic prefix (N_{CP})	16
Samples of cyclic suffix (N_{CS})	0
Transmission technique	SISO and STC MIMO

The mean channel delay profile for each paths is presented by in Table 20. During the simulation, for each pair of GFDM symbols, the paths were multiplied by a complex random variable with normal distribution according to $h_r \sim N(0,1)$.

Table 20: Channel profile considered on the simulation.

channel path (n)	0	1	2	3	4	5	6
$h_{(n)}$ [dB]	0	-1	-2	-3	-8	-14,2	-20,8

Figure 36 illustrates the performance in terms of SER for a GFDM system with single and multiple antennas, respectively. It is possible to observe the STC-GFDM performance gain over the conventional GFDM. The evaluation shows how STC techniques enable robust communication over long-range channels with severe multipath, hence fulfilling Req-F.m.8.

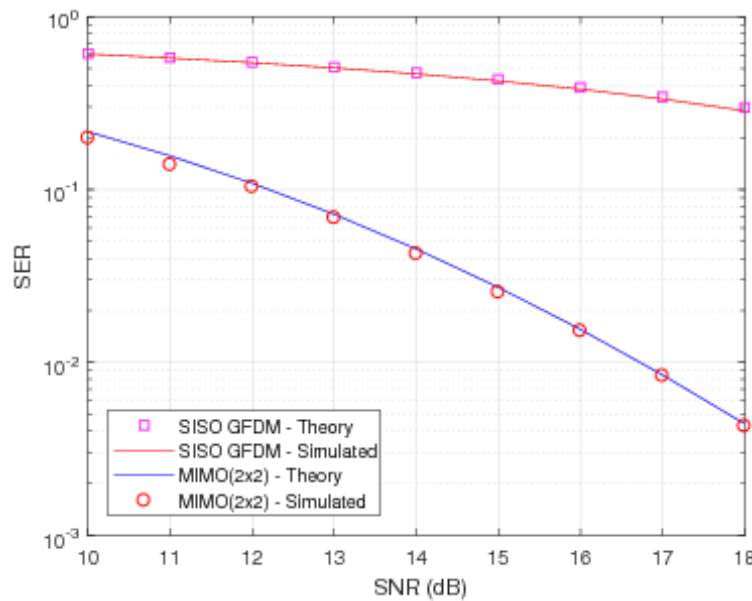


Figure 36: STC simulation on performance gain for GFDM modulation.

5.2 Multiplexing schemes

The spatial multiplexing, initially described in [49], consists of demultiplexing the input data in J streams, which are modulated and transmitted simultaneously on the same frequency by J transmit antennas [42]. To separate the different streams at the receiver side, L receive antennas are used together with algorithms for IAI cancellation. Figure 37 illustrates the basic architecture described for a spatial multiplexing MIMO system.

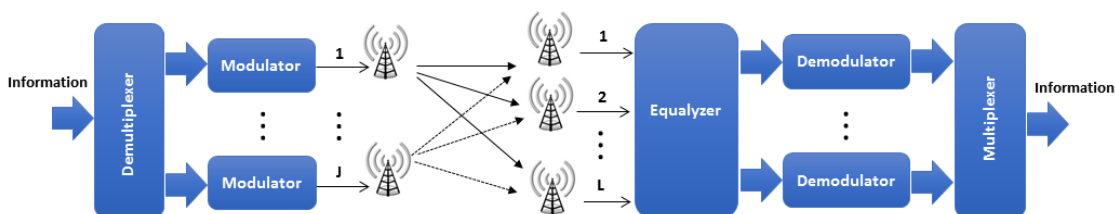


Figure 37: Basic architecture of spatial multiplexing.

Each interference cancellation algorithm, also called channel detector or equalizer, presents different performance and level of implementation complexity. The algorithm class called linear receivers

employs some linear transformation of the received signal to estimate the transmitted symbols, such as ZF and LMMSE. Although they have low implementation complexity, this class of algorithms is not optimal. On the other hand, the ML (maximum likelihood), for example, presents optimal performance using a non-linear estimation technique. ZF, MMSE and ML will be presented in more details in the next subsections. Note that the specification of 5G-FlexNOW in Table 17 specifies GFDM modulation with roll-off factor $\alpha = 0$, hence yielding an *orthogonal* modulation scheme. As a result, we can apply low complexity MIMO algorithms, which are initially developed for OFDM.

5.2.1 Introduction to zero-forcing and least minimum mean square error algorithms

Consider initially a MIMO system with two transmit and two receive antennas, denoted as $J = L = 2$, and employing spatial multiplexing, as showed in Figure 37. The signals received for a given subcarrier are

$$\begin{aligned} Y_1 &= H_{11}X_1 + H_{21}X_2 + W_1 \\ Y_2 &= H_{12}X_1 + H_{22}X_2 + W_2, \end{aligned} \quad (43)$$

where Y_l is a QAM symbol received by the antenna l , X_j is a QAM symbol transmitted by the antenna j ; $H_{j,l}$ is the channel between the j transmit antenna and the l receive antenna for the subcarrier in question; W_l represents the AWGN noise in the frequency domain added to the signal received at antenna l .

Eq. (43) can be rewritten as

$$\mathbf{Y} = \mathbf{H}\mathbf{X} + \mathbf{W}, \quad (44)$$

where $\mathbf{Y} = [Y_1 \ Y_2]^T$, $\mathbf{X} = [X_1 \ X_2]^T$ and

$$\mathbf{H} = \begin{bmatrix} H_{1,1} & H_{2,1} \\ H_{1,2} & H_{2,2} \end{bmatrix}. \quad (45)$$

Using the received signals \mathbf{Y} and the estimated channel $\hat{\mathbf{H}}$, considered equal to \mathbf{H} for optimum channel estimation, is it possible to estimate the transmitted symbols $\hat{\mathbf{X}}$ generically given by

$$\hat{\mathbf{X}} = \mathbf{V}_{\text{eq}}\mathbf{Y}. \quad (46)$$

The evaluation of equalizer matrix \mathbf{V}_{eq} varies in accordance with the adopted algorithm. ZF leads to

$$\mathbf{V}_{\text{ZF}} = (\mathbf{H}^H\mathbf{H})^{-1}\mathbf{H}^H, \quad (47)$$

where \mathbf{V}_{ZF} corresponds to pseudo-inverse of \mathbf{H} [50] [51]. This algorithm usually works well at high SNR.

The LMMSE equalizer matrix is given by [51]

$$\mathbf{V}_{\text{MMSE}} = \left(\mathbf{H}^H\mathbf{H} + \frac{1}{\text{SNR}}\mathbf{I} \right)^{-1}\mathbf{H}^H, \quad (48)$$

where $\text{SNR} = \sigma_x^2/\sigma_w^2$.

For SNR, MMSE performances as ZF. On the other hand, for low SNR, MMSE outperforms ZF [52]. This difference is due to the fact that ZF introduces severe noise enhancement, while MMSE uses the SNR to avoid noise amplification at low SNR [50]. MMSE has a slightly higher implementation complexity because the noise variance needs to be constantly estimated [52].

5.2.2 Introduction to maximum likelihood and Sphere Decoder algorithms

The ML algorithm [53] [54] calculates the Euclidean distance d between the received data \mathbf{Y} and all possible receive symbols $\mathbf{H}\mathbf{x}_{hp}$. It is given by

$$\hat{\mathbf{X}} = \arg \min_{\mathbf{x}_{hp}} |\mathbf{Y} - \mathbf{H}\mathbf{x}_{hp}|^2, \quad (49)$$

where \mathbf{x}_{hp} represents a set of hypothetical transmitted symbols. The set of symbols \mathbf{x}_{hp} which minimizes the Euclidean distance is selected as the estimated transmitted symbols $\hat{\mathbf{X}}$.

The implementation complexity of the presented ML algorithm grows exponentially with the number of transmit antennas and the constellation size. Therefore, the study of sub-optimal estimators, which aim to achieve a close to ML performance with less complexity is a prominent research area. A widely adopted approach is the so-called SD (sphere decoder) which uses the same method as ML estimator, but it restricts the set of possible \mathbf{x}_{hp} to a multidimensional sphere. The radius of the sphere can be used to trade-off complexity vs performance.

ML and SD outperform ZF and MMSE. In contrast, the increase in performance is associated with a greater complexity of implementation, which increases exponentially with the number of antennas and the mapping order [55].

5.2.3 Spatial Multiplexing performance

Performance analysis of the spatial multiplex techniques was evaluated using a computer simulation. Table 21 shows the configurations considered in this simulation, while Figure 38 shows the performance results. From Figure 38 it can be concluded that the BER performance curves of the system with f-OFDM and GFDM, given the same equalization method achieve a similar performance. With respect to the equalization algorithms, it can be observed that, under the simulated conditions, ML achieves better BER performance, while ZF presents the worst performance.

It is important to notice that the performance achieved with spatial multiplexing depends on the channel characteristics, mainly the correlation among the paths. Also, the waveforms parameters, such as CP length, number of subcarriers and prototype filter can also severely impact the overall system performance.

Table 21: Spatial Multiplexing simulation parameters.

Parameter	Value
f-OFDM parameters	
FFT samples (all activated)	1024
Samples of CP	32
Filter Function	Sinc
Windowing Filter Function	Hanning
Filter samples	513
GFDM parameters	
Number of subcarriers (K) (all activated)	1024
Number of subsymbols (M) (all activated)	3
Samples of CP	32

Pulse Shapping Filter	Raised Cosine
Filter roll-off (α)	0
General simulation parameters	
Data Mapping	BPSK
Number of transmission antennas (J)	2
Number of receiver antennas (L)	2
Spatial Multiplexer Equalizer	ZF, MMSE and ML
Channel type	Rayleigh
Channel estimation	Optimum
Condition Number restriction	No

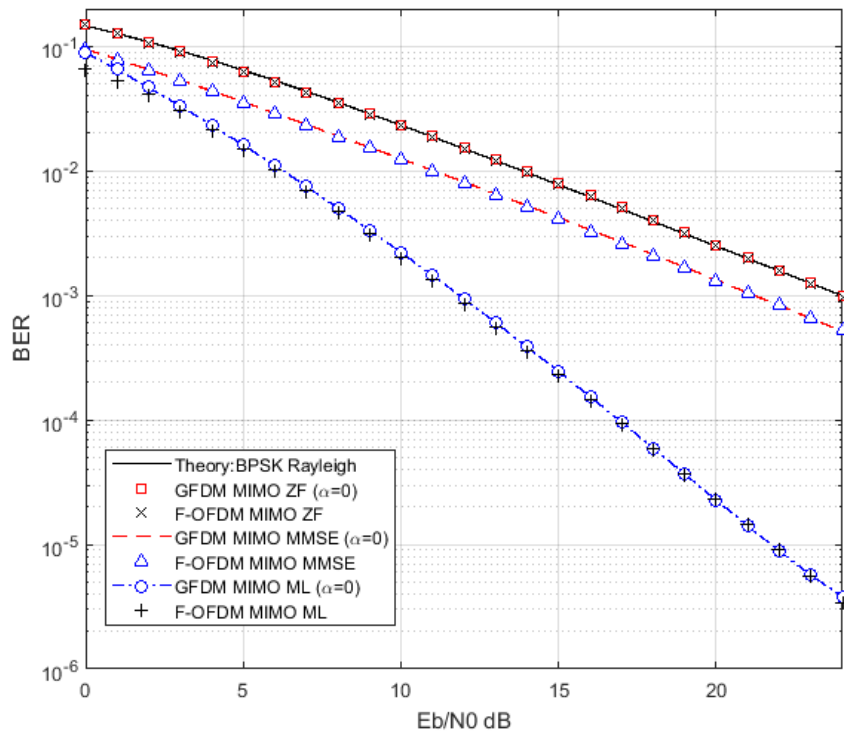


Figure 38: Spatial Multiplexing performance comparison for ZF, MMSE and ML algorithm and f-OFDM and GFDM modulation.

5.3 Impact of dual-polarized antennas on the channel capacity

In the previous sections, different strategies to achieve a diversity and multiplexing gain in MIMO systems were discussed. However, due to the required space separation between the antenna elements in the array, there is a physical limitation in the number of antennas at the transmitter and receiver sides, consequentially, in the channel capacity gain. One solution for this physical limitation is to employ dual-polarized antennas, both at the transmitter and receiver sides. This feature will virtually increase the size of the array by a factor of two. Figure 39 (a) shows a SISO system with dual-polarized antennas, while in Figure 39 (b) the *parallel* channel paths between the transmitter and receiver are shown. Note that SISO with dual-polarized antennas is actually MIMO, since the antenna has two feeders, one for each polarization. Nevertheless, it will be denoted as dual-polarized SISO in the remainder of this section.

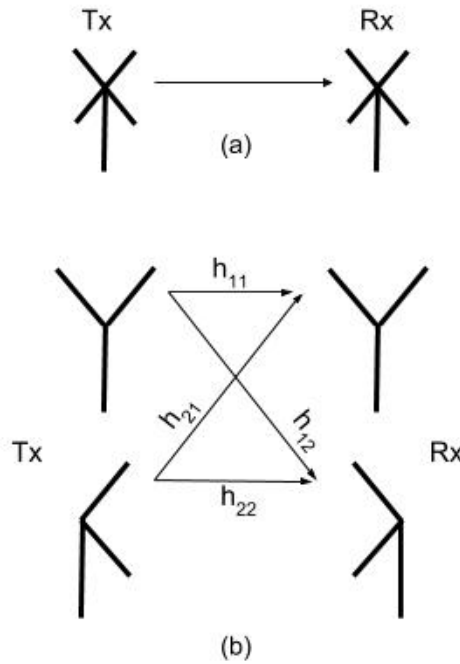


Figure 39: a) SISO with dual-polarized antennas. b) Channel between the vertical and horizontal polarized antennas, considered separately.

The use of dual-polarized antennas to achieve a higher diversity or multiplexing gain in MIMO systems is not new. In [56], a performance evaluation comparing the Alamouti OSTBC (orthogonal space-time block) with uncoded spatial multiplexing is done. In [57], a channel model for dual-polarized MIMO system with channel capacity evaluations is proposed. Other works, addressing the performance of polarized MIMO channels can be found, for instance, in [58] and [59]. For 5G networks, where the transmitter and the receiver may be equipped with a massive number of antennas, the physical spacing between the antennas is crucial. One solution to cope with that is the use of dual-polarized antennas at both ends of the wireless link. In [60], the authors propose a dual-polarized MIMO channel model for massive MIMO systems for human-care IoT devices. In [61], the authors propose a beamforming scheme by exploiting the dual-polarization diversity in 5G millimeter wave systems. In the following, simulation results of the proposed 5G-RANGE channel model form [2] together with dual-polarized antennas are discussed and evaluated in terms of the overall system throughput.

5.3.1 Simulation Results

In this section, the channel capacity results of Section 2.3 of [2] using SP (single-polarized) antennas at the transmitter and receiver side are extended to a setup considering DP (dual-polarized) antennas at both, the transmitter and the receiver. The simulation parameters are summarized in Table 22.

Table 22: Simulations parameters for the evaluation of dual-polarized antennas.

Parameter	Value	Unit
Cell radius	50	km
BS transmit power	49 and 53	dBm
Channel bandwidth	23.40	MHz
PRB (physical resource block) bandwidth	180	kHz
UE speed	3 and 120	km/h
Carrier frequency	700	MHz
Path loss model	FSPL 29.38	dB
Shadowing std.	4.47	dB
Antenna configuration	1x1, 2x2, 4x4	-
Rad. power pattern for BS and UE	Isotropic	-
Antenna gain for {BS, UE, CPE}	{9, 0, 9}	dBi
Polarization for BS and UE/CPE	{90° (SP)}, {-45°/+45° (DP)}	°
Noise figure	5	dB
Noise power per PRB	-116.45	dBm
Number of UEs	1	-
Monte Carlo runs	5000	-

As in [2], the CDF of the overall throughput was computed using the Shannon formula for the SISO and MIMO (2x2 and 4x4) configurations at the cell's edge, without considering any coding and frame structure, as follows

$$r_{\text{SISO}} = \sum_{k=1}^{N_{\text{PRB}}} B \log_2(1 + \text{SNR}_k) \quad (50)$$

and

$$r_{\text{MIMO}} = \sum_{k=1}^{N_{\text{PRB}}} B \log_2 \left(\det \left[\mathbf{I} + \frac{\eta}{\gamma^2} \mathbf{H}_k \mathbf{H}_k^H \right] \right), \quad (51)$$

where B is the PRB bandwidth, \mathbf{H} is the channel matrix with dimension N_{UE} by N_{BS} , and

$$\eta = \frac{P_{\text{BS}}}{N_{\text{PRB}} N_{\text{BS}}}. \quad (52)$$

In the scenario of Figure 40, it can be observed that, considering the 0.5 percentile of the CDF, all BS-CPE dual-polarized configurations achieve the KPI of 100 Mbps at the cell edge, while in the case of single-polarized antennas, this KPI is only achieved with 4x4 MIMO configuration. It can also be observed that the dual-polarized SISO configuration outperforms the single-polarized 2x2 MIMO. In addition, by increasing the transmission power to 53 dBm, as shown in Figure 41, the gap between single-polarized and dual-polarized MIMO also increases. This can be explained by the fact that, the 5G-RANGE propagation channel exhibits a poor scattering and small angular spread, leading to high

spatial correlation between two antennas. In this scenario, the benefit of polarization diversity becomes more effective than the array gain [57]. The results shown in Figure 42 and Figure 43 consider a LOS scenario by varying the transmission power. In this case, at the 0.5 percentile, the throughput of the BS-CPE SISO dual-polarized configuration is approximately the same as that of the BS-CPE 4x4 single-polarized MIMO one, indicating that virtualization of the array using dual-polarized antennas (thus creating parallel channel paths) is preferable than increasing physically the array size using more antennas.

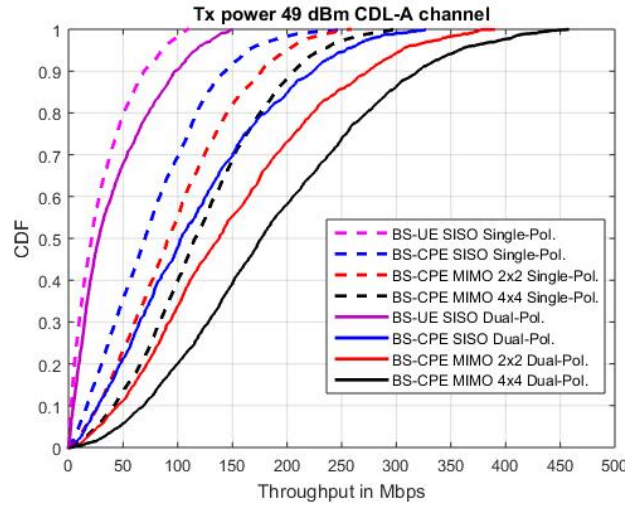


Figure 40: Channel throughput for a Tx power of 49 dBm, NLOS case.

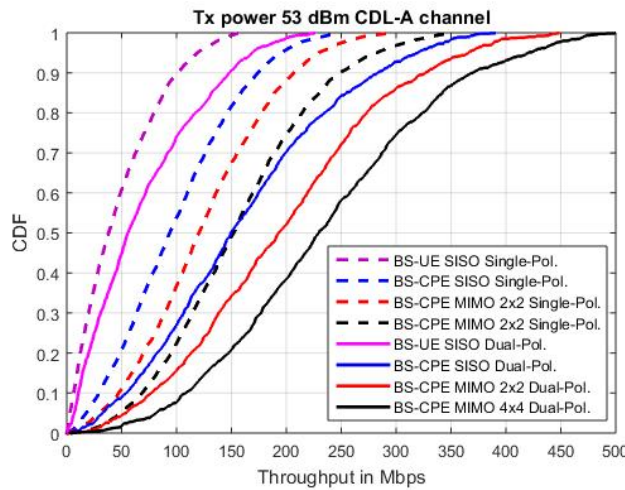


Figure 41: Channel throughput for a Tx power of 53 dBm, NLOS case.

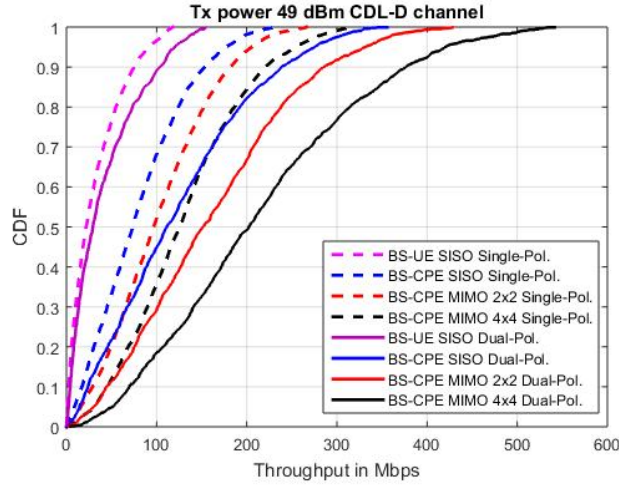


Figure 42: Channel throughput for a Tx power of 49 dBm, LOS case.

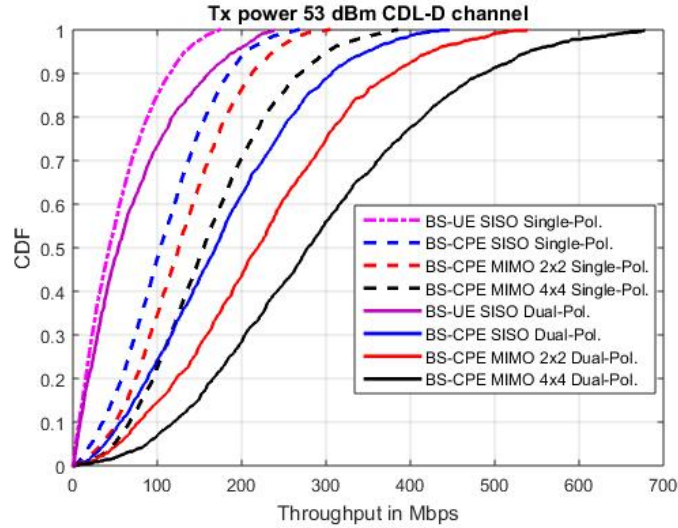


Figure 43: Channel throughput for a Tx power of 53 dBm, LOS case.

To obtain a better understanding of the impact of the results from Figure 40 to Figure 43, Table 23 shows the percentage of time, where a specific system achieves the 100 Mbps KPI. An interesting result that can be easily extracted from this table is that all transmissions BS-CPE using dual-polarized antennas achieve the KPI at least on average, i.e., 50% of the time.

Now, in Figure 44, the throughput in the uplink direction, i.e., CPE-BS is evaluated. The same parameters from Table 22 are assumed, with the exception that the transmission power of the CPE is considered to be limited to 21 dBm. In this case, the single-polarized antenna systems have a small gain over the dual-polarized antennas. This can be explained by the fact that, now, the transmitted power is much lower as compared to the scenarios in Figure 40 to Figure 43 (49 dBm and 53dBm), meaning a lower SNR regime, which favors the physical array gain, instead of the parallel channel gain provided polarization diversity [57]. Nevertheless, those are small gains compared with the downlink. It is important to mention that, since these throughput values, in Figure 40 to Figure 44, were computed using Shannon's capacity formula, these values can be considered as upper bounds for practical scenarios.

Table 23: Chance of the 100 Mbps KPI being achieved, according to the systems simulated in Figure 36 to 39.

		CDL-A		CDL-D	
		Tx 49 [dBm]	Tx 53 [dBm]	Tx 49 [dBm]	Tx 53 [dBm]
Single-Polarized Antennas	BS-UE SISO	1%	10%	2%	12%
	BS-CPE SISO	30%	45%	31%	50%
	BS-CPE MIMO 2x2	42%	62%	47%	64%
	BS-CPE MIMO 4x4	60%	77%	64%	78%
Dual-Polarized Antennas	BS-UE SISO	10%	26%	11%	27%
	BS-CPE SISO	50%	72%	54%	75%
	BS-CPE MIMO 2x2	66%	83%	69%	85%
	BS-CPE MIMO 4x4	80%	92%	82%	93%

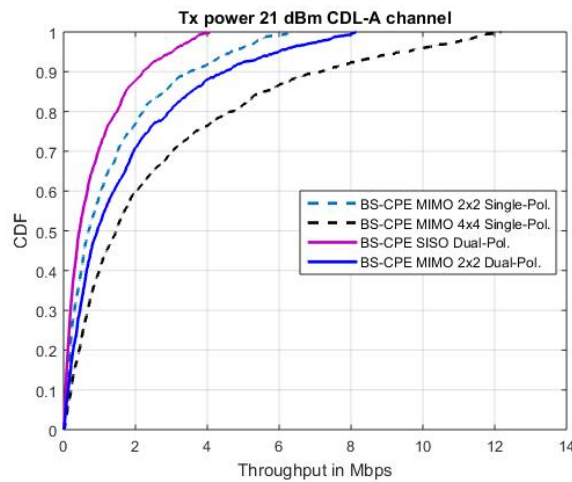


Figure 44: Channel throughput for a Tx power of 21 dBm, NLOS case.

According to the simulation results presented in this section, we conclude that the use of dual-polarized antennas is recommended for the 5G-RANGE project, not only for reducing the physical spacing of the antenna array, but also to provide additional diversity gains, especially in scenarios with moderate or high spatial correlation between the physical antennas of the array. As future perspectives, studies regarding the use of dual-polarized antennas at both the transmitter and the receiver side by considering the proposed waveform design, coding, and modulation scheme of the 5G-RANGE shall be performed in WP 6.

5.4 Definition and specification of 5G-MIMORA

The specification of 5G-MIMORA is provided in Table 24.

Table 24: Specification of 5G-MIMORA.

5G-MIMORA	
Diversity schemes	
Space-time coding	2x2 (supporting 2x1 and 1x2 operation)
Space-time coding rate	1
Multiplexing schemes	
Spatial multiplexing with LMMSE	2x2 and 4x4
Maximum channel matrix condition number	< 10 dB (up to 20dB with degradation)
Layer Precoding matrix	as specified in (TS 36.211) [62]

5.5 Discussions and future perspectives

In this section we introduced diversity and multiplexing schemes for the application in 5G-MIMORA, as specified in Table 24. For each scheme, a brief performance evaluation is provided to demonstrate the gains that can be obtained. More details on each scheme can be obtained from the literature. The most important contribution from this section is the evaluation of the impact of using dual-polarized antennas on the channel capacity (cf. Section 5.3). The evaluation shows that with dual-polarized antennas and the application of a CPE, the KPI of 100 Mbps at 50km radius will be achieved in at least 50% of the cases, even when only employing SISO. Furthermore, using dual-polarized antennas reduces the costs, which is important for the application in rural and remote areas.

In WP 6, the overall system performance with respect to the application of all the specified MIMO schemes has to be evaluated in system level simulations, which is beyond the scope of this deliverable.

6 PHY and MAC interface

This section briefly discusses the MAC and PHY interface. At the gNB side, the interface is based on the Small Cell Forum or FAPI (femtocell API) [63] [64], with interface messages using P5 PHY SAP (service access point) to configure the PHY layer, corresponding to the PHY mode control interface, and P7 PHY SAP to transmit downlink or receive uplink TBs (transport blocks), which corresponds to the data path interface. These TBs relate to MAC PDUs at the MAC layer. Messages are exchanged as APIs with TLV (tag-length-value) for both control (P5) and data (P7), including downlink and uplink interactions. The MAC scheduler commands the order or sequence of these messages, as described in [63].

6.1 Downlink interaction

The downlink transmission procedure at the gNB starts with the MAC layer sending the message DL_CONFIG.request(SFN=N) (P5 PHY SAP) to the PHY layer in order to configure this layer and to perform the corresponding downlink transmission. If the gNB has a MAC PDU (packet data unit) to transmit, the MAC layer also issues to the PHY layer the message TX.request() (P7 PHY SAP) carrying the MAC PDU. Thus, the DL_CONFIG.request message carries configuration information for each of the following 5G RANGE PHY components, such as:

- 5G-ACRA: Information containing the coding scheme, TB, and TB to code word mapping.
- 5G-FlexNOW: Information of modulation, resource allocation type that informs the granularity of resource allocation in subcarriers and slots (symbols), and codebook index.
- 5G-MIMORA: Transmission mode and MIMO configuration information with transmission scheme (SISO, Diversity, multiplexing, open loop, closed loop), number of layers, and transmission mode scheme.
- PHY Framer: Resource allocation information.

The same PHY information is also sent to the UE using DCI (downlink control information), to be able to the UE PHY to receive the downlink message containing the MAC PDU. The gNB PHY layer is responsible for coding the DCI and make use of the PDCCH (physical downlink control channel) for transportation of the DCI.

Furthermore, there is downlink transmission request with DL_CONFIG.request(SFN=N) message at the gNB without transmission of MAC PDU (with no TX.request() message). In this case, PHY layer performs only the coding of the DCI and use of the PDCCH for transport of this information to the UE. This is used for scheduling the UE uplink transmission with uplink grant, and in this case, the DCI message carries the UE side 5G RANGE PHY components configuration, in order to perform the uplink transmission.

6.2 Uplink interaction

As previous mentioned, UE PHY layer uplink transmission configuration is defined by the gNB and informed to the UE through the DCI. Based on this DCI information, the UE side 5G RANGE PHY components receive the same set of configurations described in Section 6.1, allowing the MAC PDU uplink transmission.

In this case of uplink transmission, at the gNB side, the MAC scheduler controls the reception of the MAC PDU at the subframe N+K, issuing the message UL_CONFIG.request(SFN=N+K) to the PHY layer that carries information for 5G RANGE PHY components configuration with the same set of configuration as described in Section 6.1, allowing the PHY layer to receive the uplink messages

transmitted by the UE at the subframe $N+K$. After reception, the PHY layer sends this MAC PDU to the MAC layer using the `RX_ULSCH.indication()` message.

Besides that, uplink transmission can include control information, which is carried by using UCI (uplink control information) transported via the PUCCH (physical uplink control channel). The PHY layer at the gNB side performs the decoding of the UCI and it is responsible to send this control information to the MAC layer using a specific P5 PHY SAP, depending on the type of control information that is received. This P5 PHY SAP messages are described in [63].

7 Conclusions

In this document we provided the complete definition of the 5G-RANGE PHY. By utilizing the previously introduced channel model [2], which is tailored to the project's application scenario in remote and rural areas, in all simulations, we make sure to design the PHY for the specific application. For 5G-ACRA, we specify to use a modified version of the 5G NR Polar code, which we apply on the transport and the control channel. Simulations results in practical 5G-RANGE setting reveal that it is not necessary to use two different channel coding schemes for high-end performance. This is in stark contrast to the evaluations with AWGN channels. The evaluation of waveform candidates for 5G-FlexNOW yields GFDM as most suitable waveform with respect to the mandatory requirements from [1]. Hence, GFDM is chosen as waveform for 5G-FlexNOW and we provide an adaptive flexible frame structure with 6 different numerologies to support a wide range use cases and especially all use cases and applications which are defined in [1]. Furthermore, the frame structure allows for coexistence with PUs and supports application with 6 MHz and 8 MHz TV channels, which are used in Brazil and Europe, respectively. The specification of 5G-IR2A contains novel channel estimation algorithms for GFDM and synchronization, which is based on 5G NR synchronization. The application of advanced STBC in 5G-MIMORA ensures a robust system which utilizes the diversity of the long-range cell channel. Furthermore, we define multiplexing and precoding schemes to also provide high data rates in some use cases. Both approaches are further enabled by a novel dual-polarization antenna technique, which allows to virtually double the number of antennas. The specification of each block carefully takes care of the associated system requirements [1]. Also, the PHY-MAC interface is briefly discussed in Section 6.

For the projects economic success, a low implementation complexity is essential. Therefore, for each block we carefully consider the implementation complexity. For 5G-ACRA we considerably reduce it by using only a single channel coding scheme, as opposed to two schemes in 5G NR. Furthermore, implementation complexity considerations for the encoder and decoder are provided in Section 2.3.1 as well as in [2]. For the implementation GFDM modulation and demodulation within FlexNOW we propose a novel FFT based framework (cf. Section 3.1.5.3). With this novel modem implementation, which is based on recent advances in GFDM, a competitive low complexity implementation is feasible. The complexity of the defined channel estimation schemes for 5G-IR2A is also low, and can be obtained in the references [39] and [40]. The synchronization complexity is similar to 5G NR. By using the novel dual-polarized antenna scheme as presented in Section 6.3, we can reduce the cost by virtually doubling the number of antennas, without physically doubling it. As a result, practical implementations of the 5G-RANGE PHY are expected to be viable at very low costs. This will also be demonstrated by the PoC in WP 6.

In WP 6, we will build an integrated simulator, which combines the PHY specified in this deliverable with the MAC layer (WP 4) and the network layer (WP 5). In these simulations an MCS (modulation and coding scheme) table has to be defined and optimized for the application in the 5G-RANGE network. Furthermore, detailed full system simulations will determine the overall system performance under various conditions and use cases to evaluate the system performance.

8 References

- [1] 5G-RANGE, ““Application and requirements report”, Deliverable 2.1, Work Package 2,” April 2018.
- [2] 5G-RANGE, ““Physical layer of the 5G-RANGE – Part I”, Deliverable 3.1, Work Package 3,” December 2018.
- [3] Huawei, HiSilicon, *R1-1611256: Performance evaluation of channel codes for small block sizes*, Reno, 2016.
- [4] 3GPP, *Technical specification (TS) 38.212 - NR; Multiplexing and channel coding. (Release 15)*, 2018.
- [5] A. Balatsoukas-Stimming, M. B. Parizi and A. Burg, “LLR-Based Successive Cancellation List Decoding of Polar Codes,” *IEEE Transactions on Signal Processing*, vol. 63, no. 19, pp. 5165-5179, 2015.
- [6] E. Sharon, S. Litsyn and J. Goldberger, “An efficient message-passing schedule for LDPC decoding,” in *23rd IEEE Convention of Electrical and Electronics Engineers in Israel*, Tel-Aviv, 2004.
- [7] E. Arikan, “Systematic Polar Coding,” *IEEE Communications Letters*, vol. 15, no. 8, pp. 860-862, 2011.
- [8] G. Sarkis, I. Tal, P. Giard, A. Vardy, C. Thibault and W. Gross, “Flexible and Low-Complexity Encoding and Decoding of Systematic Polar Codes,” *IEEE Transactions on Communications*, vol. 64, no. 7, pp. 2732-2745, 2016.
- [9] C. Schnelling, Y. Amraue and A. Schmeink, “On iterative decoding of polar codes: Schedule-dependent performance and constructions,” in *55th Annual Allerton Conference on Communication, Control, and Computing*, Monticello, IL, USA, 2017.
- [10] A. Elkelesh, M. Ebada, S. Cammerer and S. ten Brink, “Belief Propagation List Decoding of Polar Codes,” *IEEE Communications Letters*, vol. 22, no. 8, pp. 1536-1539, 2018.
- [11] 3GPP, *Technical specification (TS) 38.212 - NR; Multiplexing and channel coding*, 2017.
- [12] V. Bioglio, C. Condo and I. Land, “Design of Polar Codes in 5G New Radio,” 09 January 2019. [Online]. Available: <https://arxiv.org/abs/1804.04389>. [Accessed 22 January 2018].
- [13] F. Xi, C. Ye and R. L. Olesen, “A Polar Code Hybrid Rate Matching Scheme,” in *2018 European Conference on Networks and Communications (EuCNC)*, Ljubljana, Slovenia, 2018.
- [14] R. Kimura, A. Monma, J. Duan and M. Uesugi, “Block-Orthogonal Frequency Division Multiplexing in Multi-Path Fading Channel,” *Wireless Personal Communications*, vol. 38, p. 27–42, 2006.
- [15] J. Abdoli, M. Jia and J. Ma, “Filtered OFDM: A new waveform for future wireless systems,” in *2015 IEEE 16th International Workshop on Signal Processing Advances in Wireless Communications (SPAWC)*, Stockholm, 2015.
- [16] L. Mendes, N. Michailow, M. Matth  , I. Gaspar, D. Zhang and G. Fettweis, “GFDM: Providing flexibility for the 5g physical layer,” in *Opportunities in 5G Networks: A Research and Development Perspective*, CRC Press, 2016.

-
- [17] W. C. James and W. T. John, "An algorithm for the machine calculation of complex Fourier series," *Mathematics of computation*, vol. 19, no. 90, pp. 297-301, 1965.
 - [18] M. Matth  , L. L. Mendes and G. Fettweis, "Generalized Frequency Division Multiplexing in a Gabor Transform Setting," *IEEE Communications Letters*, vol. 18, pp. 1379-1382, 2014.
 - [19] A. Nimr, M. Matth  , D. Zhang and G. Fettweis, "Optimal Radix-2 FFT Compatible Filters for GFDM," *IEEE Communications Letters*, vol. 21, pp. 1497-1500, 2017.
 - [20] M. Danneberg, N. Michailow, I. Gaspar, D. Zhang and G. Fettweis, "Flexible GFDM Implementation in FPGA with Support to Run-Time Reconfiguration," in *2015 IEEE 82nd Vehicular Technology Conference (VTC2015-Fall)*, Boston, 2015.
 - [21] I. Gaspar, N. Michailow, a. Navarro, E. Ohlmer, S. Krone and G. Fettweis, "Low Complexity GFDM Receiver Based on Sparse Frequency Domain Processing," in *IEEE 77th Vehicular Technology Conference (VTC Spring)*, Dresden, 2013 .
 - [22] A. Nimr, M. Chafii and G. Fettweis, "Unified Low Complexity Radix-2 Architectures for Time and Frequency-Domain GFDM Modem," *IEEE Circuits and Systems Magazine*, vol. 18, pp. 18-31, 2018.
 - [23] E. Biglieri, S. Proakis and S. Shamai, "Fading channels: information-theoretic and communications aspects," *IEEE Transactions on Information Theory*, vol. 40, no. 6, pp. 2619-2692, 1998.
 - [24] A. Bahai, B. Saltzberg and M. Ergen, *Multi-Carrier Digital Communications: Theory and Applications of OFDM*, Springer, 2004.
 - [25] S. Pejoski and V. Kafedziski, "Estimation of Sparse Time Dispersive Channels in Pilot Aided OFDM Using Atomic Norm," *IEEE Wireless Communications Letters* , vol. 4, no. 4, pp. 397-400, 2015.
 - [26] Q. T. Zhang and S. H. Song, "Exact Expression for the Coherence Bandwidth of Rayleigh Fading Channels," *IEEE Transactions on communications*, vol. 55, pp. 1296-1299, 2007.
 - [27] 5G-RANGE, "Physical layer of the 5G-RANGE Part 1," 2018.
 - [28] S. H. Hwang, J. S. Um, M. S. Sun, C. J. Kim, H. R. Park and Y. H. Kim, "Design and Verification of IEEE 802.22 WRAN Physical Layer," in *2008 3rd International Conference on Cognitive Radio Oriented Wireless Networks and Communications (CrownCom 2008)*, Singapore, Singapore, 2008.
 - [29] T. S. Rappaport, *Wireless communications: principles and practice.*, New Jersey: Prentice Hall, 1996.
 - [30] M. S. Akram, *Pilot-based channel estimation in OFDM systems*, Master of Science Thesis, 2007.
 - [31] 3GPP, *Technical specification (TS) 38.211 - NR; Physical Channels and Modulation. (Release 15)*, 2018.
 - [32] T. M. Schmidl and D. C. Cox, "Robust frequency and timing synchronization for OFDM," *IEEE Transactions on Communications*, vol. 45, no. 12, pp. 1613-1621, 1997.
 - [33] A. Awoseyila, C. Kasparis and B. G. Evans, "Improved preamble-aided timing estimation for OFDM systems," *IEEE Communications Letters*, vol. 12, no. 11, pp. 825-827, 2008.

-
- [34] 3GPP, *Technical specification (TS) 38.104 - NR; Base Station (BS) radio transmission and reception. (Release 15)*, 2018.
 - [35] 3GPP, *Technical Specification (TS) 38.213; NR; Physical Layers Procedures for Control. (Release 15)*, 2018.
 - [36] B. Bertenyi, S. Nagata, H. Kooropaty, X. Zhou, W. Chen, Y. Kim, X. Dai and X. Xu, “5G NR Radio Interface,” *Journal of ICT, River Publishers*, vol. 6.1, pp. 31-58, 2018.
 - [37] S. Ehsanfar, M. Matthe, D. Zhang and G. Fettweis, “A Study of Pilot-Aided Channel Estimation in MIMO-GFDM Systems,” in *20th International ITG Workshop on Smart Antennas*, Munich, Germany, 2016.
 - [38] S. Ehsanfar, M. Matthe, D. Zhang and G. Fettweis, “Theoretical Analysis and CRLB Evaluation for Pilot-Aided Channel Estimation in GFDM,” in *2016 IEEE Global Communications Conference (GLOBECOM)*, Washington, DC, 2016.
 - [39] S. Ehsanfar, M. Matthe, D. Zhang and G. Fettweis, “Interference-Free Pilots Insertion for MIMO-GFDM Channel Estimation,” in *2017 IEEE Wireless Communications and Networking Conference (WCNC)*, San Francisco, CA, 2017.
 - [40] S. Ehsanfar, M. Matth  , M. Chafii and G. Fettweis, “Pilot- and CP-aided Channel Estimation in MIMO Non-Orthogonal Multi-Carriers,” *IEEE Transactions on Wireless Communications*, 2018.
 - [41] S. Kay, *Fundamentals of Statistical Signal Processing: Estimation Theory*, Upper Saddle River, NJ: Prentice Hall, 1993.
 - [42] J. R. Hampton, *Introduction to MIMO Communications*, New York, NY, USA: Cambridge University Press, 2014.
 - [43] J. Mietzner, R. Schober, L. Lampe, W. H. Gerstacker and P. A. Hoeher, “Multiple-antenna techniques for wireless communications - a comprehensive literature survey,” *Commun. Surveys Tuts.*, vol. 11, no. 2, pp. 87-105, Apr. 2009.
 - [44] S. M. Alamouti, “A simple transmit diversity technique for wireless communications,” *IEEE Journal on Selected Areas in Communications*, vol. 16, no. 8, pp. 1451-1458, Oct. 1998.
 - [45] V. Tarokh, N. Seshadri and A. R. Calderbank, “Space-time codes for high data rate wireless communication: Performance criterion and code construction,” *IEEE Trans. Inform.Theory*, vol. 44, no. 2, pp. 744-765, 1998.
 - [46] S. Mudulodu and A. Paulraj, “A transmit diversity scheme for frequency selective fading channels,” *Global Telecommunications Conference, GLOBECOM '00*, vol. 2, pp. 1089-1093, 2000.
 - [47] M. Matth  , L. L. Mendes and G. Fettweis, “Space-Time Coding for Generalized Frequency Division Multiplexing,” *European Wireless 2014; 20th European Wireless Conference*, pp. 1-5, 2014.
 - [48] M. Matthe, L. L. Mendes, I. Gaspar, N. Michailow, D. Zhang and G. Fettweis, “Multi-user time-reversal STC-GFDMA for future wireless networks,” *EURASIP Journal on Wireless Communications and Networking*, vol. 2015, no. 1, p. 132, may 2015.
 - [49] A. Paulraj and T. Kailath, “Increasing capacity in wireless broadcast systems using distributed transmission/directional reception (DTDR)”. US Patent Patent 5,345,599, Sep. 1994.

-
- [50] R. Gupta and A. Grover, “BER Performance Analysis of MIMO System using Equalization Techniques,” *Innovative Systems Design and Engineering*, vol 3, no. 10, 2012.
 - [51] Y. Jiang, M. K. Varanasi and J. Li, “Performance Analysis of ZF and MMSE Equalizers for MIMO Systems: An In-Depth Study of the High SNR Regime,” *IEEE Transactions on Information Theory*, vol. 57, pp. 2008 - 2026, April 2011.
 - [52] S. A. Bhagwatkar, B. P. Patil and B. S. Satpute, “Performance of MMSE channel equalization for MIMO OFDM system,” *Computing Communication Control and automation (ICCUBE)*, vol. 16, Aug. 2016.
 - [53] R. v. Nee, A. v. Zelst and G. Awater, “Maximum Likelihood Decoding in a Space Division Multiplexing System,” *IEEE 51st Vehicular Technology Conference Proceedings - VTC2000-Spring*, May 2000.
 - [54] R. BHAGYA and A. ANANTH, “Performance studies of 2x2 MIMO system for different modulation and OFDM multiplexing techniques using ML detector,” *International Journal of Electronics and Communication Engineering (IJECE)*, vol. 3, pp. 11-22, Sep. 2014.
 - [55] N. Khan, S. S. Pawar and M. S. Raeen, “An Architecture For Realizing Transmission For 2x2 MIMO Channel,” *International Journal of Emerging Technology and Advanced Engineering*, vol. 2, Sep. 2012.
 - [56] C. Oestges, B. Clerckx, M. Guillaud and M. Debbah, “Dual-polarized wireless communications: from propagation models to system performance evaluation,” *IEEE Transactions on Wireless Communications*, no. IEEE, p. 7, 2008.
 - [57] M. Coldrey, “Modeling and capacity of polarized MIMO channels,” in *Vehicular Technology Conference, 2008. VTC Spring 2008. IEEE*, 2008.
 - [58] S. Ogawa and F. Ono, “STBC-MIMO Network Coding with Dual Polarization Antennas,” in *Proceedings of 20th International Conference on Computer Communications and Networks (ICCCN)*, 2011.
 - [59] B. J. Wysocki, T. A. Wysocki and S. S. Adams, “On an Orthogonal Space-Time-Polarization Block Code,” *JCM*, vol. 4, 2009.
 - [60] J.-K. Hong, “Performance Analysis of Dual-Polarized Massive MIMO System with Human-Care IoT Devices for Cellular Networks,” *Journal of Sensors*, 2018.
 - [61] O. Jo, J.-J. Kim, J. Yoon, D. Choi and W. Hong, “Exploitation of Dual-Polarization Diversity for 5G Millimeter-Wave MIMO Beamforming Systems,” *IEEE Transactions on Antennas and Propagation*, vol. 65, pp. 6646--6655, 2017.
 - [62] 36.211, 3GPP Technical Specification TS, “E-UTRA: Physical Channels and Modulation (Release 9),” 2010.
 - [63] 5G-RANGE, “Definition of Cognitive MAC Reference Architecture”, Deliverable 4.1, Work Packet 4,” April 2018.
 - [64] Small Cell Forum, *FAP and nFAP Specifications*, Release 9, Doc 082.09.05, May 2017.